INL/EXT-18-51447
Revision 0

Baseline Postirradiation Examination of the AFC-3C, AFC-3D, and AFC-4A Experiments

Nuclear Technology Research and Development

Jason M. Harp
Luca Capriotti
Fabiola Cappia

Prepared for
U.S. Department of Energy
Advanced Fuels Campaign

Idaho National Laboratory
September 2018
NTRD-FUEL-2018-000120

SUMMARY

The AFC-3C, AFC-3D, and AFC-4A capsule irradiations were irradiated at the Idaho National Laboratory Advanced Test Reactor. These irradiations were planned to test several different fast reactor fuels that could be used to facilitate ultra-high burnup applications in sodium fast reactors. Several different alloys, fuel geometries, bonding materials, and the use of additives were tested in ferritic-martensitic HT-9 cladding. The AFC-3C and 3D experiment took various different U-Mo, U-Zr, U-Pd-Zr, U-Mo-Ti-Zr, and U-Mo-Ti-Zr-Pd alloys to burnups of 2.1% to 4.5% FIMA (fissions per initial heavy metal atoms) and fission densities of 6.13×10^{20} to 1.27×10^{21} fissions / cm^3. These alloys were evaluated against the historical fuel performance of previously irradiated fuel from literature. Fuel performance was irradiated through a suite of postirradiation examination techniques including neutron radiography, gamma spectrometry, dimensional inspection, fission gas release measurements, chemical burnup analysis, and optical microscopy. The irradiations were performed at relatively aggressive temperatures that resulted in significant interaction between the cladding and the fuel in many cases. In spite of this, there were no in-pile cladding breaches in these tests. The U-Zr alloys performed better than the U-Mo or U-Mo-Ti-Zr alloys. Some of the fuel-cladding interaction issues seen in helium bonded annular fuel that was not machined to tight tolerances appear to have been resolved by machining the outer diameter of annular fuel in this irradiation. Higher Zr concentrations in additive bearing fuel appears to have improved the performance of Pd additive fuel.

INTENTIONALLY BLANK

CONTENTS

FIGURES

TABLES

INTENTIONALLY BLANK

ACRONYMS

AFC	Advanced Fuels Campaign
AL	Analytical Laboratory
ATR	Advanced Test Reactor
DOE	Department of Energy
EBR-II	Experimental Breeder Reactor IIEDM
EFPD	effective full-power days
EPMA	Electron Probe Micro-Analysis
FCCI	Fuel-cladding Chemical Interaction
FFTF	Fast Flux Test Facility
FGR	fission gas release
FIMA	Fissions per Initial heavy Metal Atoms
FTA	Actinide Transmutation Fuels
GASR	Gas Assay, Sample, and Recharge
GECT	Gamma Emission Computed Tomography
HFEF	Hot Fuel Examination Facility
ICP-MS	Inductively Coupled Plasma-Mass Spectrometry
IFR	Integral Fast Reactor
INL	Idaho National Laboratory
LHGR	Linear Heat Generation Rate
NRAD	Neutron Radiography Reactor
PGS	Precision Gamma Scanner
PICT	peak inner cladding temperature
PIE	Postirradiation Examination
SEM	scanning electron microscopy
TRIGA	Training Research Isotope General Atomics

INTENTIONALLY BLANK

BASELINE POSTIRRADIATION EXAMINATION OF THE AFC-3C, AFC 3D, AND AFC-4A EXPERIMENTS

1. INTRODUCTION

A long term research focus of the US Department of Energy (DOE) Advanced Fuels Campaign (AFC) is to investigate technologies that can allow for increased actinide utilization in nuclear fuel for fast neutron spectrum reactors. This includes both the incorporation of minor actinides into nuclear fuel for transmutation and high utilization of actinides through "ultra high" burnup fuel. This goal is defined as fuel that can reach a burnup of 30-40 percent fission per initial metal atom (%FIMA) which is higher than what has historically been achieved [1, 2]. Historically, Experimental Breeder Reactor II (EBR-II) Mark III/IIIA/IV driver fuel (U-10Zr fuel with stainless steel 316 or ferritic martensitic steel HT-9 cladding) was qualified to 10%FIMA, but many experimental assemblies and fuel pins achieved higher peak burnup up to near 20%FIMA without failure [3]. The motivation of the irradiation tests explored in this work was to screen candidate alloys and forms that could tolerate very high burnup irradiations of up to 30 % FIMA. In these irradiations, termed AFC-3C, AFC-3D and AFC-4A, uranium-based alloys and forms were irradiated in a prototypic fast reactor spectrum to investigate fuel performance. Irradiations were performed in the Idaho National Laboratory (INL) Advanced Test Reactor (ATR). The performance of these fuels is compared to the historic performance of U-10Zr [4]. Metallic fuel for fast reactors has a long history that has been reviewed several time in the literature[3–8].

These irradiations test several different design variations in metallic fuel for fast reactors with a limited number of samples in addition to testing some variation in irradiation conditions. Because of this, it is difficult to understand fully the complete fuel performance behavior observed in these irradiations. However, it is possible to evaluate this fuel in 4 broad categories. U-10Mo alloys, which from a performance perspective include the 5Mo-4.3Ti-0.7Zr alloy irradiated in AFC-4A, were tested to evaluate the potential benefit of eliminating constituent redistribution in the fuel. Both alloys are single phase from room temperature up to melting. The lack of a phase transition eliminated constituent redistribution and should simplify the modeling of these systems. Previous irradiations have shown that while these alloys do not have constituent redistribution [9] they do interact with cladding more readily than U-Zr alloy even at moderate temperatures for sodium fast reactors. The second category is U-Zr based fuel. The vast majority of historical experience with U-10Zr is with 75% smeared density sodium bonded fuel. These irradiations stepped outside of that phase space to investigate annular fuel bonded without sodium and lower smeared densities. There is interest in removing sodium bonding from fuel to avoid mixed hazardous waste treatment on the back end of the fuel cycle [10]. Low smeared density annular or solid fuel is required to push burnup beyond 20%FIMA because solid fission products begin to fill all available porosity which leads to swelling in the cladding [4]. The third category is annular fuel, which has been investigated for both U-Mo and U-Zr alloys. The behavior of this fuel is closely connected with the base alloy, but these irradiations have shown the advantage of accurately machining annular fuel to the cladding inner diameter after casting. The fourth category is the addition of an additive, such as Pd, to control lanthanide driven fuel cladding chemical interaction (FCCI). These irradiations further emphasize the need to balance the amount of additive in the fuel with the major alloying element (Zr or Mo) in order to prevent early life interaction between the fuel and the cladding that can be exasperated by additives.

Postirradiation examination (PIE) performed of AFC-3C, AFC-3D and AFC-4A was primarily performed in the Hot Fuel Examination Facility (HFEF) located at the Idaho National Laboratory (INL) Materials and Fuels Complex (MFC). A variety of PIE is performed on the irradiated specimens including visual exams, neutron radiography, gamma spectrometry scanning, dimensional inspection, fission gas release measurements, optical microscopy and chemical burnup analysis. The results of these exams are recorded in this report and discussed in the context of literature and prior irradiations.

2. SUMMARY OF EXPERIMENT AND IRRADIATION CONDITIONS

2.1 Motivation and Experiment Test Matrix

The AFC-3C and AFC-3D irradiations tests are an extension of the AFC-3 and AFC-4 irradiation tests to investigate alloys and forms beyond the standard fuel from EBR-II (U-10Zr, 75% smear density, sodium bonded solid fuel). The test matrix for AFC-3C, AFC-3D and AFC-4A is shown in Table 1. AFC-3C and AFC-3D repeated many of the alloys irradiated in AFC-3A and AFC-3B [9]. The AFC-3A/B irradiations were terminated early due to fabrication issues with the capsule, while the AFC-3C/D irradiations were completed as scheduled after 2, 3 or 4 cycles in the reactor. The burnup accumulated in these irradiations is adequate to evaluate the early life performance of these alloys and forms. The irradiated alloys were either U-10Mo, U-10Zr or U-13Zr with Pd. The Mo alloys are meant to prevent constituent redistribution in the fuel, potentially simplifying fuel modeling. The U-10Zr irradiations explore smear densities, fuel forms, and bonding material options. The Pd containing fuel are meant to investigate the addition of Pd to the fuel as a getter for lanthanides. Helium bonded, annular fuel is explored to remove the sodium bond from the fuel. The sodium bond creates an additional complication on the back end of the fuel cycle, forcing fuel to be treated prior to disposal. In a full recycle fuel cycle, this is not necessarily a disadvantage, but, in a once-through fuel cycle, sodium treatment is undesirable.

Table 1. AFC-3C, AFC-3D and AFC-4A Test Matrix.

Rodlet ID	Table 1	Fuel Form	Bond Material	Nominal Smear Density	Outer Diameter (mm)	Inner Diameter (mm)	Total Height (mm)	As-built Smear Density
3C-R1	U-10Mo	Solid	Sodium	75%	4.28	N/A	38.1	74.5%
3C-R2	U-10Mo	Annular	Helium	55%	4.92	3.30	38.1	54.4%
3C-R3	U-10Zr	Sodium	Solid	65%	3.98	N/A	37.8	64.6%
3C-R4	U-10Zr	Annular	Helium	55%	4.93	3.29	38.1	54.8%
3C-R5A	U-1Pd-13Zr	Solid	Sodium	75%	4.3	N/A	19.0	74.6%
3C-R5B	U-2Pd-13Zr	Solid	Sodium	75%	4.3	N/A	19.0	74.6%
3D-R1	U-10Zr	Annular	Helium	55%	4.91	3.30	38.0	53.8%
3D-R2	U-4Pd-13Zr	Solid	Sodium	55%	3.66	N/A	38.1	54.6%
3D-R3	U-10Mo	Solid	Sodium	55%	3.66	N/A	38.1	54.6%
3D-R4	U-10Mo	Annular	Helium	55%	4.92	3.30	38.1	54.4%
3D-R5	U-4Pd-13Zr	Annular	Helium	55%	4.92	3.30	38.1	54.0%
4A-R1	U-10Mo	Annular	Helium	65%	4.88	2.92	38.1	62.2%
4A-R3	U-5Mo-4.3Ti-0.7Zr	Solid	Sodium	75%	4.27	—	38.1	74.2%
4A-R4	U-5Mo-4.3Ti-0.7Zr-2Pd	Solid	Sodium	75%	4.27	—	38.1	74.2%
4A-R5	U-10Zr	Solid	Sodium	75%	4.27	—	38.1	74.2%

The AFC-4A irradiations explore a different alloy of Mo, Ti and Zr to stabilize U. This alloy sought to both keep the fuel single phase during irradiation, thus preventing constituent redistribution, while still providing the FCCI benefits that U-Zr alloy fuels enjoy over U-Mo alloy fuels. The additive Pd was also explored in this system. A Mo alloy with tungsten was planned, but it was not possible to alloy tungsten during fabrication.

2.2 Irradiation Capsule Design Cadmium Shroud Description/Approach

The basic design of the AFC-3 and AFC-4 irradiation experiments is illustrated in Figure 1. The fuel is irradiated in a Cd shroud (Figure 1a) to create a radial power profile that is prototypic of fast reactor conditions [11]. The validity of the technique has been evaluated previously and is documented in the Spectrum Comparison Report [12]. The AFC-3C and AFC-3D alloys were formed by mixing appropriate quantities of metals in an arc melter. The alloys were homogenized through a series of several melts. The alloys were then cast into quartz molds using a counter gravity injection casting system where a vacuum is used to draw the alloy melt into the mold. The annular fuel molds contained an inner quartz core. After casting, the molds are removed by breaking the quartz off the outside of the cast pins. For the annular pins, the inner quartz core was removed from the cast pin by drilling. The outside of the annular slugs was machined to the desired outer diameter. This is an important improvement over the AFC-3A/B fuel slug fabrication that will be discussed in the PIE discussion Section (3.2). The fuel slugs were then cut to length. The AFC-4A fuel slugs were fabricated in the same manner but, instead of counter gravity injection, the slugs were gravity cast into quartz molds using the arc melter. For each rodlet, the fabricated fuel is placed inside HT-9 cladding with an inner diameter of 4.95 mm and an outer diameter of 5.84 mm. If sodium is used, it is placed inside the rodlet before the top end cap is welded on. The sodium is settled by heating the welded rodlet in a well furnace followed by gentle tapping. The sealed rodlets are then placed inside a stainless steel 316 capsule as shown in Figure 1b. The capsule provides temperature control across the gap between the rodlet and the capsule and is the primary safety barrier between the experiment and the ATR coolant.

The fabrication of AFC-3C/D is specified in INL document SPC-1607 [13] documented in project files as the AFC-3C/D As-Built Data Package and ECAR-2317 [14] for the rodlets and the capsules. The AFC-4A fabrication is specified in SPC-1620 [15] and documented in ECAR-2373 [16] and in the project files as the AFC-4A As-Built Data Package.

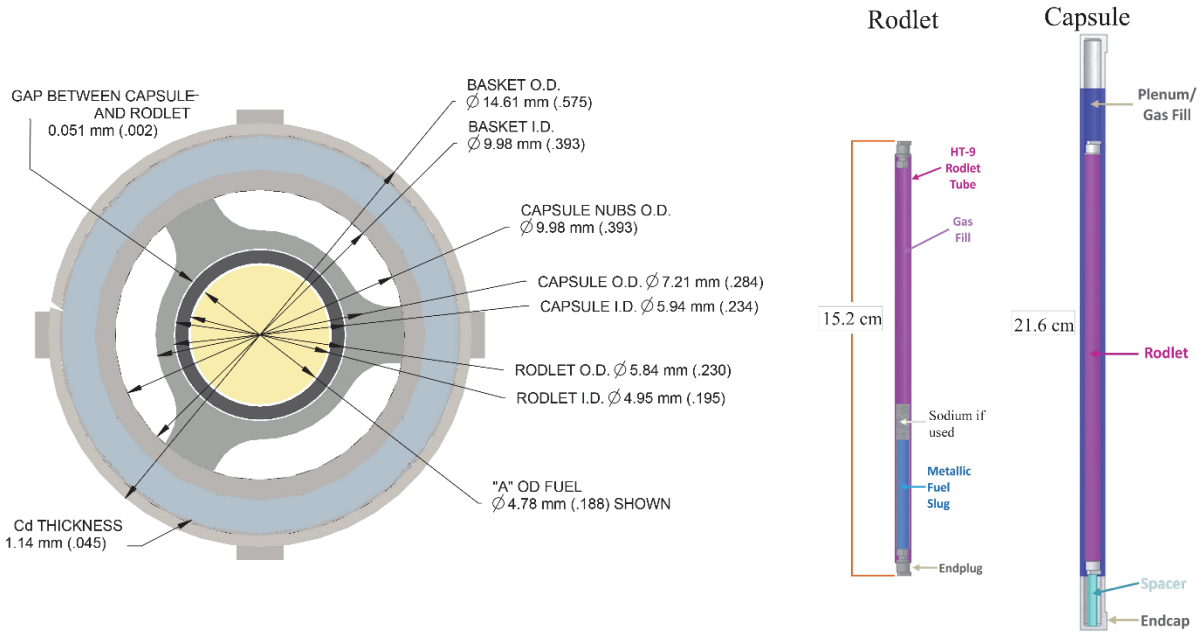

(a) (b)

Figure 1. (a) AFC-3 Cross section with Basket, Capsule, Rodlet, and fuel, (b) Typical configuration of AFC rodlet and capsule.

2.3 AFC-3C, AFC-3D and AFC-4A Irradiation History

The AFC-3C capsules all were placed in the reactor during the same cycles. Irradiation began August 23, 2013 in ATR cycle 154B for 53.5 effective full power days (EFPD), continued in cycle 155A for 55.1 EFPD, and was finished in cycle 157C for 5.4 EFPD. There was a large break in the irradiation between 155A and 157C that lasted from January 16, 2014 until February 10, 2015.

All the AFC-3D capsules began irradiation in cycle 154B for 53.5 EPPD, then were removed and not irradiated again until cycle 157A for 37.6 EFPD. AFC-3D R1 and AFC-3D R4 were irradiated additionally in cycle 158A for 52.2 EFPD and cycle 158B for 51.4 EFPD.

AFC-4A was irradiated in cycle 155A, cycle 157C, and cycle 157D. The history of the irradiations along with the cycles, cycle dates, and EFPD information is shown in Table 2. There were several major emerging repairs at ATR that account for the long break between cycle 157A and 157C.

Table 2. Irradiation History of AFC-3C, AFC-3D and AFC-4A.

Cycle	Start Date	End Date	EFPD	AFC-3C Cumulative EFPD	AFC-3D Cumulative EFPD 2,3,5	AFC-3D Cumulative EFPD 1,4	AFC-4A Cumulative EFPD
154B	8/23/2013	10/16/2013	53.5	53.5	53.5	53.5	—
155A	11/8/2013	1/16/2014	55.1	108.6	—	—	55.1
155B	2/3/2014	4/12/2014	49.9	—	—	—	—
157A	7/23/2014	8/30/2014	37.6	—	91.1	91.1	—
157C	2/10/2015	2/15/2015	5.4	114	—	—	60.5
157D	5/29/2015	8/12/2015	59.7	—	—	—	120.2
158A	11/10/2015	1/2/2016	52.2	—	—	143.3	—
158B	2/8/2016	4/1/2016	51.4	—	—	194.7	—

The as-run neutronic and thermal irradiation histories for each rodlet were calculated by combining the results of neutronic and thermal analysis of each capsule. The heat generation and linear heat generation rate (LHGR) in each capsule is calculated using whole ATR core Monte Carlo (MCNP 6.0) simulations coupled with ORIGEN for depletion. The recorded ATR power history from each cycle and the initial ATR core loading are used as inputs to these simulations. The heat generation rates are then supplied to a finite element analysis code (Abaqus) to calculate the temperatures in the capsule. The axial variation in power and temperature is relatively low. For the fuel documented in this work, fuel performance can largely be tied back to the inner cladding temperature. The inner cladding temperature adjacent to the fuel slug is no more than ±20°C from the peak inner cladding temperature (PICT). Through the finite element analysis, it was possible to generate a relationship between LHGR and PICT [17,18]. The LHGR in any capsule varies directly with the ATR lobe power for the location of the capsule. In Figure 2, Figure 3, and Figure 4, the hourly ATR lobe power history has been converted to hourly LHGR history for each capsule and further converted to the hourly PICT history for each capsule. The hourly PICT is plotted against EFPD in ATR. The dips in these graphs is related to reactor shutdowns or scrams of the reactor.

The PICT for almost all the rodlets in AFC-3C, AFC-3D and AFC-4A are higher than desirable. Any time spent above 600°C for a metallic fuel clad in an iron-based alloy is going to cause some degree of FCCI. The root cause of the high temperatures experienced by these rodlets is the sensitivity of the design of the experiment to the gap distance between the rodlet outer diameter and the capsule inner diameter. The gap between the rodlet and the capsule creates the proper temperature conditions in the fuel, but small variations in the gap have a large impact on PICT. A contributing factor to the elevated temperatures is the difficulty of fabricating high precision tubes from bar stock. High precision tubing is typically extruded and swaged to final dimensions. Because the AFC capsule is not a standard dimension, the

capsule tubes are machined from bar stock. The drawing for the capsules specifies an inner capsule dimension of 0.234±0.001 inches (0.59436± 0.00254 cm). As-built every capsule used for these irradiations was between 0.2347 inches inner diameter and 0.235 inches inner diameter. These capsules met the drawing specification, but the enrichments for the experiments were set assuming 0.234 inch inner diameter capsules. This difference is the primary contributor to the higher PICT seen by these rodlets. Contributing factors include variations in ATR lobe power and the neutronic behavior of ATR that increases flux at the top and bottom of the core later in the ATR cycle. The later effect is illustrated in the PICT trends experienced by AFC-3C R1 and AFC-3C R5 in Figure 2.

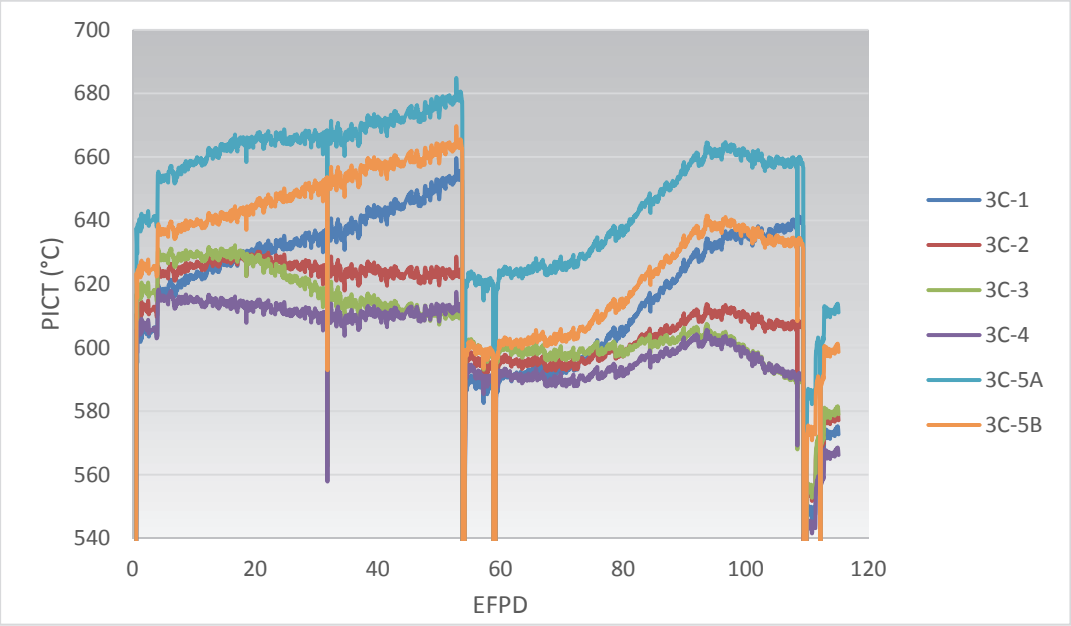

Figure 2. PICT history for AFC-3C experiments.

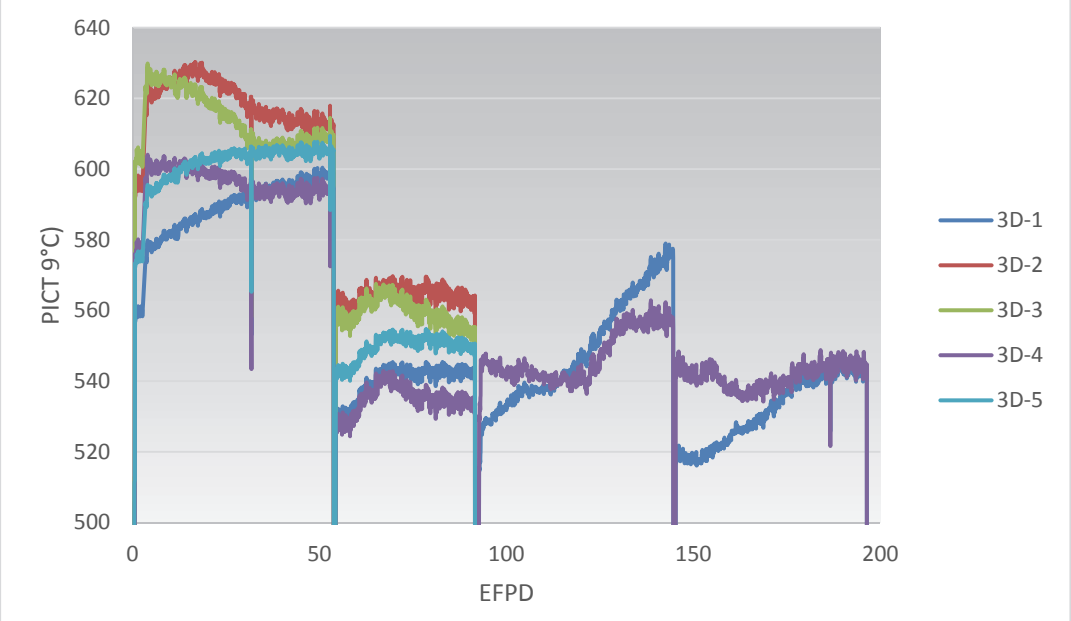

Figure 3. PICT history for AFC-3D experiments.

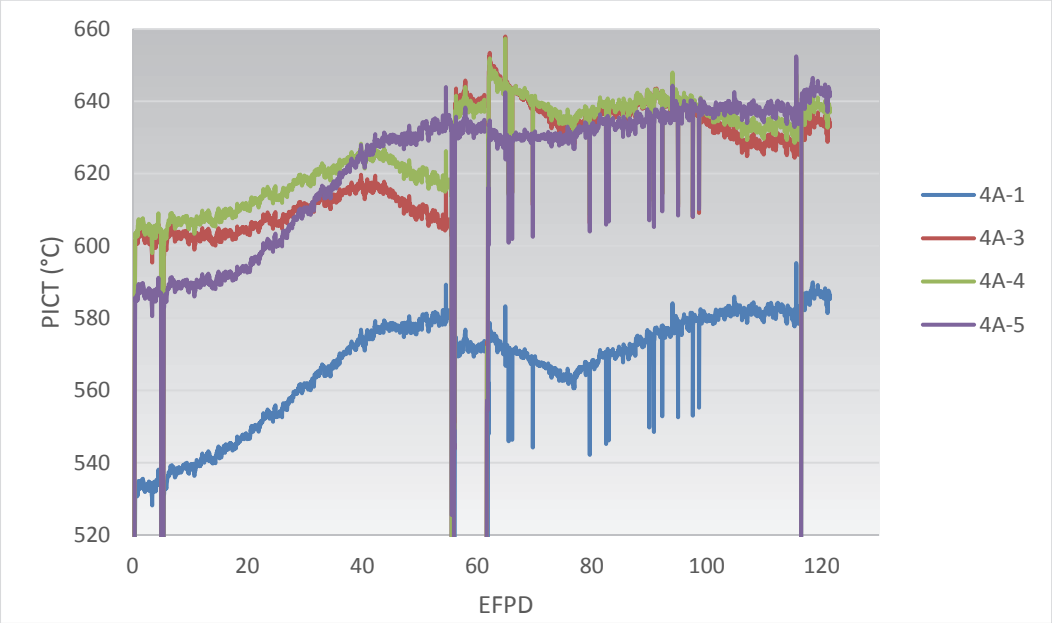

Figure 4. PICT history for AFC-4A experiments.

3. AFC-3C AND AFC-3D

Postirradiation Examination (PIE) results from the examination of AFC-3C and AFC-3D are summarized in the following section followed by a discussion of the results. The AFC-3C and AFC-3D irradiations explored several concepts that may enable ultra high burnup fuel (>30 %FIMA) for sodium fast reactors. The most studied alloying element for uranium in metallic fuel is Zr. These irradiations examined replacing Zr with Mo. Ultra high burnup would require smear densities below 75% to accommodate the production of solid fission products. Low smear density fuels (55% and 65%) were irradiated to investigate the impact of lowering smear density. Sodium bonding creates some issues with fuel treatment after irradiation. Helium bonded metallic fuel was also investigated to understand the impact of removing the sodium bond.

3.1 Results from PIE

In the following sections, the PIE results from AFC-3C and AFC-3D will be shown. Examinations included visual inspection, neutron radiography, cladding profilometry, gamma-ray spectrometry, fission gas release analysis, optical microscopy and chemical analysis. These exams evaluate the engineering scale performance of the fuel and can be related to the phenomenological performance of the fuel as well.

3.1.1 Neutron Radiography

Neutron radiography was performed using the Neutron Radiography Reactor (NRAD) located in the basement of HFEF. The NRAD reactor is a 250kW TRIGA reactor with two beam lines. The east beam line services a position below the main floor of the hot cell and is used for irradiated fuel. Neutrons pass through the fuel specimen and expose different activation foils [19]. The radiography fixture contains a scale marked with Gd paint that produces a calibrated scale for quantitative measurements of irradiated fuel dimensions. The fixture used in these shots also contained a hafnium step wedge. This allows the gray scale from radiographs to be mapped to a known neutron attenuation.

Neutron radiography images were taken of the AFC-3C and AFC-3D pins at 6 angles with both a dysprosium (Dy) foil for thermal neutron radiography and a Cd-covered indium (In) foil for epithermal neutron radiography. Each angle was taken 30° apart. The rotations were fixed by placing the rodlets in a collet to fix the radial position. The collets were geared so that the fuel pins could be rotated exactly 30° between each shot. An example of the thermal neutron radiography with each pin labeled is shown in Figure 5 for AFC-3C. Detailed neutron radiographs of the fuel material are shown in Figure 6 for thermal neutron radiography and Figure 7 for epithermal neutron radiography.

There are some notable features in the neutron radiography. AFC-3C R1 contains some areas of low density that may indicate excess porosity about 15 to 18 mm above the end cap. AFC-3C R2 appears to have remained annular which is expected for U-10Mo, based on the AFC-3A/B irradiations [9]. The AFC-3C R3 pin has less attenuation in the center of the fuel pin also, which may indicate either enhanced porosity or less neutron attenuation from constituent redistribution in this pin. The annulus in AFC-3C R4 (U-10Zr) also appears to have largely remained open, but it does appear that the annulus has shrunk some from the as-built inner diameter. Very little can be discerned from the AFC-3C R5 radiograph. The enrichment of this pin is high, allowing very little neutron penetration. The pin appears to have behaved well, in line with historical expectations. The sodium plug above the fuel in 3C R1 extends about 6 mm, and the plug above the fuel in 3C R3 extents about 3.5 mm. There is no evidence of a large sodium plug above 3C R5.

Representative neutron radiography from AFC-3D is shown in Figure 8 for the entire pins, and the fuel is detailed in Figure 9 for thermal neutrons and Figure 10 for epithermal neutrons. The annulus in 3D R1 appears to have remained open along the majority of the fuel zone. The curvature in the lower attenuation band seen on the fuel may indicate some closure at the top of the fuel column or possibly constituent redistribution along temperature gradients. The radiographs of 3D R2 and 3D R3 show some asymmetric

behavior. This sort of behavior was also seen in solid, low smear density pins in AFC-3A/B [9] and in EBR-II irradiations [20]. However, the axial growth in 3D R3 (U-10Mo) is significantly greater than in R2 (U-10Zr). The annuli in 3D R4 and 3D R5 appear to have remained open.

The quantitative measurement generally obtained from neutron radiography of irradiated fuels is axial growth of the fuel column. For EBR-II metallic fuel experiments, axial growth of the fuel slug was mostly easy to measure using neutron radiography or precision gamma scanning. The fuel slugs began irradiation at 34.3 cm long and, although the fuel sometimes looked much less dense at the top and make identifying the exact point of the top of the fuel slug difficult, the fuel axial growth data obtained in this way were generally consistent. In contrast, the fuel segments in the ATR experiments are less than 4 cm long. This makes it very difficult to assess in a consistent way the axial growth in these short fuel column rodlets to compare to EBR-II experiments. There is simply too much subjective judgment in selecting the as-irradiated fuel slug length, so comparison to axial growth measurements from EBR-II is not entirely meaningful. Furthermore, there is a lack of consensus among experts concerning how to understand the phenomenon of axial growth in metallic fuels. There is some evidence that suggests axial growth in metallic fuel may be in part an end effect that happens in close proximity to the unconstrained, free fuel surface at the top of the fuel column. For example, measured axial growths in Fast Flux Test Facility (FFTF) irradiations of metallic fuel have been noted to be less than those for identical compositions in EBR-II [21]. If that is the case, it may not make sense to compare axial growth expressed as a percent of total fuel length for metallic fuel columns of significantly different lengths. This may not be a fuel phenomenon that necessarily differs solely due to differences in neutron spectra, but differs in part due to differences in total fuel length.

However, since AFC-3C and AFC-3D all had the same length, some comparisons between alloys can be made. Axial growth for each rodlet is summarized in Table 3. The trend noted earlier about axial growth between 3D R2 and 3D R3 also holds for all the rodlets in 3C and 3D. The U-Mo based alloys appear to have more axial growth than the U-Zr based alloys. This may be related to how fission gas is retained in the different alloys. Also the He bonded annular pins tend to have less growth than the solid pins.

Table 3. Axial Growth in AFC-3C and AFC-3D

Rodlet ID	Alloy	Bond Material	Type	Axial Growth
3C-R1	U-10Mo	Sodium	Solid	18%
3C -R2	U-10Mo	He	Annular	11%
3C -R3	U-10Zr	Sodium	Solid	7%
3C -R4	U-10Zr	He	Annular	2%
3C -R5	U-1Pd-13Zr	Sodium	Solid	7%
3D-R1	U-10Zr	He	Annular	4%
3D -R2	U-4Pd-13Zr	Sodium	Solid	6%
3D -R3	U-10Mo	Sodium	Solid	19%
3D -R4	U-10Mo	He	Annular	5%
3D -R5	U-4Pd-13Zr	He	Annular	2%

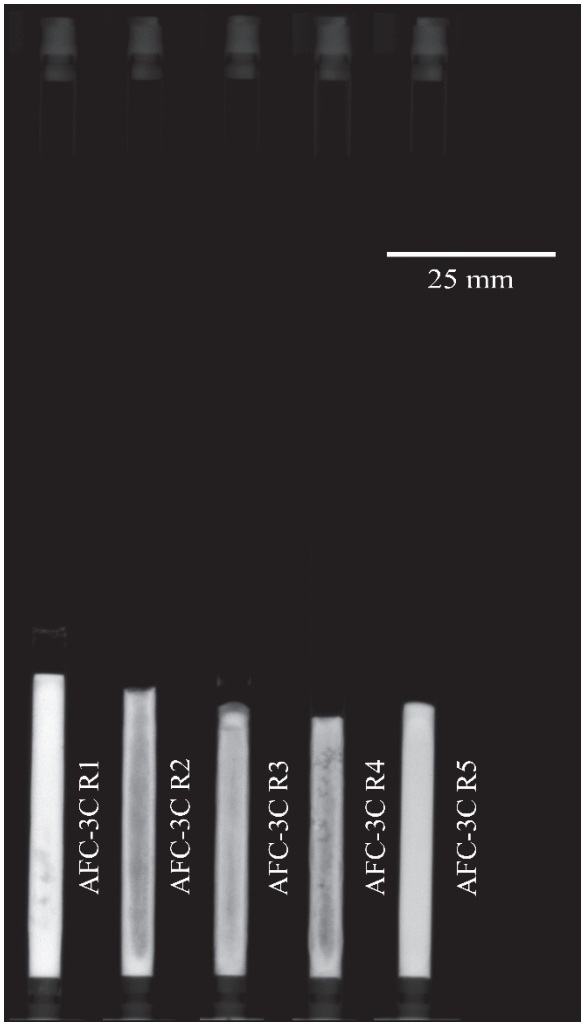

Figure 5. Thermal neutron radiograph showing the entire AFC-3C rodlets.

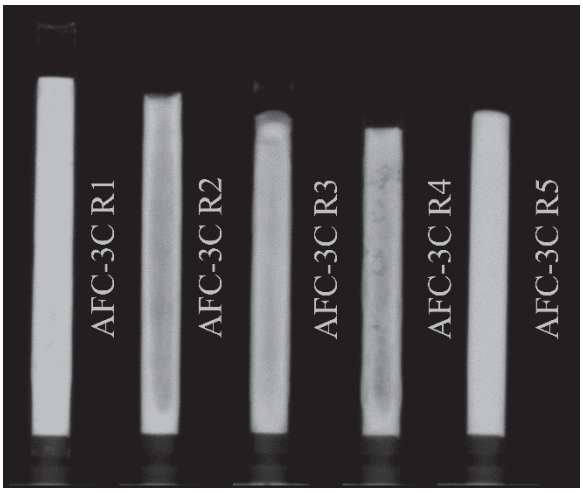

Figure 6. Thermal neutron radiography of the AFC-3C fuel.

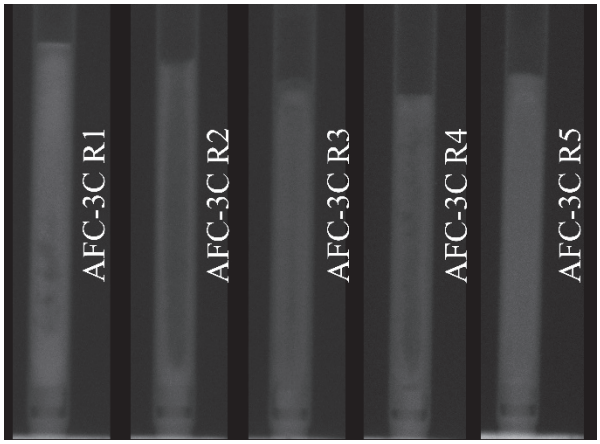

Figure 7. Epithermal neutron radiography of the AFC-3C fuel.

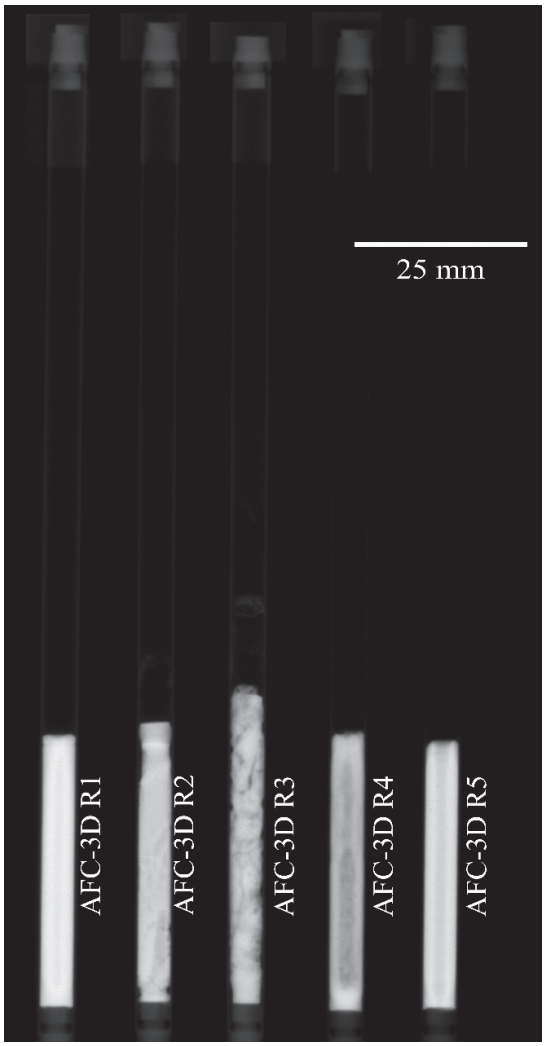

Figure 8. Thermal neutron radiograph showing the entire AFC-3D rodlets.

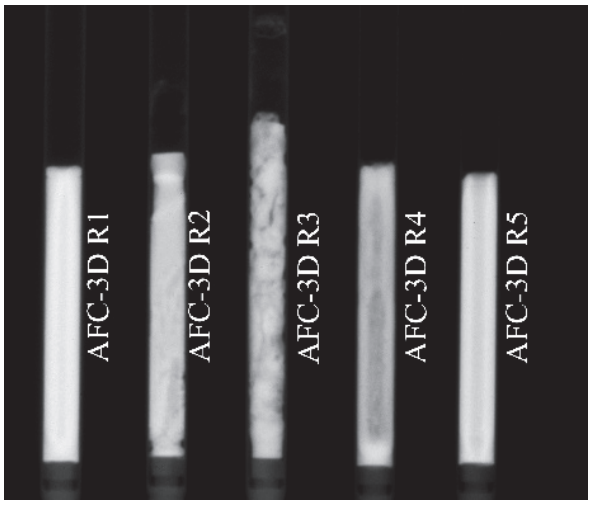

Figure 9. Thermal neutron radiography of the AFC-3D fuel.

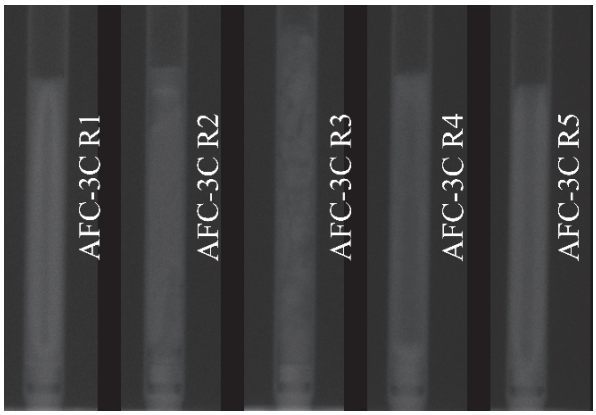

Figure 10. Epithermal neutron radiography of the AFC-3D Fuel.

3.1.2 Dimensional Inspection

Dimensional inspections of AFC-3C and AFC-3D were performed using the US HPRR Plate checker in HFEF. Outside diameter measurements were collected all along the rodlets in roughly 0.5 mm increments and at 36 angles every 5° from the initial scan angle to 175°. Diameter measurements are collected with ±5 μm accuracy. The angle averaged measured diameters for the AFC-3C rodlets are shown in Figure 11, and the angle averaged measured diameters for the AFC-3D rodlets are shown in Figure 12. The bounding as-specified cladding dimensions are also shown by the blue box on the figures, and the capsule inner diameter is also shown to demonstrate the maximum possible diameter the rodlet could reach by swelling or thermal creep. The diameters are by the distance from the top of the fuel pin, which puts the fueled portion of the rodlet towards the right side of the figure. The AFC-3C rodlets clearly have experienced some dimensional change. This is probably related to thermal creep due to the high temperatures experienced by these rodlets (see Figure 2). The temperatures experienced by AFC-3D were much lower, and there is essentially no dimensional change measured in these rodlets.

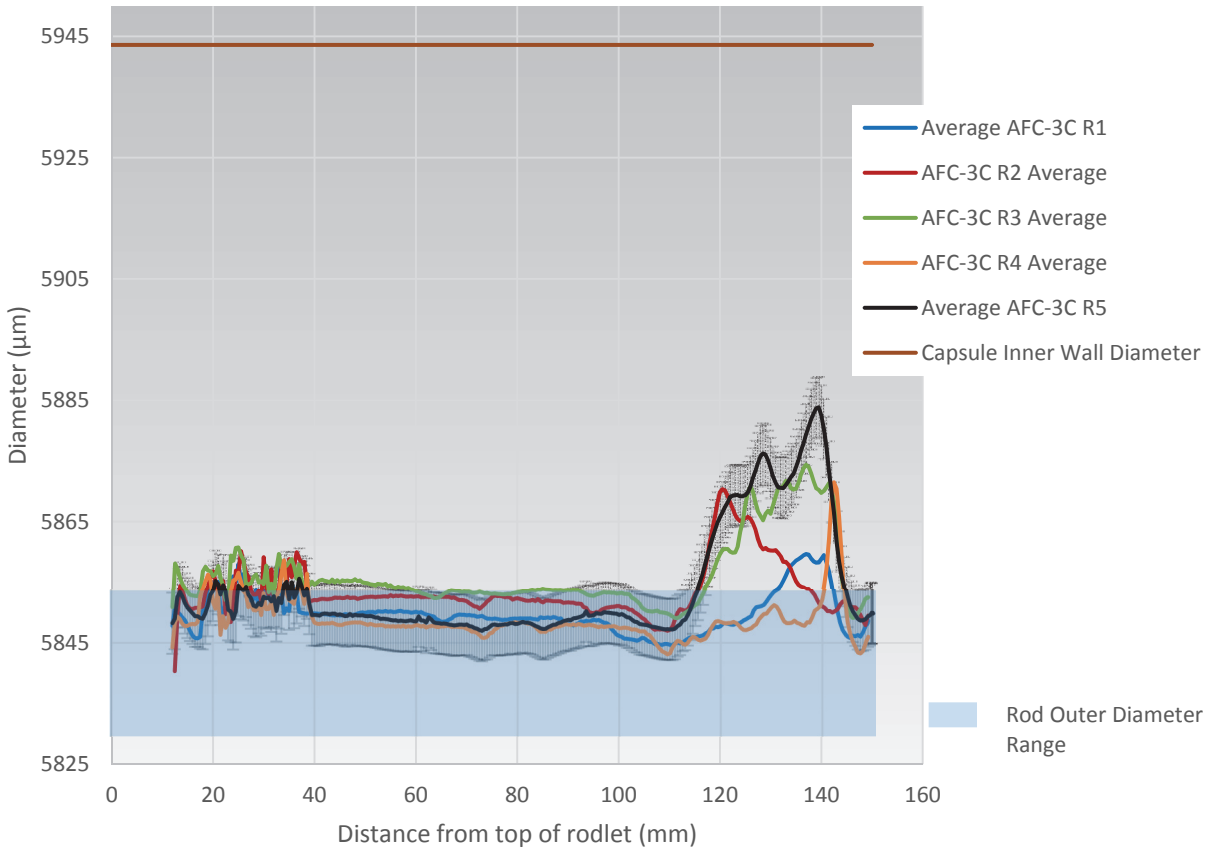

Figure 11. Measured diameters for AFC-3C rodlets.

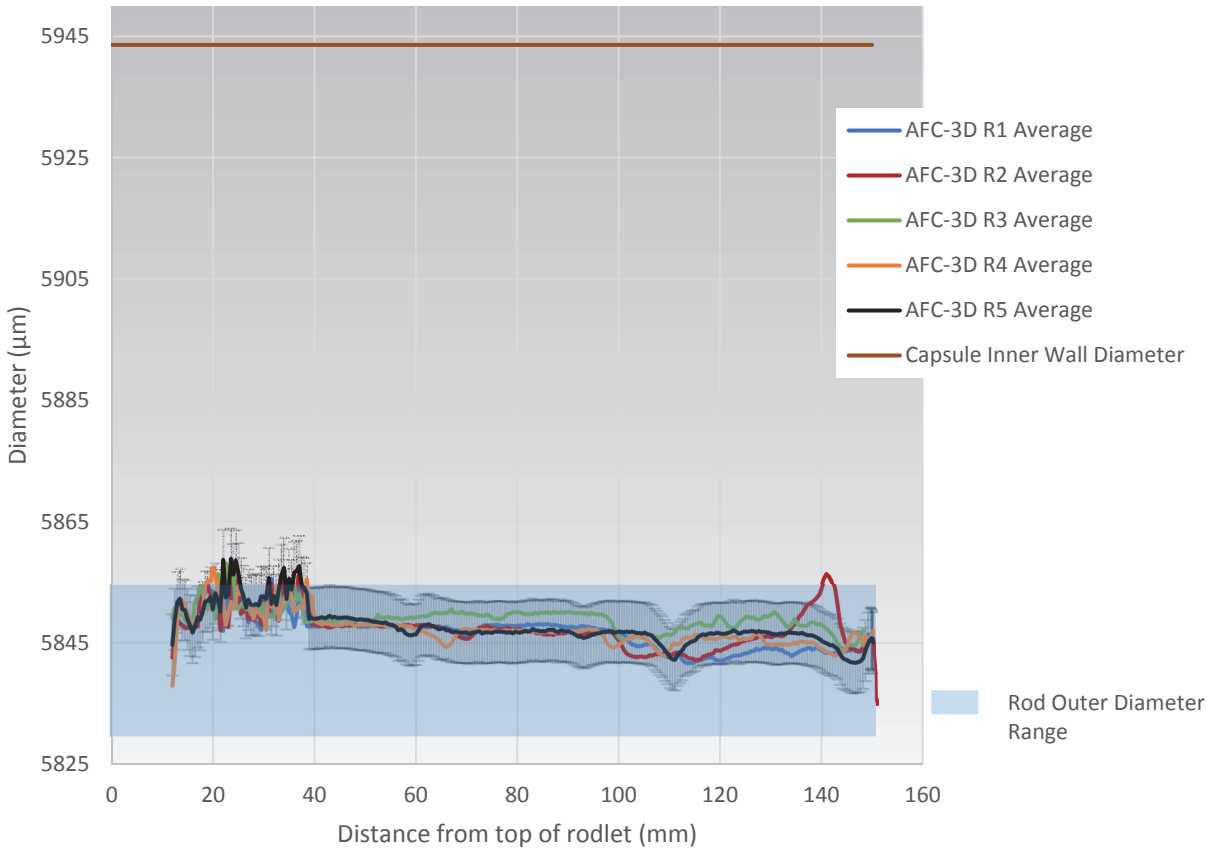

Figure 12. Measured diameters for AFC-3D rodlets.

3.1.3 Gamma Spectrometry

Gamma ray spectrometry of all of the AFC-3C and 3D rodlets was performed using the HFEF Precision Gamma Scanner (PGS). The PGS has three major components: collimator, stage, and detector. The collimator penetrates the HFEF cell wall with a rectangular aperture that is adjustable from 0.254 cm to 0.00254 cm in height and is 2.2225 cm wide. The collimator can be rotated from a horizontal to vertical orientation. The stage manipulates the sample in front of the collimator in the plane facing the collimator and can rotate the sample about its central axis. The detector consists of a Compton suppressed high purity germanium detector, and its control system moves the stage and collimator and initiates the scans.

Gamma spectrometry was performed on each AFC-3C and AFC-3D rodlet individually. The rodlets were scanned in 0.127 cm steps for a live time of 30 minutes. Several fission products were detected in the gamma spectrometry, including: Ru-106 (as Rh-106), Sb-125, Cs-134, Cs-137, Ce-144, Eu-154, and Ce-144 (as Pr-144). Additionally, several activation products were detected, including Co-60 and Mn-54. Since Mn-54 is not a fission product, its signal is used in the axial profile plots to indicate the location of the cladding and cladding endcaps where this signal spikes. The axial gamma spectrometry scans from 4 rodlets are shown in Figure 13, Figure 14, Figure 15, and Figure 16.

The behavior of gamma emitting fission products follows trends observed earlier in AFC-3A/B [9]. There are certain trends for sodium bonded, solid fuel and specific trends for helium bonded annular fuel. The cesium behavior change is the most pronounced. In the sodium bonded case, Cs dissolves into the sodium and transports above the fuel column into the sodium plug located above the fuel. This trend is seen in Figure 13. This also occurs with Eu-154, which tends to behave as a volatile in metallic fuel in contrast to

the behavior of Ce in the fuel represented by the CePr-144 signal. Cesium in the annular fuel does not transport above the fuel slug, but it does transport and collect at the cooler axial ends of the fuel slug. These spikes are seen in Figure 14, Figure 15, and Figure 16. However, there is a peak in the axial center of the fuel slug in Figure 14 and also to a lesser degree in Figure 16. It is not clear if this hump is Cs that has not migrated out of this portion of the fuel column or if there is a microstructural feature that has trapped Cs in this area. The CePr-144 signal is tied to the behavior of lanthanides in the fuel. At high burnup in metallic fuel, lanthanides migrate to the cladding and cause FCCI. This could be detected by local spikes in CePr-144 distribution, but there are not spikes like this detected in the AFC-3C/D rodlets as is expected for this burnup. The Ce spike in Figure 16 appears to be due to a location change in density when the location of the spike is compared to the neutron radiograph. Ruthenium and other noble metals integrate well into metallic fuel alloys and do not migrate as shown for the 4 pins plotted here. The Mn-54 signal shows the location of rodlet endcaps.

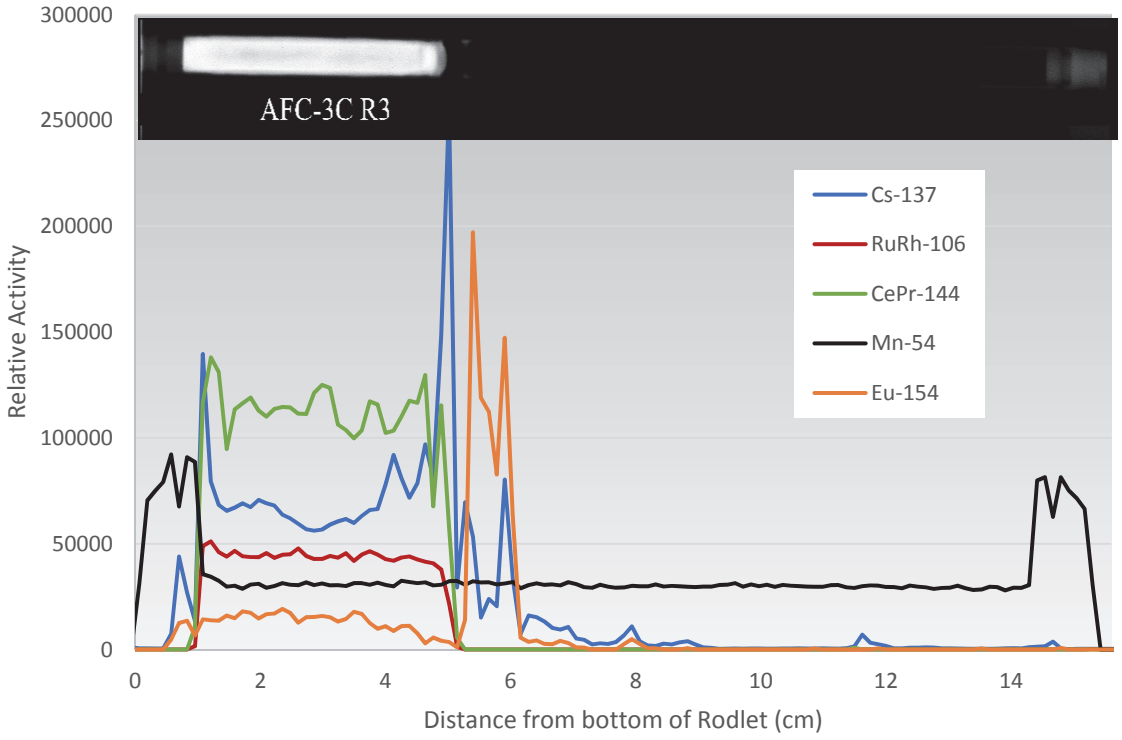

Figure 13. Axial gamma scan of AFC-3C R3 showing key radionuclides.

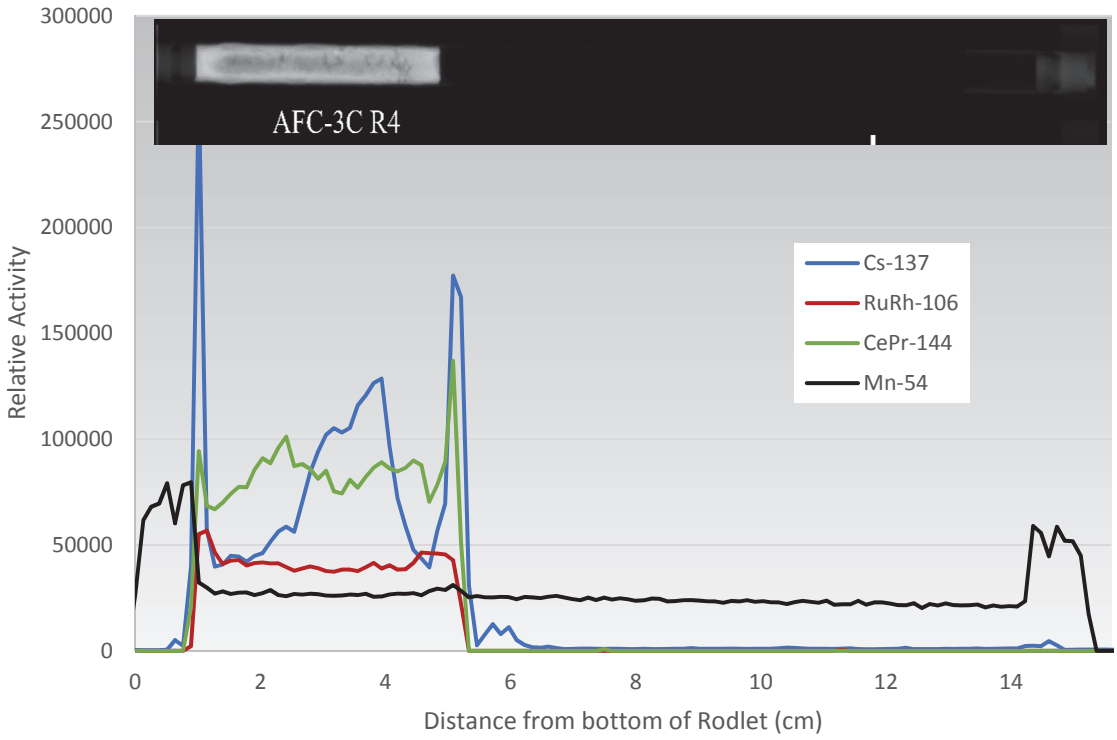

Figure 14. Axial gamma scan of AFC-3C R4 showing key radionuclides.

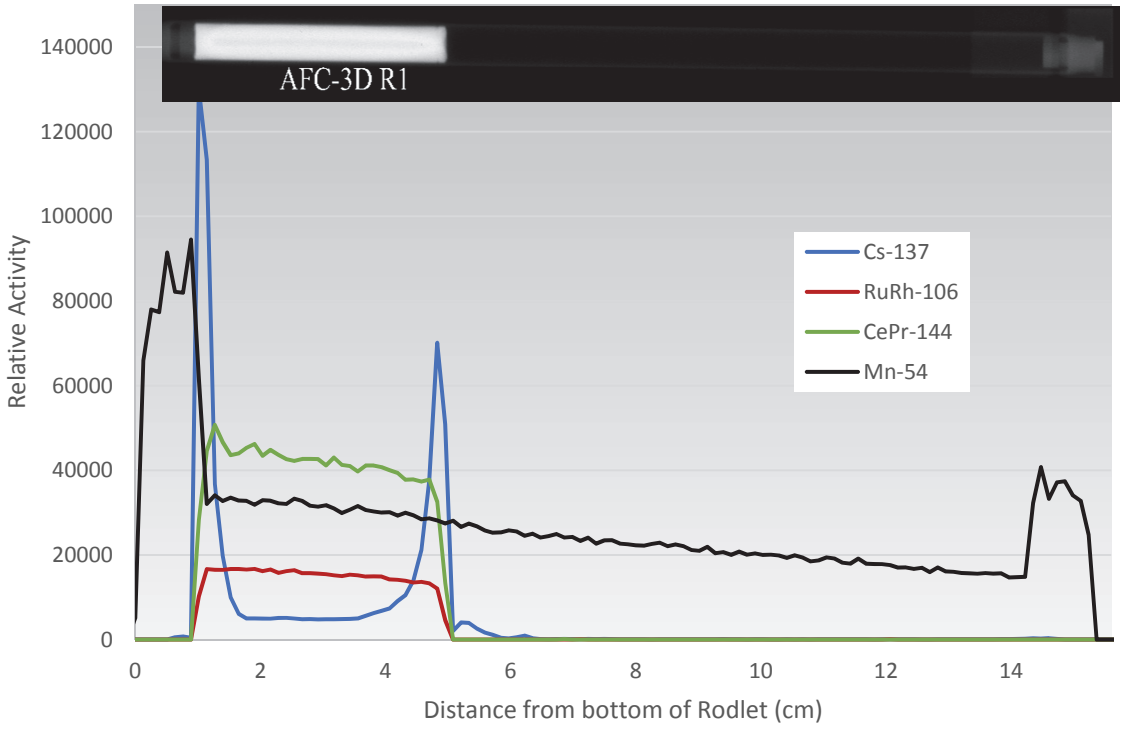

Figure 15. Axial gamma scan of AFC-3D R1 showing key radionuclides.

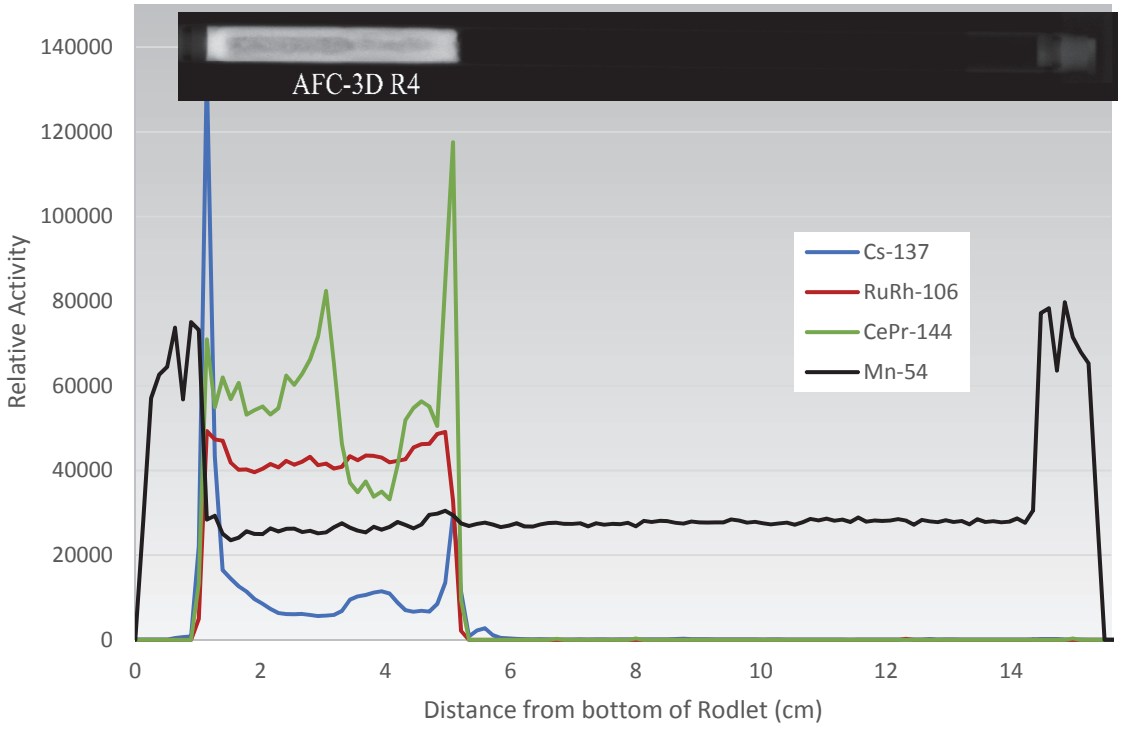

Figure 16. Axial gamma scan of AFC-3D R4 showing key radionuclides.

In addition to axial gamma spectrometry scans, it is possible to rotate the HFEF PGS collimator from a horizontal to a vertical orientation. In this orientation, it is possible to move an axial level of the fuel past the collimator and perform a series of rotations over several angles. The resulting signals over several angles can be collected and tomographically reconstructed to provide a two-dimensional distribution of fission products averaged over an axial location. This is referred to as Gamma Emission Computed Tomography (GECT). The full details of this technique are available in Reference [22], and the demonstration of this technique can be seen in Reference [23] and [9]. This technique is similar to conventional X-ray computed tomography, but it is limited by the number of angles that can practicably be collected as spectrum collection takes several minutes, and the total collection time can extend to several days or weeks for a fully characterized rodlet.

The GECT technique was applied to both AFC-3C R3, AFC-3C R4, AFC-3D R1 and AFC-3D R4. Data were collected at the mid-plane of the fuel slug. The results of the GECT for Cs-137, Ru-106, and CePr-144 are shown in Figure 17, Figure 18, and Figure 19, respectively. In all these plots, the general position of the cladding is represented by two black rings that represent the inner and outer diameter of the cladding. The Cs-137 distribution is quite similar for all the measured rodlets. Overall, the Cs appears to have migrated to the outer radius of the fuel slug near the cladding. The solid fuel pin (Figure 17a) does have some Cs-137 signal throughout the radius of the fuel pin, while the annular pins (Figure 17b-d) have a depressed signal in the center of the fuel. The RuRh-106 signal shows more differences. The solid pin shows an annular distribution of Ru-106, which may indicate some significant Zr redistribution in this pin. The ring of Ru-106 in Figure 18b compared to the ring in Figure 18c and Figure 18d indicates that the annulus in Figure 18b may have closed more than the other pins. This is not surprising, considering the higher temperatures experienced by AFC-3C R4. The temperatures may have been high enough in AFC-3C R4 to cause some Ru migration with Zr. The Ce-144 tomograms in Figure 19 are all also generally ring shaped. This again indicates some large central porosity may have formed in AFC-3C R3 (Figure 19a). The Figure 19b and Figure 19c tomograms generally indicated Ce-144 is distributed

throughout the fuel. The unusual distribution is shown in Figure 19d; there is indication of CePr-144 signal in the center of the fuel, and the signal is also near the cladding. However, the Ru-106 signal indicates there is no fuel in the central area, and neutron radiography also generally indicates the annulus is intact for this pin. The signal observed here may be Ce migrating to the annulus independent of fuel swelling.

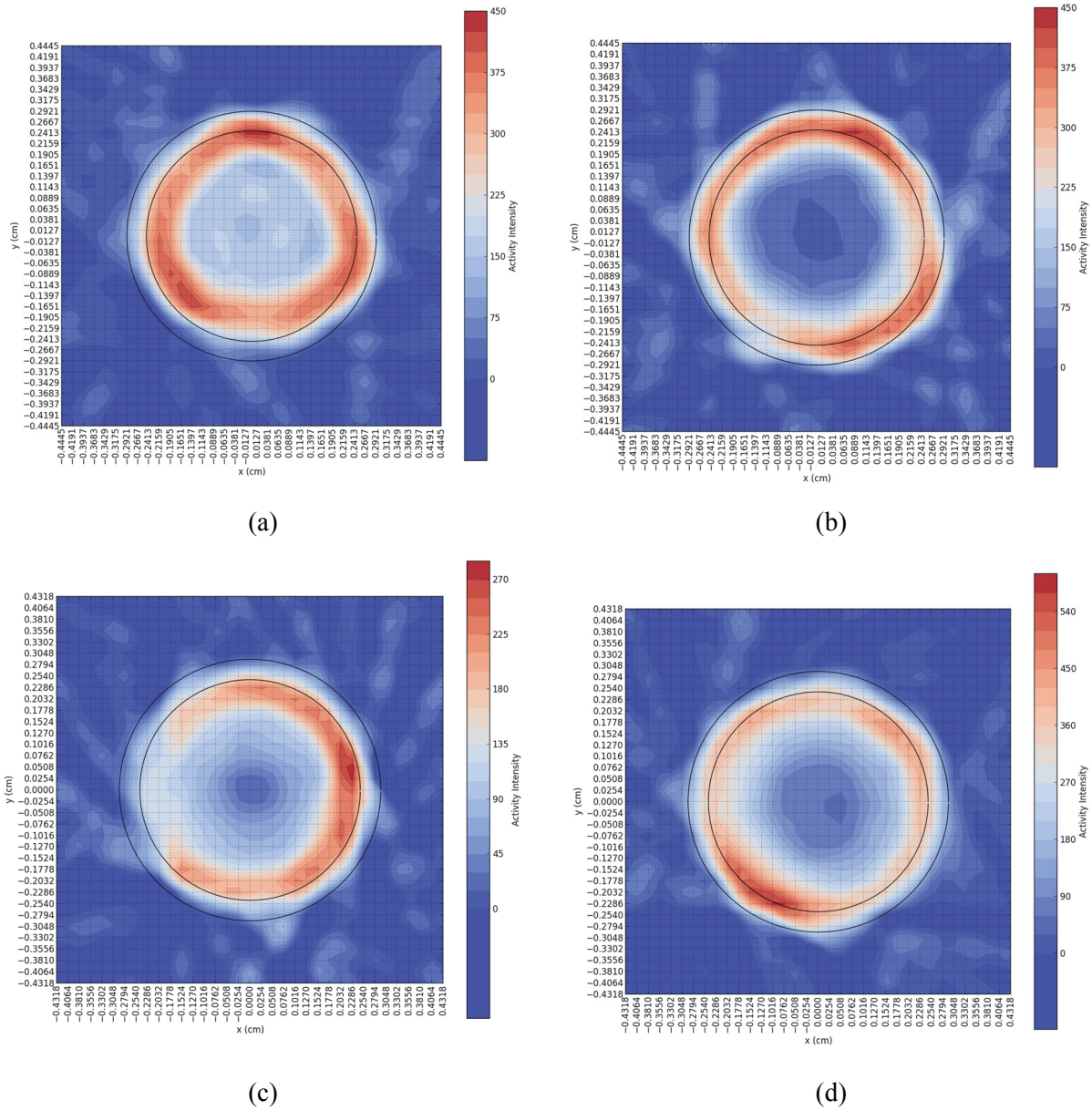

Figure 17. Cs-137 distribution in the middle of the fuel zone for select AFC-3C and AFC-3D pins
(a) AFC-3C R3, (b) AFC-3C R4, (c) AFC-3D R1, (d) AFC-3D R4

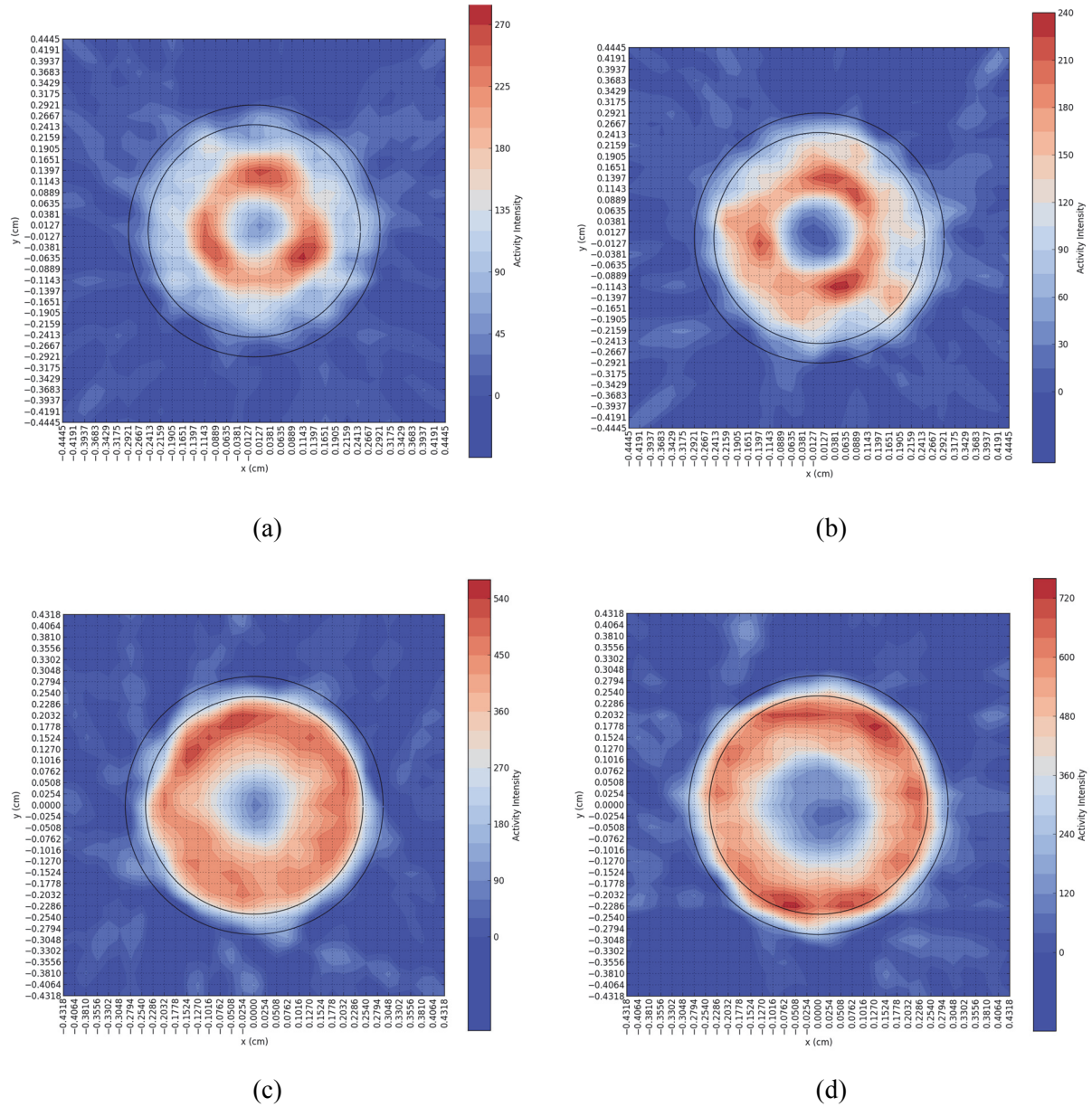

Figure 18. Ru-106 distribution in the middle of the fuel zone for select AFC-3C and AFC-3D pins (a) AFC-3C R3, (b) AFC-3C R4, (c) AFC-3D R1, (d) AFC-3D R4

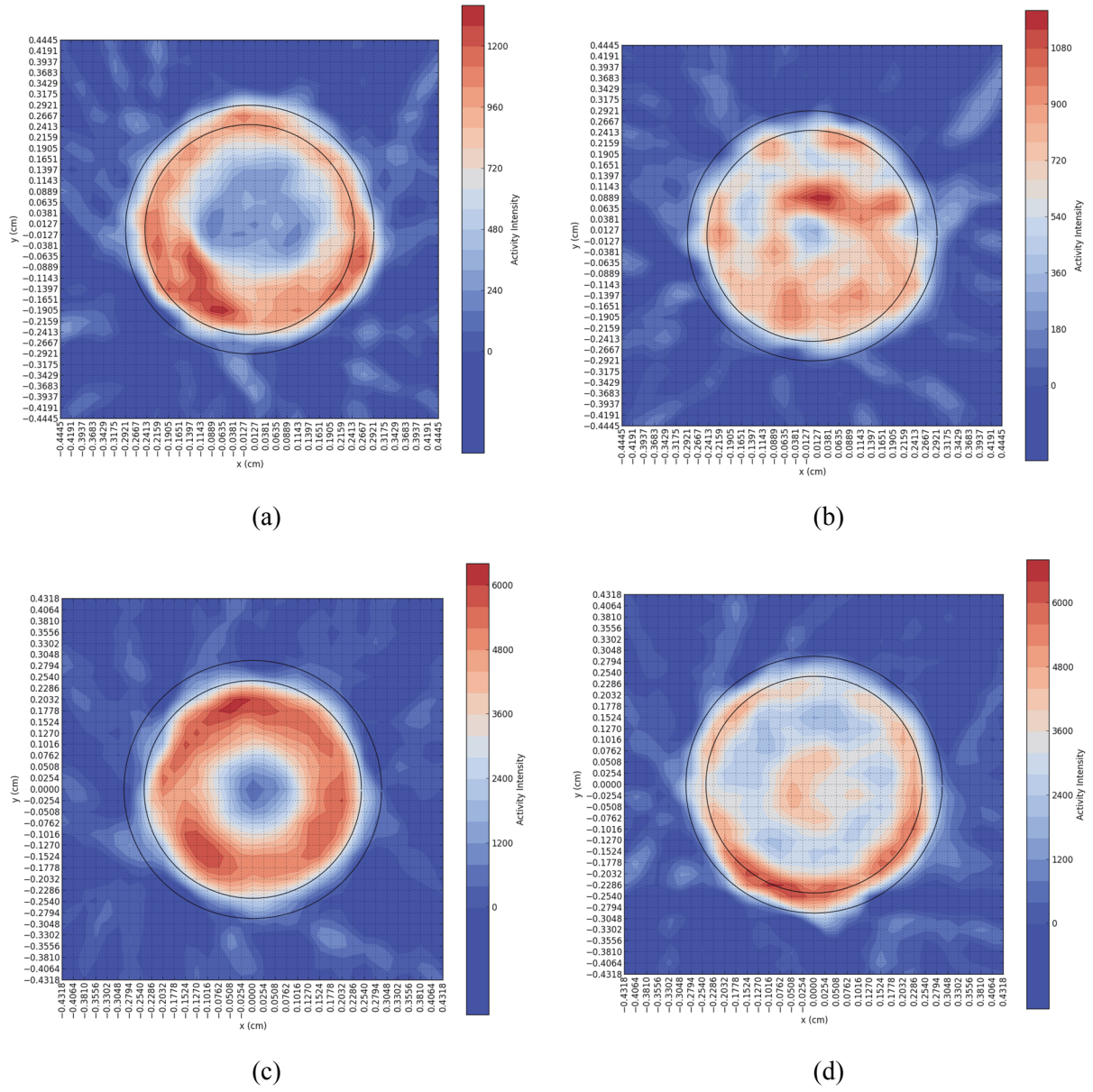

Figure 19. CePr-144 distribution in the middle of the fuel zone for select AFC-3C and AFC-3D pins (a) AFC-3C R3, (b) AFC-3C R4, (c) AFC-3D R1, (d) AFC-3D R4.

3.1.4 Fission Gas Release

Fission gases were collected from the rodlets using the HFEF Gas Assay, Sample, and Recharge (GASR) system. Rodlets were punctured using a 150 W Nd-YAG laser system, and a gas sample was collected in a stainless steel bottle external to the hot cell. Void volume in the rodlet was then determined by a series of backfills into the punctured rodlet and expansions into the GASR system. The rodlet internal gas pressure was derived from the void volume measurement and the initial gas pressure measurement upon puncture. Fission gas analysis was performed by gas mass spectrometry. Results of fission gas analysis provided total elemental composition, krypton isotopic composition, and xenon isotopic composition. A summary of results for AFC-3C and AFC-3D is shown in Table 4. The fission gas release (Kr+Xe release) is based on an estimate of the number of fissions that occurred in each rodlet from U-235, Pu-239 and other nuclei that is input into an empirical relationship between fission and atoms of Xe and Kr

produced. The number of fission in each rodlet was determined in two ways from predicted fission density and from inductively coupled plasma-mass spectrometry (ICP-MS). The number of fissions from ICP-MS are derived from results discussed in Section 3.1.5. Both fission gas release (FGR) values for each rodlet are shown in Table 4. The measured fissions FGR is higher than the predicted fissions FGR, and some of the measured fission FGR values are greater than 100%, which reveals some bias in this calculation. The FGR from measured fission values requires some assumptions that may have created a bias. Additionally, the FGR by both methods for AFC-3C R2 is quite low. The collected gas sample had some air contamination. If the air contamination is ignored, the FGR for this rodlet rises to 60%. Metallic fuel fission gas release historically is 70%±10% for 75% smear density, sodium-bonded U-10Zr and U-19Pu-10Zr fuel for fission densities beyond 7×10^{20} fissions per cm^3, and the majority of fission gas release occurs by 5×10^{20} fissions per cm^3 [12,24]. All the rodlets except AFC-3C R1 and AFC-3C R5 have fission densities greater than 7×10^{20} fissions per cm^3, and 3C R1 and R5 have fission densities greater than 5×10^{20} fissions per cm^3. Thus, many of the AFC-3C and AFC-3D pins match the historical experience, but some of the pins have relatively high FGR. The FGR of these pins will be discussed in the Discussion section.

Table 4. Fission Gas Release Summary.

Rodlet	Fission Gas Release (Predicted Fission)	Fission Gas Release (Measured Fission)
AFC-3C R1	56%	81%
AFC-3C R2*	17%*	17%*
AFC-3C R3	91%	113%
AFC-3C R4	87%	102%
AFC-3C R5	38%	58%
AFC-3D R1	85%	114%
AFC-3D R2	59%	67%
AFC-3D R3	42%	50%
AFC-3D R4	64%	69%
AFC-3D R5	66%	76%
*`There was air contamination in this sample. Correcting for the air contamination, the FGR is 60%.		

3.1.5 Burnup

During rodlet sectioning to create the microscopy samples, additional samples were taken from near the fuel column mid-plane and sent to the INL Analytical Laboratory (AL) for a variety of chemical and isotopic analyses. The primary goal of these analyses was to ascertain the burnup of the sampled material. Gamma spectrometry analysis was also performed.

Burnup is calculated from the results of mass spectrometry measurements of dissolved fuel samples. The fuel is dissolved, and aliquots are sent through several different ICP-MS devices. A chemical separation for Pu was performed to help fully analyze the actinide content of the fuel. The determination of burnup was performed using the measured mass of a specific fission product in the fuel, the cumulative fission yield of that specific fission product, and the total mass of actinides present in the sample. This method is sometimes referred to as the "Fission Product Monitor - Residual Heavy Atom" technique [25,26] and calculates burnup in Fission per Initial heavy Metal Atoms (%FIMA). All fission yields were taken from ENDF/B-VII.1 [27]**Error! Reference source not found.**. A benefit of this burnup technique is that it requires no *a priori* knowledge of the sample. The burnup value and information about the fuel is also used to calculate fission density. The fission density tends to be a more consistent metric for comparing fuel performance across different experiments.

The measured burnup values, the measured fission densities, and the calculated burnup for each rodlet are shown in Table 5. The burnup was calculated using the measured actinide concentration and the concentration of the following nuclides: La-139, Ce-140, Ce-142, Pr-141, Nd-145, and Nd-146. The exception was AFC-3C R4, which was calculated with Tc-99, Ru-101, Ru102, Rh-103, and Ru-104 concentrations. The burnup values match the prediction fairly well. The fission densities have a greater discrepancy, but these values are more susceptible to bias in some of the assumptions that go into the calculation.

3.1.6 Metallography

Optical microscopy was performed on samples from all rodlets from AFC-3C and AFC-3D. Two samples were collected from each rodlet. A 5.1 mm transverse slice was cut from near the mid-plane of the fuel slug. This slice was mounted as a transverse metallurgical mount showing the full circumference of the fuel at near the fuel axial mid-height. There was also a 10.1 mm slice of fuel cut from a height of interest in the fuel slug. This slice was mounted in a longitudinal mount. The mount was then ground from the cladding outer radius to the center line of the fuel. Optical microscopy was performed using a Leica DMi8 inverted microscope. Figure 20 through Figure 46 on the following pages contain optical microscopy collected for AFC-3C and AFC-3D. These images are discussed in context with the irradiation conditions and other PIE in the subsequent sections.

Table 5. Burnup values for AFC-3C and AFC-3D Rodlets.

Rodlet	Simulation Burnup (%FIMA)	Simulation Fission Density (fissions/cm^3)	Measured Burnup (%FIMA)	Measured Fission Density (fissions/ cm^3)
AFC-3C R1	2.3%	8.82E+20	2.1%	6.39E+20
AFC-3C R2	3.2%	1.21E+21	3.3%	9.27E+20
AFC-3C R3	2.8%	9.70E+20	2.9%	7.88E+20
AFC-3C R4	3.4%	1.18E+21	3.0%	7.89E+20
AFC-3C R5A	2.8%	8.64E+20	2.6%	6.66E+20
AFC-3D R1	4.6%	1.61E+21	4.3%	1.08E+21
AFC-3D R2	2.8%	8.38E+20	2.7%	5.91E+20
AFC-3D R3	2.2%	8.41E+20	2.1%	5.68E+20
AFC-3D R4	4.6%	1.69E+21	4.5%	1.27E+21
AFC-3D R5	2.9%	8.97E+20	2.7%	6.09E+20

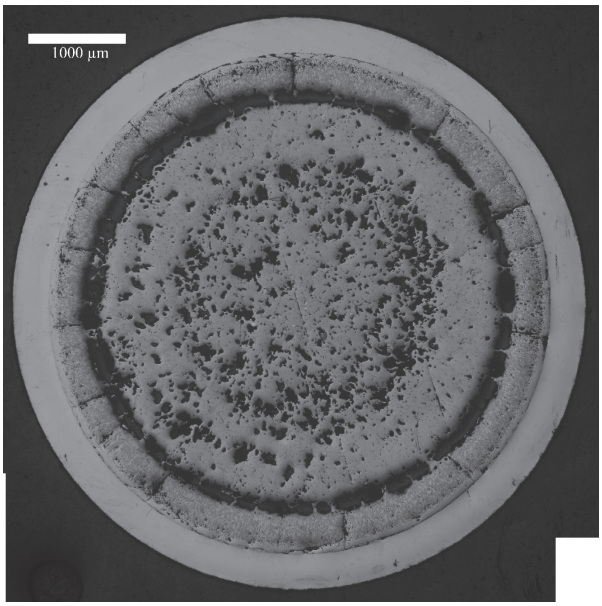

Figure 20. Transverse cross section of AFC-3C R1 (U-10Mo, 75% smear density, solid, sodium bonded).

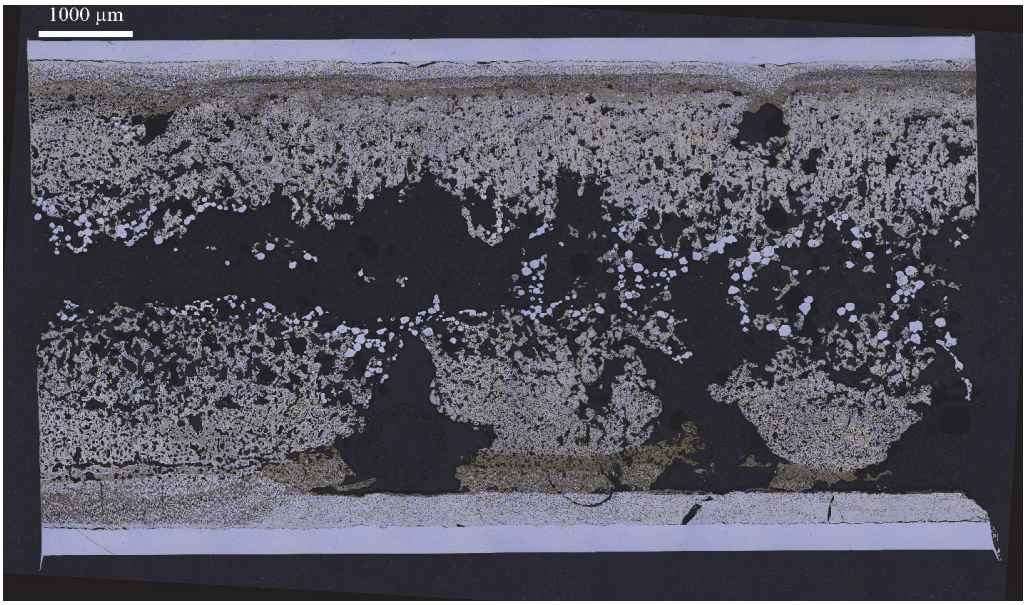

Figure 21. Longitudinal section of AFC-3C R1 taken 10.5 mm above the fuel slug bottom. Fuel slug center and top towards the right side of the image.

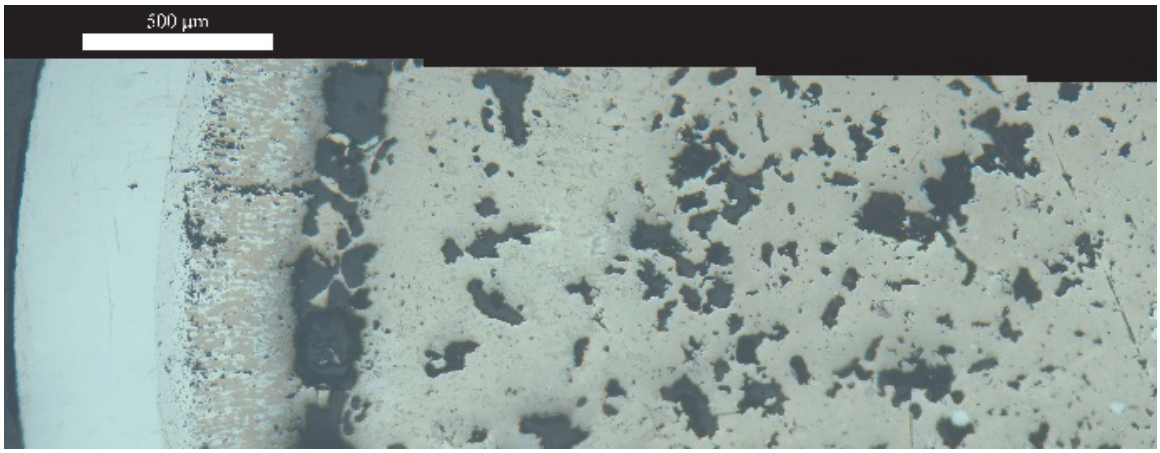

Figure 22. Higher magnification detail of radial microstructure of AFC-3C R1.

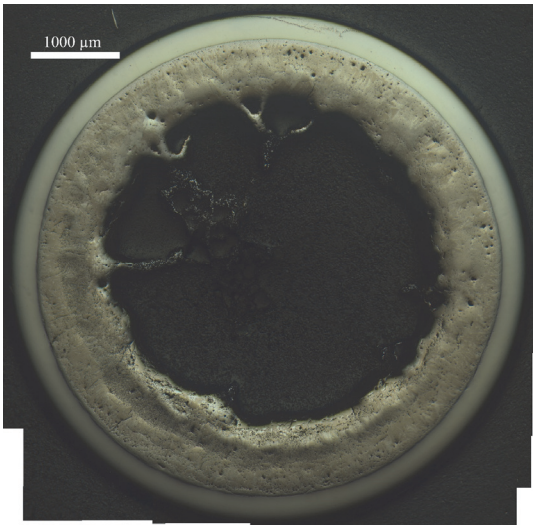

Figure 23. Transverse cross section of AFC-3C R2 (U-10Mo, 55% smear density, annular, He bonded).

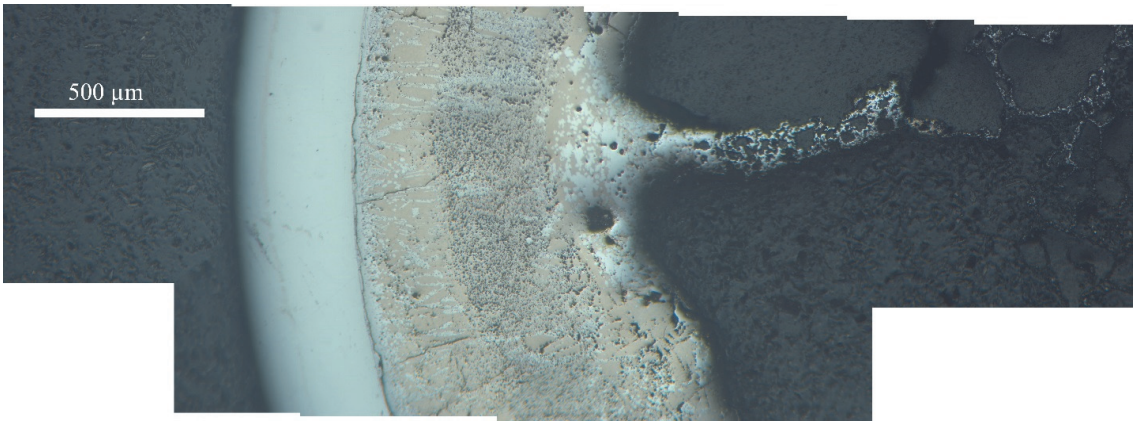

Figure 24. Higher magnification detail of radial microstructure in AFC-3C R2.

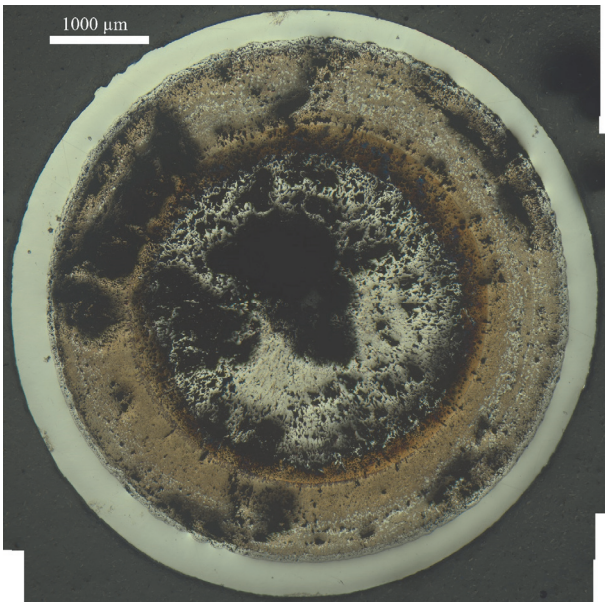

Figure 25. Transvers cross section of AFC-3C R3 (U-10Zr, 65% smear density, solid, sodium bonded).

Figure 26. Higher magnification detail of radial microstructure revealed in AFC-3C R3.

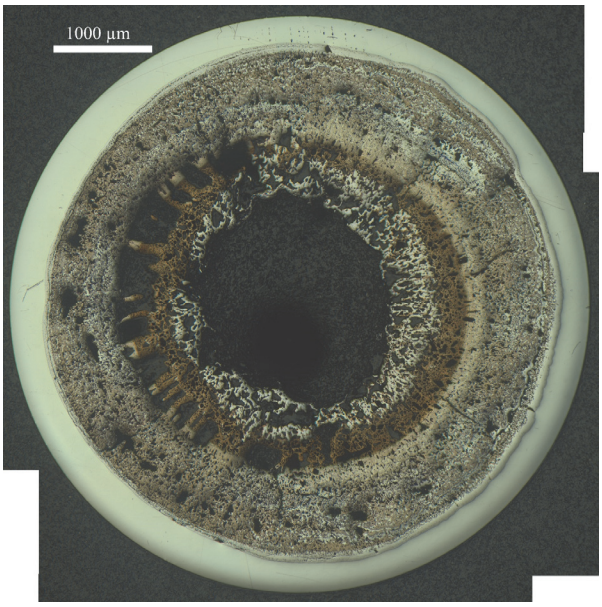

Figure 27. Transverse cross section of AFC-3C R4 (U-10Zr, 55% smear density, annular, He bonded).

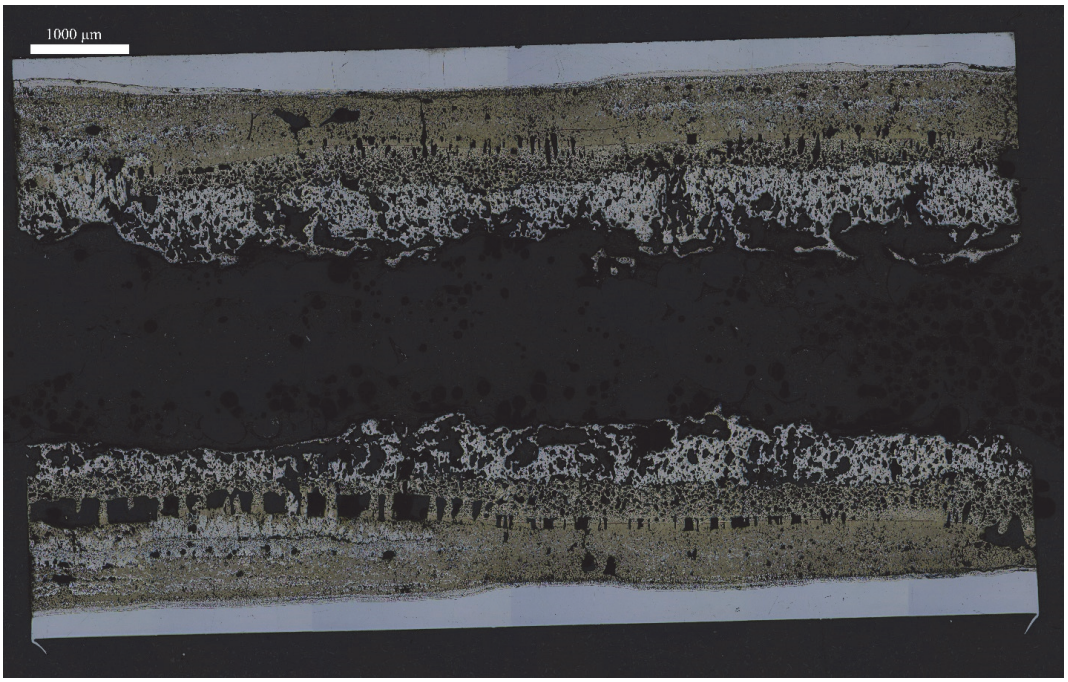

Figure 28. Longitudinal section of AFC-3C R4 taken 19 mm from the bottom of the fuel slug. Fuel slug center and bottom towards the left side of the image.

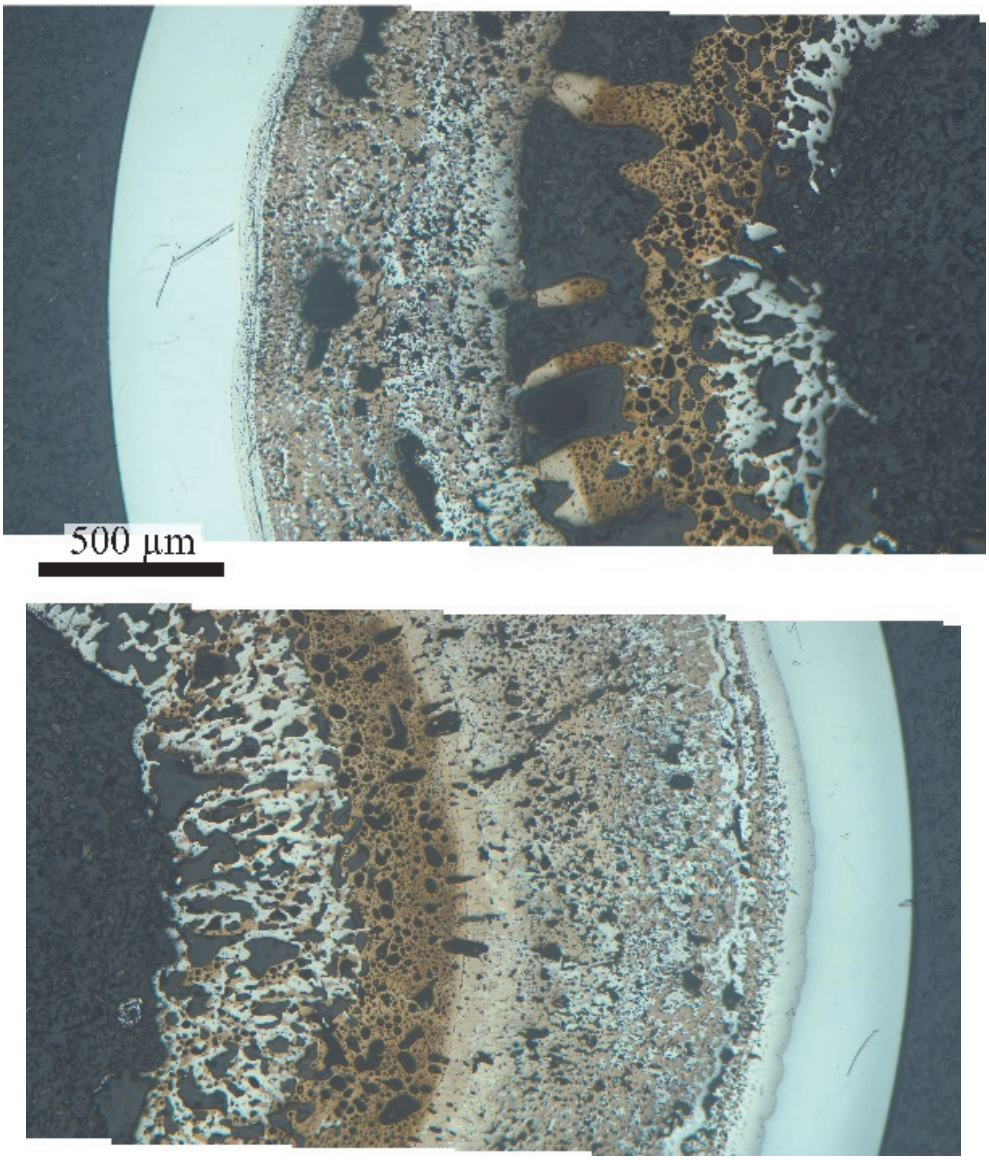

Figure 29. Higher magnification detail of the radial microstructure of AFC-3C R4.

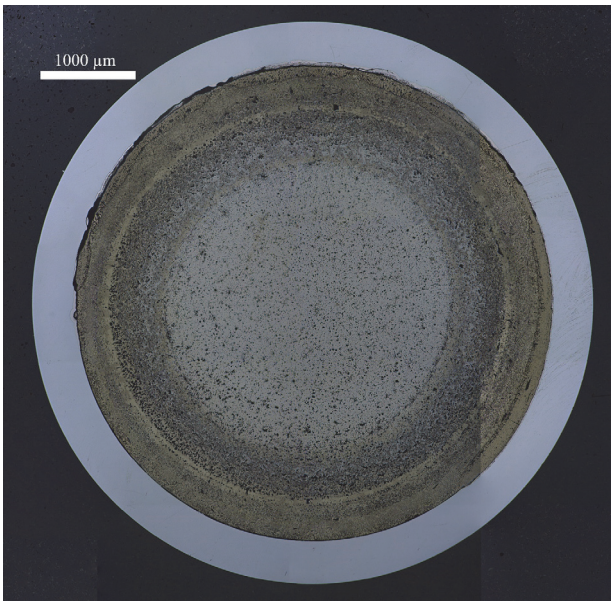

Figure 30. Transverse cross section of AFC-3C R5A (U-1Pd-13Zr, 75% smear density, solid, sodium bonded).

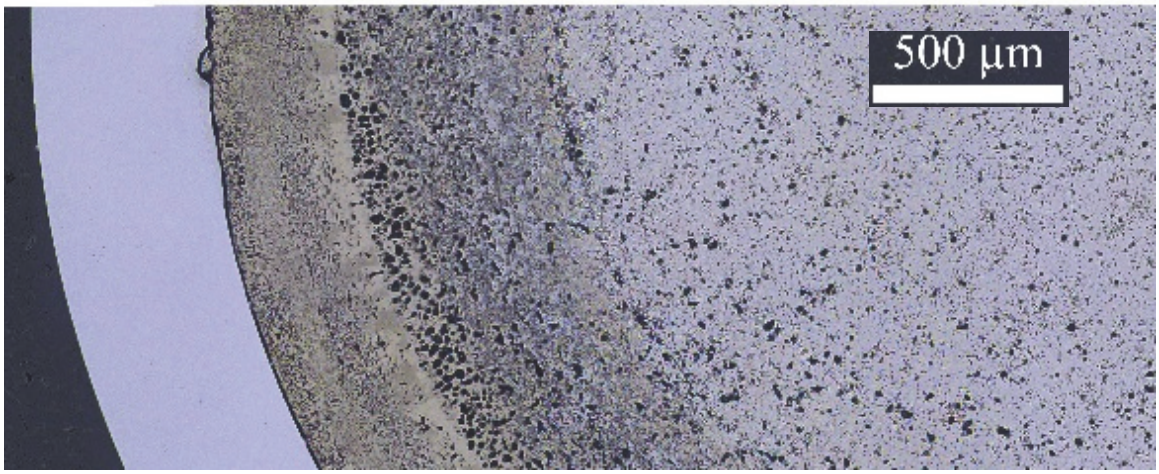

Figure 31. Higher magnification detail of the radial microstructure of AFC-3C R5A.

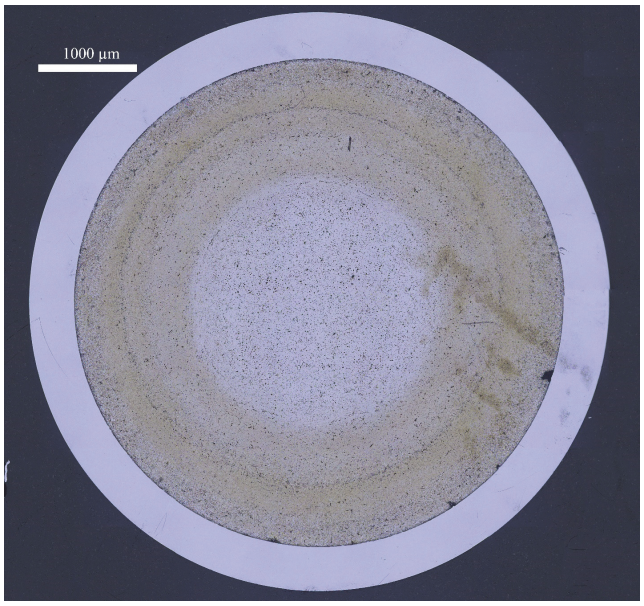

Figure 32. Transverse cross section of AFC-3C R5B (U-2Pd-13Zr, 75% smear density, solid, sodium bonded).

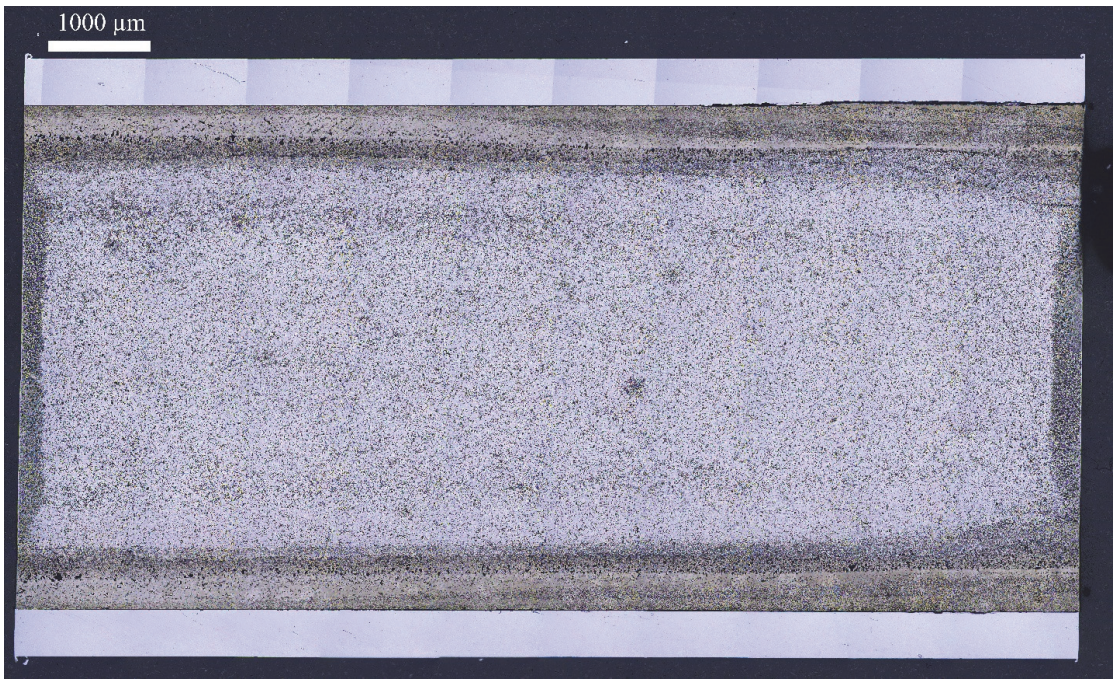

Figure 33. Longitudinal section of AFC-3C R5B taken 19.8mm above the bottom of the stacked AFC-3C R5 fuel slugs. Fuel slug center and bottom towards the left side of the image.

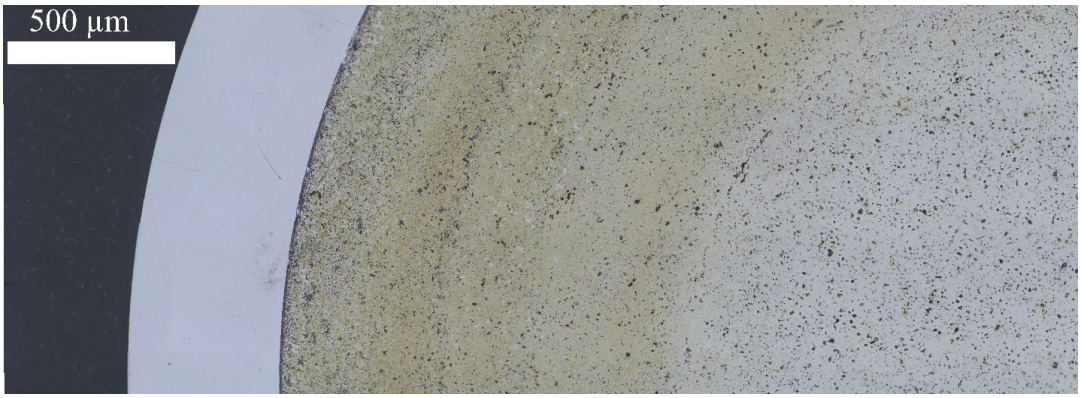

Figure 34. Higher magnification detail of the radial microstructure of AFC-3C R5B.

Figure 35. Transverse cross section of AFC-3D R1 (U-10Zr, 55% smear density, annular, He bonded).

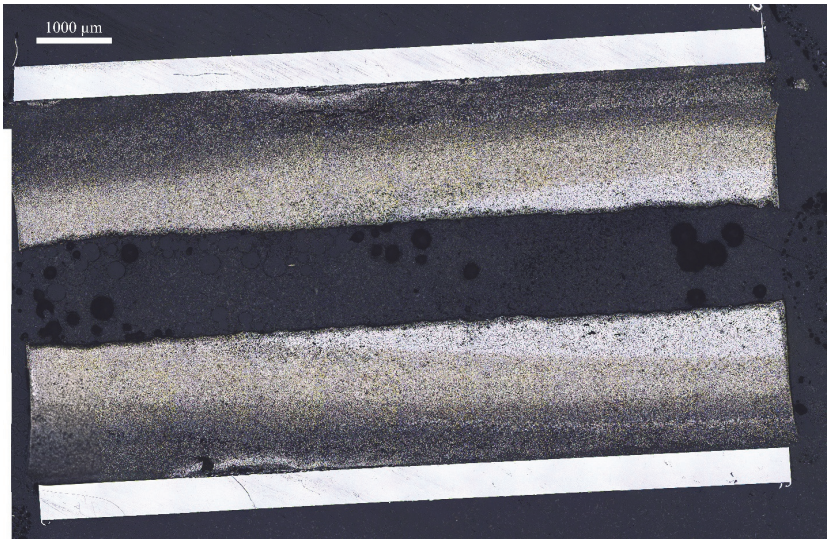

Figure 36. Longitudinal section from AFC-3D R1 taken 25 mm above the bottom of the fuel slug. Fuel slug center and bottom towards the right of the image.

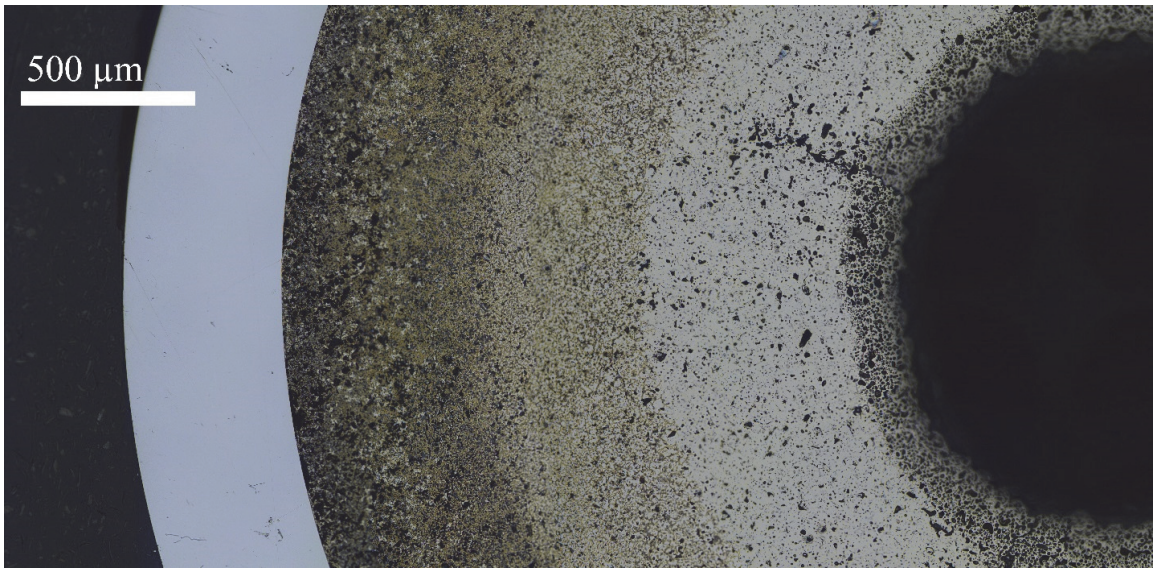

Figure 37. Higher magnification detail of the radial microstructure of AFC-3D R1.

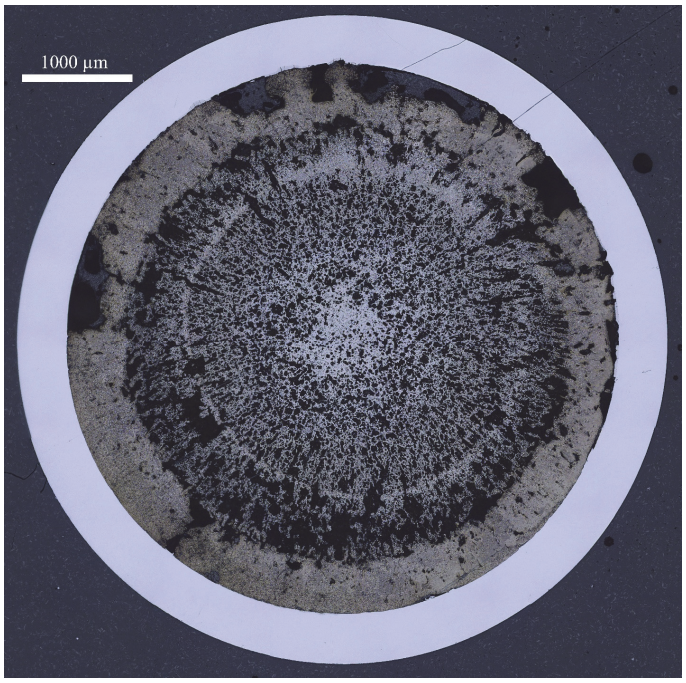

Figure 38. Transverse cross section of AFC-3D R2 (U-4Pd-13Zr, 55% smear density, solid, Na bonded).

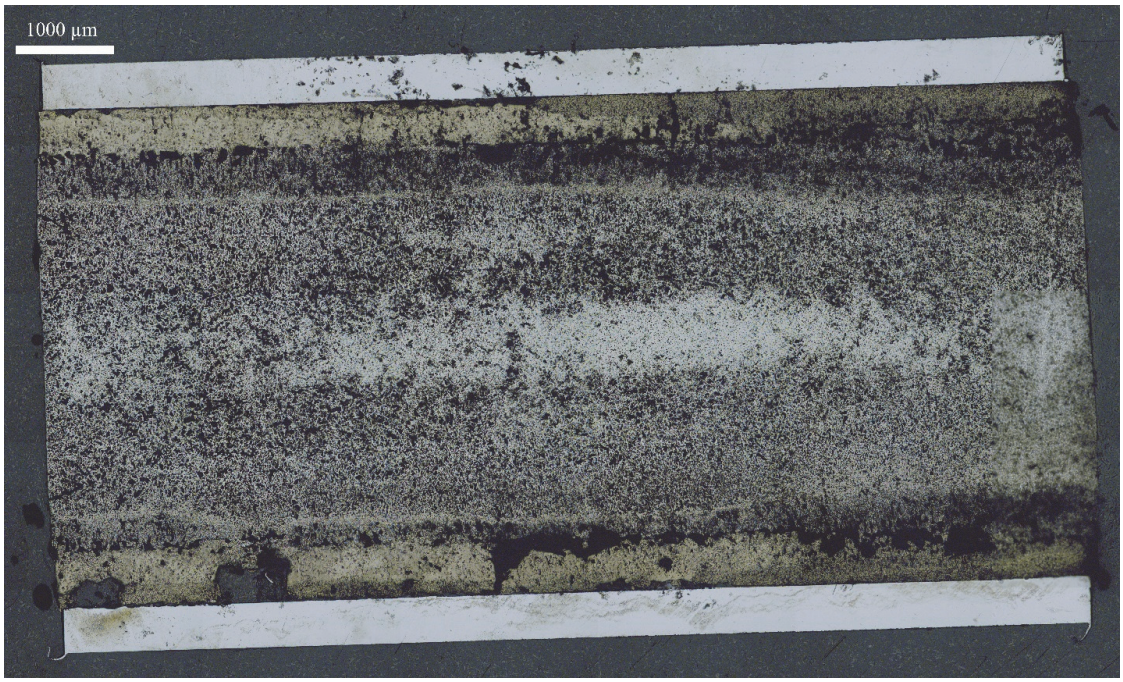

Figure 39. Longitudinal Section from AFC-3D R2 taken 21 mm above the bottom of the fuel slug. Fuel slug center and bottom towards the left of the image.

Figure 40. Transverse cross section of AFC-3D R3 (U-10Mo, 55% smear density, solid, Na bonded).

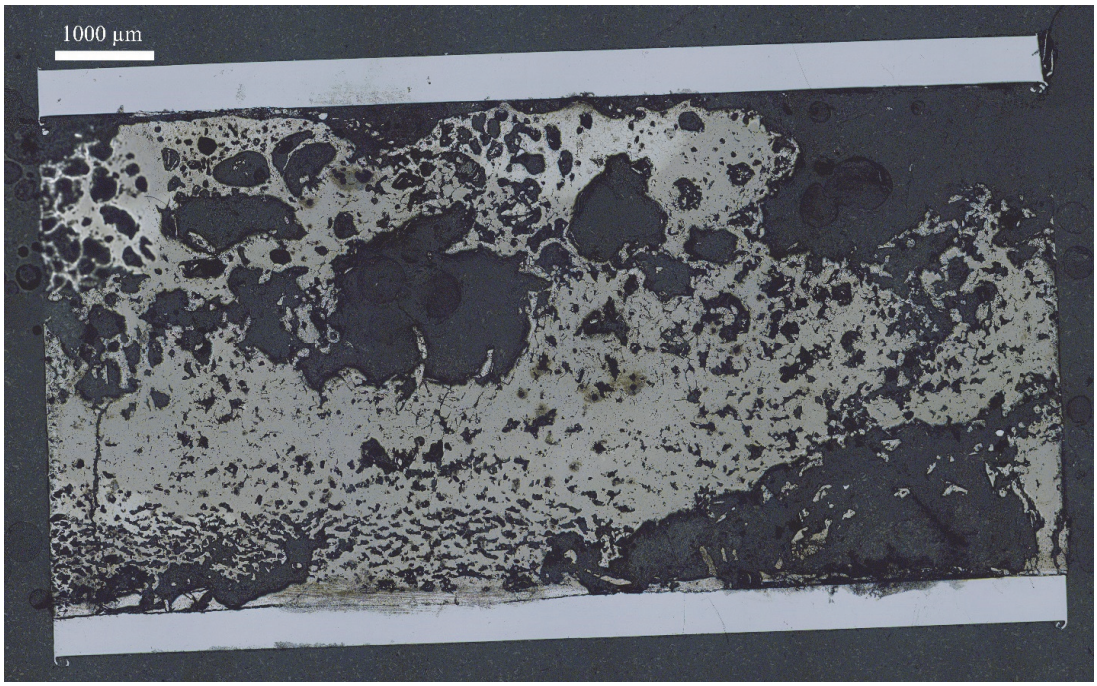

Figure 41. Longitudinal section from AFC-3D R3 taken 27 mm above the bottom of fuel slug. Fuel slug center and bottom towards the left of the image.

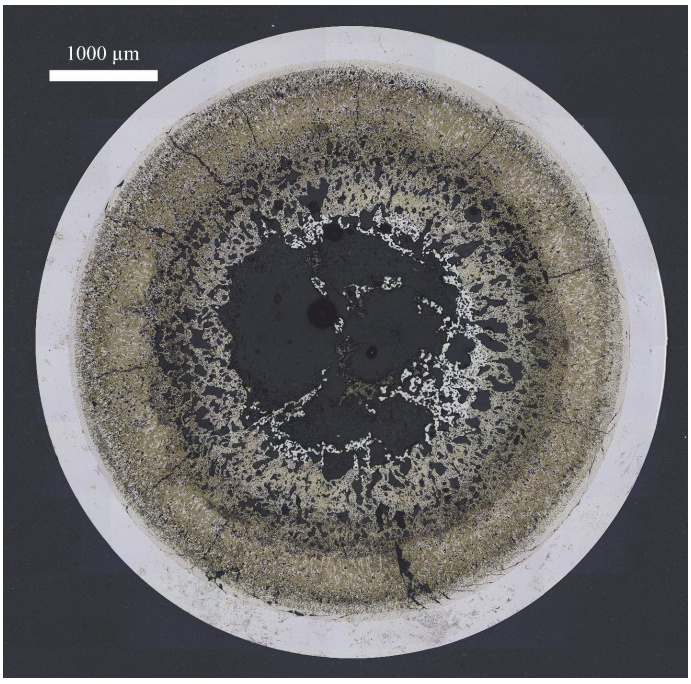

Figure 42. Transverse cross section of AFC-3D R4 (U-10Mo, 55% smear density, annular, He bonded).

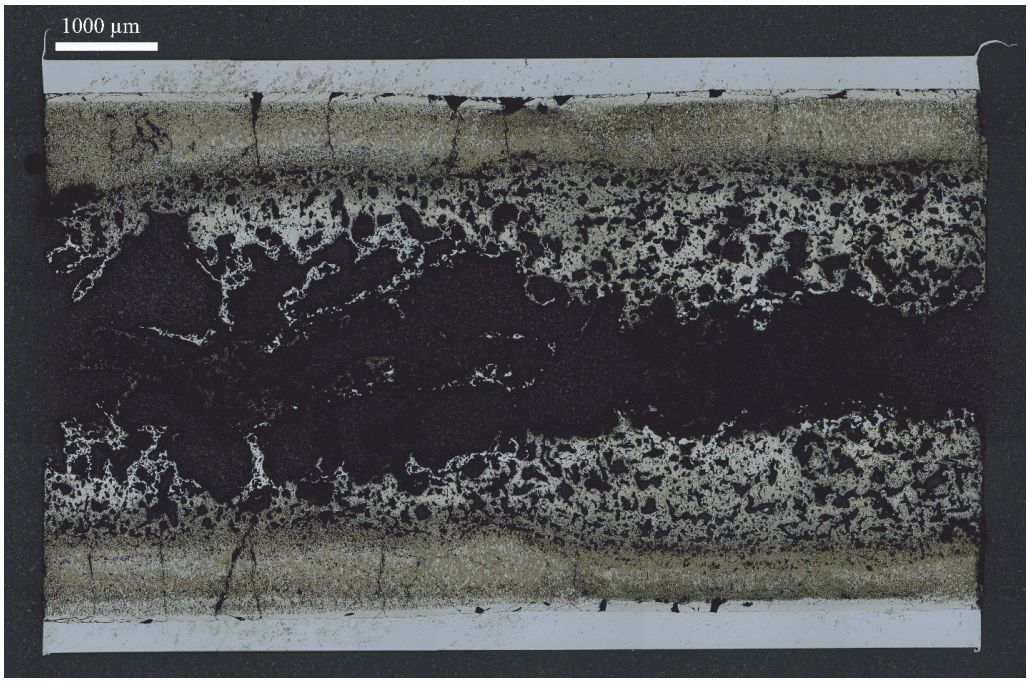

Figure 43. Longitudinal section from AFC-3D R4 taken 21 mm above the bottom of the fuel slug. Center and bottom of the fuel slug towards the left of the image.

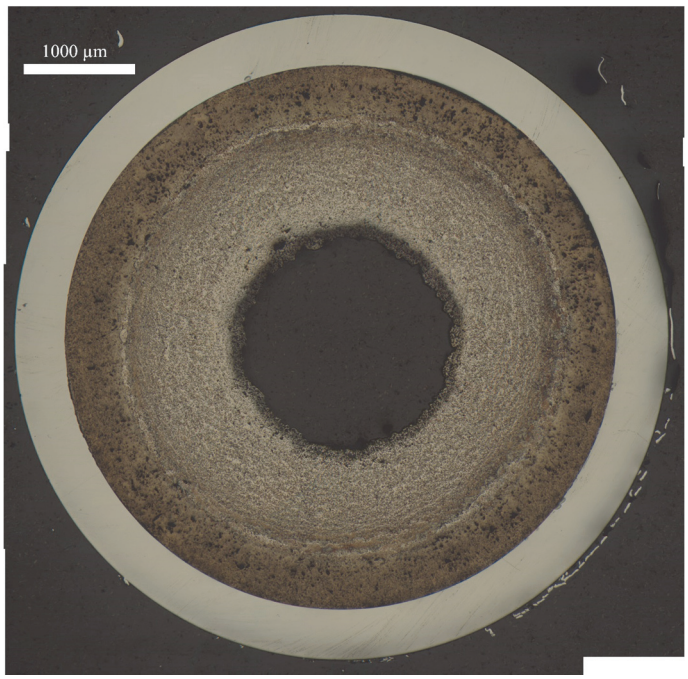

Figure 44. Transverse cross section of AFC-3D R5 (U-4Pd-13Zr, 55% smear density, annular, He bonded).

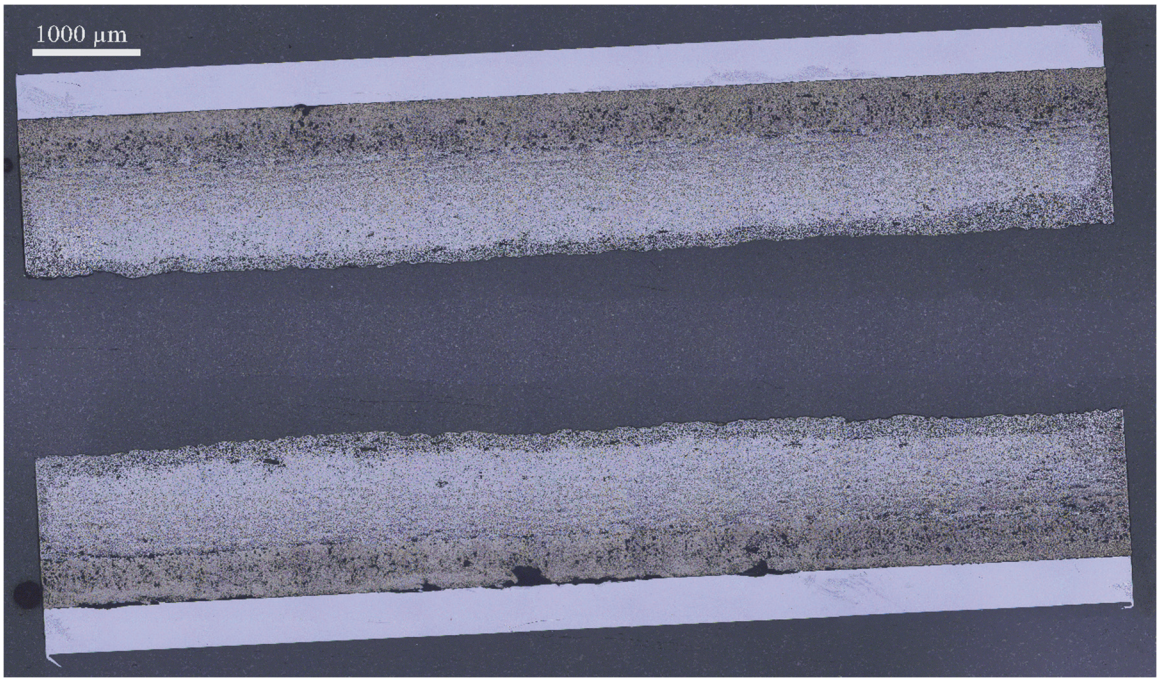

Figure 45. Longitudinal section from AFC-3D R5 taken 24.5 mm above the fuel slug bottom. Fuel slug center and bottom towards the right side of image.

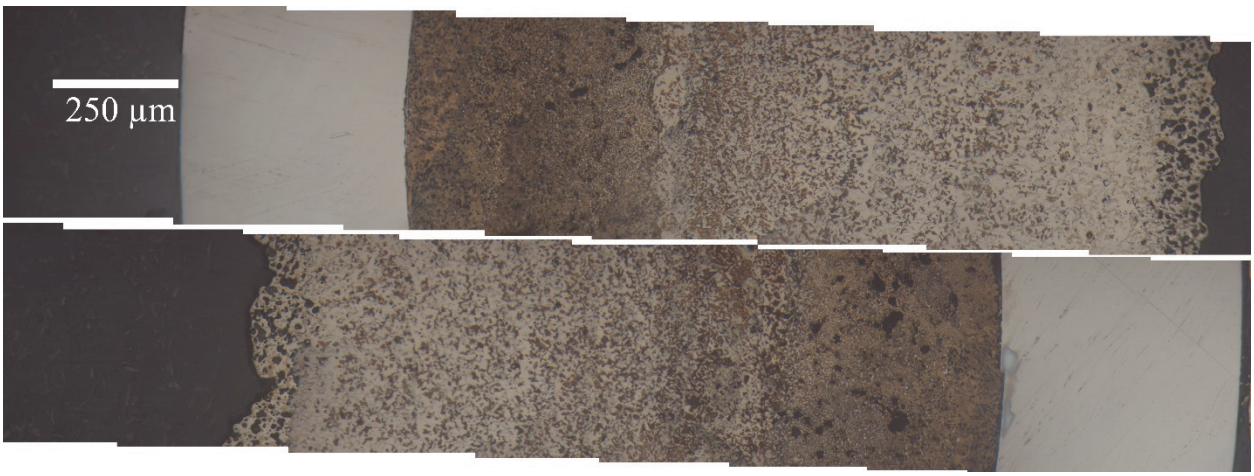

Figure 46. Radial microstructure detail of AFC-3D R5.

3.2 Discussion

The AFC-3C and FC-3D test are in many ways 10 different loosely connected experiments. The temperatures experienced by AFC-3C complicate meaningful interpretation of these rodlets; the irradiation conditions of these rodlets tend to fall outside of historical experience. The irradiation temperatures of AFC-3D were more reasonable and facilitate interpretation of the PIE data in terms of the historical literature. Interpretation of the PIE falls into 4 broad categories: U-Mo fuels, U-Zr fuels, Annular Fuel, and Pd Bearing Fuel. The AFC-3C and 3D tests will be evaluated through these 4 catagories subsequently. The key performance criteria considered will be swelling, fission gas release, and FCCI.

3.2.1 U-Mo Fuels

There were 4 U-10Mo alloy fuels irradiated in these experiments. Early in metal fuel development for fast reactors, U-Mo alloys were considered [5,6] and, subsequently, have been considered to possibly have favorable properties for high burnup and transmutation applications [28]. The most significant use of U-10Mo fuel was in the Mark II fuel pins of the Dounreay Fast Reactor. This fuel easily achieved burnups in the 2-3% range, but cladding temperatures were limited to 480°C. An undesirable increase in cladding thickness was thought necessary to increase the fuel performance (higher burnup, higher temperature) [6]. Unfortunately, most of the historical data are either very low burnup (<1 %FIMA) and not against iron-based cladding. There is some knowledge from EBR-II testing that U-Pu-Zr alloys react less with austenitic stainless steels than U-Pu-Mo alloys [29], but there were no published data definitively demonstrating this experience. That changed with the publication of the AFC-3A and AFC-3B PIE that showed definitive and significant interaction between HT-9 cladding and U-10Mo fuel at sodium fast reactor relevant temperatures [9]. The results from AFC-3C and AFC-3D generally support the observations from AFC-3A and AFC-3B.

The PICT history for the U-10Mo rodlets is an important context for interpreting the observed results from PIE. Refer to Figure 2 and Figure 3 to see the PICT history of these rodlets. AFC-3C R1 and R2 spent their entire irradiation above 590°C, which is expected to enhance FCCI. AFC-3D R3 was above 600°C for the first cycle of irradiation, but was at about 560°C for the second cycle of irradiation. AFC-3D R4 was near but never exceeded 600°C for its first irradiation cycle, and it never exceeded 560°C in the 3 cycles that followed.

Three of the four U-10Mo rodlets experienced fairly significant axial growth (3C R1-18%, 3C R2-11%, 3D R3-19%; see Table 3) compared to U-Zr alloys (6% or less). The exception is AFC-3D R4 which only had 5% axial growth. The increased axial swelling may be due to the cubic crystal structure of U-10Mo at all relevant temperatures. Non-cubic phases of U and U-Zr have been observed to release more fission gas than cubic phases [30], and fission gas is the driving force for swelling [31–33]. The lower fission gas release in U-10Mo can thus explain some of the enhanced axial swelling. Fission gas release in the high swelling U-10Mo pins tends to be lower compared to AFC-3D R4 (see Table 4). This is most apparent in AFC-3D R3, which only released 40-50% of fission gas and had 19% axial swelling, while 3D R4 released 64-70% of fission gas and had 5% axial growth.

Overall, the U-Mo gamma spectrometry behavior is similar to historical patterns observed from U-Zr fuel. The odd behavior of Ce-144 where it spikes in the center of the fuel slug in Figure 16 may be due to features similar to the significant interaction and cracking seen in Figure 43. Further evidence of lanthanide attack of the cladding can be seen in the distribution of CePr-144 in Figure 19d for AFC-3D R4. This is significant for U-10Mo fuel performance because lanthanide-driven FCCI is not usually observed in U-Zr fuel until much higher burnups. This indicates cladding wastage in U-10Mo is occurring from both U-Fe interactions and lanthanide-Fe interactions even at moderate burnup.

The observed FCCI in all 4 U-Mo pins is significant. This is clearly seen in Figure 20, Figure 21, and Figure 22 for 3C R1, Figure 23 and Figure 24 for 3C R2, Figure 40 and Figure 41 for 3D R3, and Figure 42 and Figure 43 for 3D R4. The amount of FCCI observed is somewhat expected given the temperatures experienced by the fuel although the interaction in U-Zr, that saw similar temperatures, was less in most cases. In AFC-3C R1, there is at least 80 µm of cladding wastage. Similarly, there is 80-90 µm of wastage in AFC-3C R2. The wastage in 3D R3 is asymmetric, but it is also more severe at about 100 µm of cladding wastage. The low smear density, but solid fuel geometry, may have enhanced interaction where fuel was in contact with the cladding, but there was no interactions where only sodium was in contact with the cladding. For 3D R4, the wastage was most severe at about 110 µm. This pin was in the reactor longer than any of the other U-10Mo pins, but it also was only exposed to PICT temperatures of 600°C or less. This result again shows the limitations of U-10Mo clad in a ferritic alloy as a fuel for a sodium fast reactor with typical outlet temperatures.

Constituent redistribution should also be mentioned. One of the proposed benefits of U-10Mo is the lack of constituent redistribution in this fuel. There are no phase transitions from room temperature to operating temperatures in this alloy and, therefore, no driving force for constituent redistribution as is typically seen in U-Zr alloys. There does not appear to be any constituent redistribution in U-10Mo based on these irradiations or the AFC-3A/B irradiations. AFC-3C R1 is the best example of this. However, the amount of Fe interaction seen in the 3C 3D rodlets complicates interpretation of the optical microscopy.

3.2.2 U-Zr Fuels

Six of the AFC-3C 3D rodlets were U-Zr alloys with and without Pd additives. The Pd additives will be discussed in a subsequent section. Many of these rodlets performed very well while some performed no better than the U-10Mo fuel.

The axial growth for all these rodlets is low compared to the U-10Mo. The change in cladding diameter is low in all these pins except AFC-3C R3 and 3C R5. Based on the temperatures of these rodlets, this is likely thermal creep in the cladding. The axial behavior of fission products in 3C and 3D rodlets is in line with expectations. The radial distribution of fission product seen in the GECT is also in line with expectations.

The fission gas release for the U-Zr pins is notable. AFC-3C R3, 3C R4, and 3D R1 all have fairly high fission gas release. Low smear density fuel like AFC-3C R3 has historically had high fission gas release [20], but the fission gas release for solid low smear density fuel in AFC-3B was lower or near 70% [9]. Also, the fission gas release for AFC-3D R2 is in the historical fission gas release band of 70±10%. The high fission gas release of the annular fuel is also expected. Annular fuel should primarily be irradiated with the fuel below the cubic phase transition temperature of U-10Zr in the alpha uranium phase range, and alpha uranium is expected to have high fission gas release [30]. Fission gas release for AFC-3D R5 is also in the historical range and not elevated like the other annular pins; this may be due to the relatively low fission density in this pin or possibly an effect of the Pd and extra Zr present in this fuel. The lower fission gas release in AFC-3C R5 is expected due to its low fission density of just over 5×10^{20} fissions per cm^3.

Both AFC-3C R3 and AFC-3C R4 were irradiated at elevated temperatures with PICT exceeding 600°C for the entire first cycle of irradiation. It is not surprising that FCCI has occurred in these pins (see Figure 25 and Figure 27). Constituent redistribution and smear density also likely enhanced FCCI in these pins. Based on the microstructures in Figure 25 and some initial scanning electron microscopy (SEM) of U-10Zr fuel irradiated in AFC-3A, constituent redistribution may have caused most of the Zr to migrate away from the cladding. Once this occurred, the free uranium would have interacted with the cladding readily at the PICTs predicted in Figure 2. Over the first cycle of irradiation, the entire fuel pin is above 615°C, indicating all the Zr in this fuel pin would have been dissolving into pockets of gamma U-Zr [34]. Similar reactions would have occurred in AFC-3C R4.

This did not happen in AFC-3C R5, in spite of the PICT being higher than in 3C R3 or 3C R4. There is some interaction in AFC-3C R5A (Figure 30), but it is not severe, and there is little obvious interaction in AFC-3C R5B (Figure 32). Based on the lack of interaction, some Zr must have remained near the outer radius of the fuel. The exact reason why Zr did not migrate further in this pin is still under investigation.

The AFC-3D pins with the lower PICT fared much better than the AFC-3C pins. AFC-3D R1 had excellent performance, especially compared to AFC-3D R4 which has the same irradiation history. The 3 colored bands in Figure 35 show some constituent redistribution has occurred, and these same bands are present in the longitudinal microscopy (Figure 36). Electron microscopy of some sort (SEM or EPMA) would clarify the compositions, but some hypotheses on the compositions can be made based on the U-Zr phase diagram. The outer band in the fuel that extends from the outer radius inward about 600 μm is likely uranium with small amounts (~2 atom %) of Zr. The next band inwards that extents about 400 μm further into the fuel appears to be a mixture of the outer band compositions with the inner band

composition. The inner most band, from 1000 µm into the fuel to the annulus, all appears to be single phase in the optical microscopy. This phase was likely gamma-(U,Zr) under irradiation and is now likely delta UZr_2. The success of 3D R1 versus the failure of 3C R4 will be studied further. At this time, the only clear difference is the small 20-40°C difference in PICT that separates the drastic difference in performance.

3.2.3 Annular Fuel

Most of the observations from the annular fuel were discussed in the previous two sections. There are, however, some general differences between AFC-3A/B and AFC-3C/D that proved significant in annular fuel performance. In AFC-3A/B, annular fuel slugs were cast into annular molds, the quartz molds were broken off the slugs, and the slugs were placed in the pins with a significant gap (>50 µm) between the fuel slug and the cladding. In AFC-3C/D, the fuel slugs were machined after casting to create a small (<25 µm) well-known gap between the fuel and the cladding. This significantly improved performance, even at elevated temperatures. This extra fabrication cost is an important trade-off between helium bonding and sodium bonding that must be considered when evaluating fuel designs for future reactors.

The behavior of the annulus is also notable. In AFC-3A/B the annulus in the U-10Zr and U-4Pd-10Zr fueled rodlets essentially closed, while the annulus in the U-10Mo rodlet stayed open. This is thought to be due to a diffusion of Zr up the temperature gradient that does not exist in the U-10Mo fuel. This theory generally holds well against the AFC-3C/D data, especially AFC-3C R2, except the annulus in AFC-3D R4 has closed to some degree. However, upon examining the neutron radiography (Figure 9), the amount of closure seen in Figure 42 may be a local effect. The annulus in Figure 43 over about 10 mm of fuel shows little closure.

The closure of U-Zr is much more significant. This is likely due to the combined effect of fission gas swelling and the diffusion phenomenon that drives Zr constituent redistribution. In previous tests, the closure of the annulus in AFC-3A R4 was nearly complete (Figure 47). Closure did not occur in AFC-3C R4 (Figure 27). Closure also did not occur in AFC-3D R1 and is illustrated for both the longitudinal section and transverse section in Figure 48. The closure was remarkably consistent over the entire length observed in Figure 48a. The lack of closure in AFC-3C R4 and AFC-3D R1 may be due to complete fission gas release in these pins (85-100%) which is contrary to the incomplete fission gas release in AFC-3A R4 (37%). Similar behavior to AFC-3D R1 was also observed for AFC-3D R5 (Figure 44 and Figure 45).

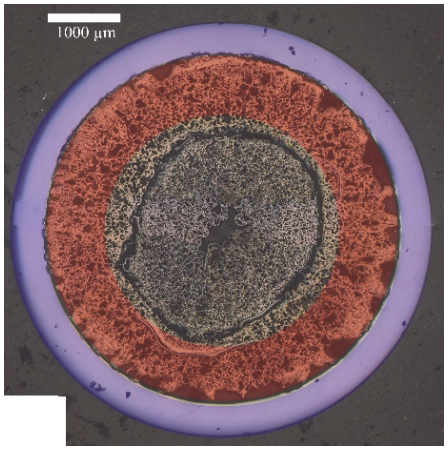

Figure 47. AFC-3A R4 U-10Zr, 55% smear density, annular fuel transverse cross section with blue shading showing the original cladding and red shading showing the original fuel dimensions.

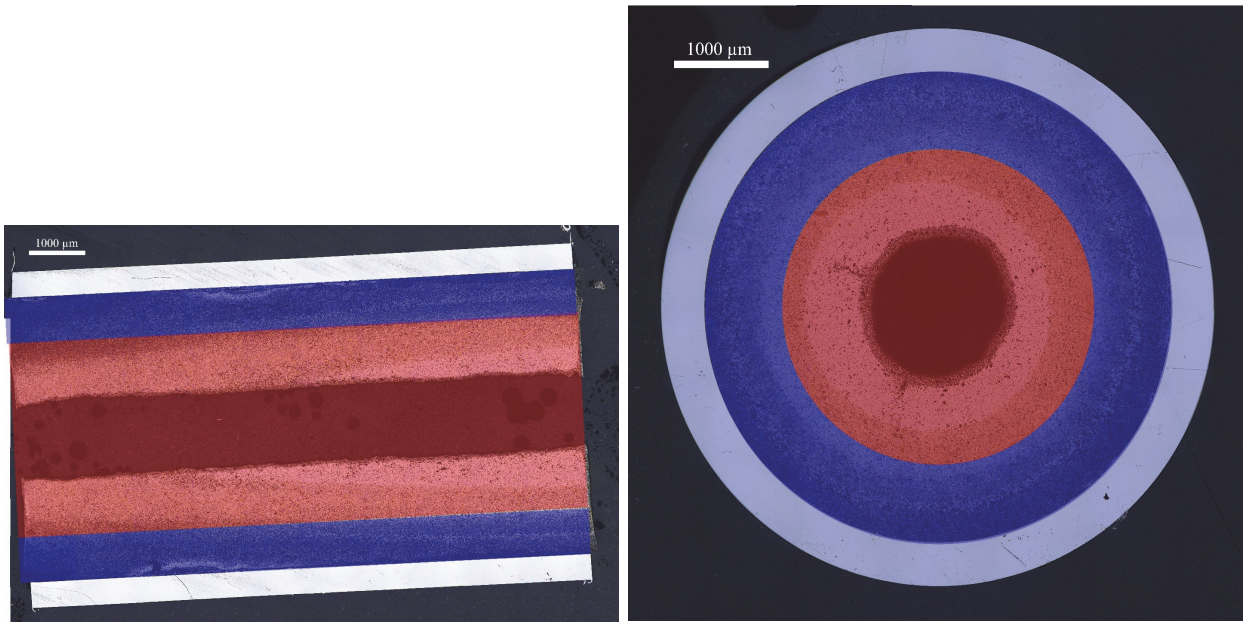

(a) (b)

Figure 48. The closure of the annulus in AFC-3D R1 where the blue shading shows the original fuel area and the red shading shows the original annulus area for both the longitudinal section (a) and the transvers section (b.).

3.2.4 Pd Bearing Fuel

Palladium has been proposed as an additive to metallic fuel to help prevent lanthanide-initiated FCCI in U-Zr alloys at high burnup [35,36]. This concept was tested in out-of-pile tests, and lanthanide-palladium precipitates have been observed in bot U-5Fs and irradiated U-10Zr [37]. During fabrication, Zr and Pd form a stable intermetallic compound, and Pd was expected to release Zr and form stable intermetallic compounds with lanthanides. This had mixed success in AFC-3A/B [9]. Some of the issues in AFC-3A/B were attributed to Zr-Pd intermetallics that removed Zr from the U matrix, and then the U was more free to interact with the cladding. To help alleviate this problem in AFC-3C/D, additional Zr (13% not 10%) was added to the Pd bearing pins. Overall, this appears to have helped improve performance of these pins. In these tests, the Pd bearing pins do not have any obvious performance difference between U-Zr pins with the same geometry.

4. AFC-4A

The AFC-4A irradiation test was an alloy exploration test. This test explored U-10Mo, U-10Zr, and U-10MTZ with and without Pd. The MTZ alloy is 50% Mo, 43%Ti, 7% Zr by weight. The goal of this test was to investigate an alloy of Mo, Ti, and Zr that could be alloyed with U to form a compound that is single phase and cubic at irradiation temperatures. This would prevent constituent redistribution. By retaining Zr in this alloy, it was hoped that alloy would also avoid FCCI between the fuel alloy and the cladding that is observed with U-Mo alloys. The irradiated alloy is 34.8 atom % Mo, 60 atom % Ti, and 5.2 atom % Zr. Its location in the Mo-Ti-Zr phase diagram is shown in Figure 49 by a star. The entire region that contains the star is single phase cubic. While it was not irradiated, it may have been more beneficial to be on the higher Zr portion of the Mo-Ti-Zr phase diagram as shown by the X in Figure 49. An alloy in the Zr rich region may have behaved similarly to U-Zr alloys. The irradiated alloys have acted similar to prior experience with U-10Mo irradiations. This is demonstrated in the optical microscopy of this fuel in the subsequent sections. This poor performance was exasperated by the temperatures experienced by the fuel in these irradiations also.

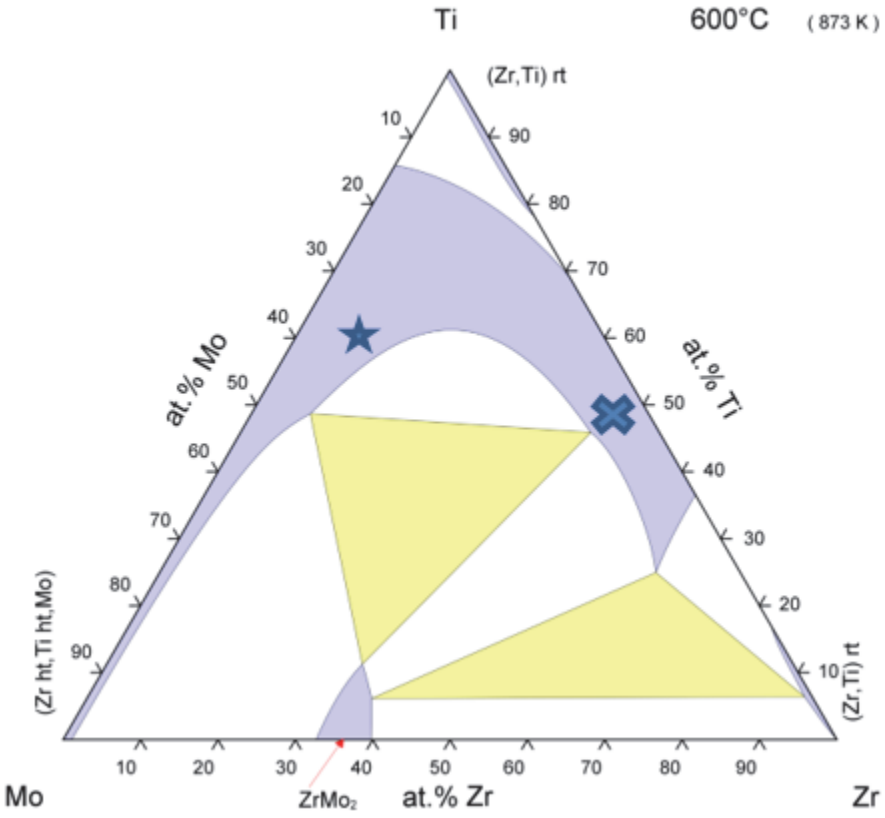

Figure 49. Phase diagram of Mo-Ti-Zr system at 600°C, with a star showing the irradiated composition and an X showing an alternative composition.

4.1 Results from PIE

As with AFC-3C and AFC-3D, AFC-4A was sent through standard PIE to determine the engineering scale performance of the fuel. The results from neutron radiography, dimensional inspection, gamma spectrometry, fission gas release, burnup, and optical microscopy are summarized in this section. The results are then discussed as a whole. The irradiation conditions of AFC-4A were discussed previously in Section 2.3. As with AFC-3C, the PICT of AFC-4A was higher

4.1.1 Neutron Radiography

Neutron radiography of the AFC-4A rodlets was performed in a similar manner to AFC-3C and AFC-3D. The radiography fixture used for those rodlets was not available for AFC-4A and a simpler fixture was used. Radiographs were taken at 3 different angles 120° apart. The neutron radiography is shown in Figure 50.The rodlets were relatively symmetric except for the top of AFC4A R3 which is shown at 3 different angles in Figure 51. The axial growth for AFC-4A R1 was 0%, 17% for 4A R3, 16% for 4A R4 and 12% for 4A R5. Considering the PICT experienced by these pins, the neutron radiography appears relatively free of a sign of significant fuel degradation.

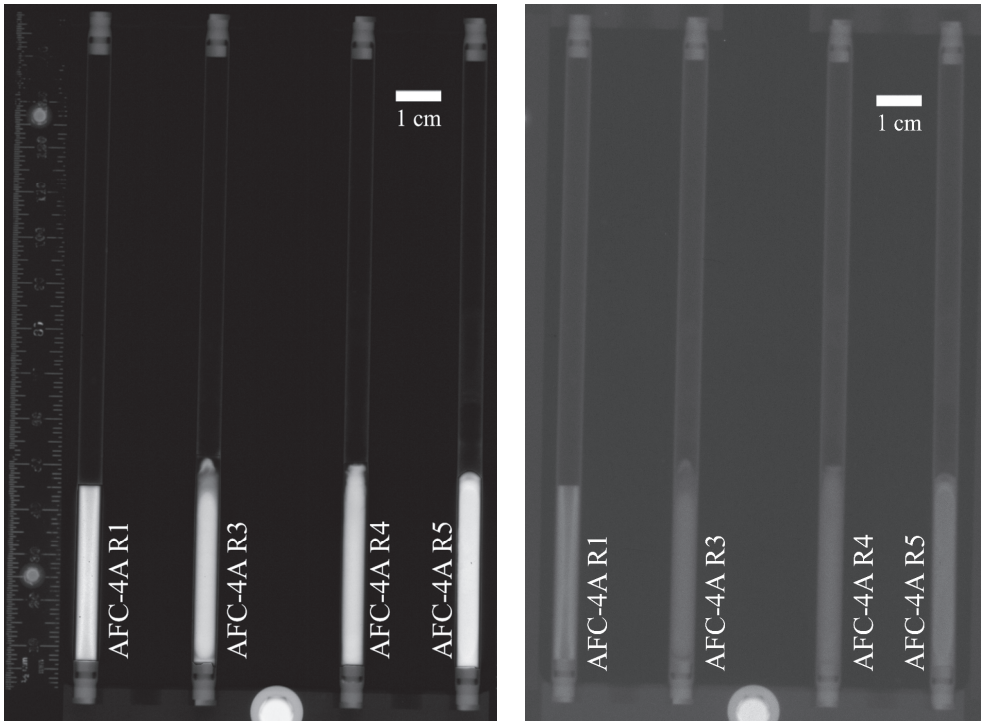

(a) (b)

Figure 50. Thermal (a) and epithermal (b) neutron radiographs of the AFC-4A rodlets.

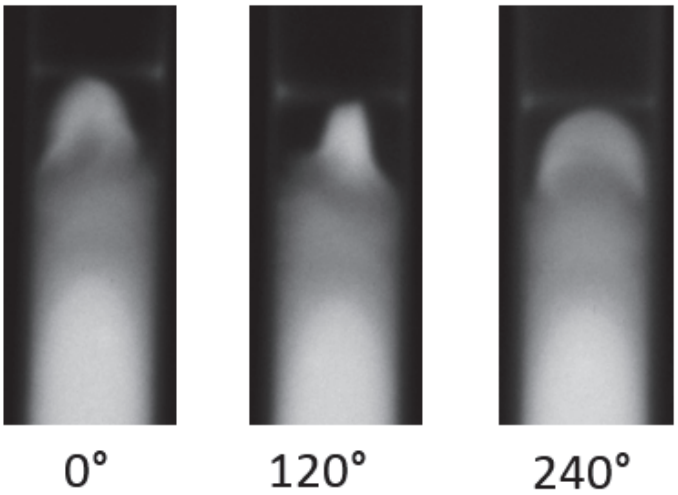

Figure 51. Neutron radiographs of the top of AFC-4A R3 showing the asymmetric behavior of the top of this fuel pin.

4.1.2 Dimensional Inspection

Dimensional inspections of AFC-4A was performed using the US HPRR Plate checker in HFEF. Outside diameter measurements were collected all along the rodlets in roughly 0.5 mm increments and at 36 angles every 5° from the initial scan angle to 175°. Diameter measurements are collected with ±5 µm accuracy. The angle averaged measured diameters for the AFC-4A rodlets are shown in Figure 52. There was some thermal creep of the cladding in the 3 high PICT rodlets (R3, R4, R5). The maximum strain is approximately 0.4%, and the cladding stayed well away from the capsule inner wall.

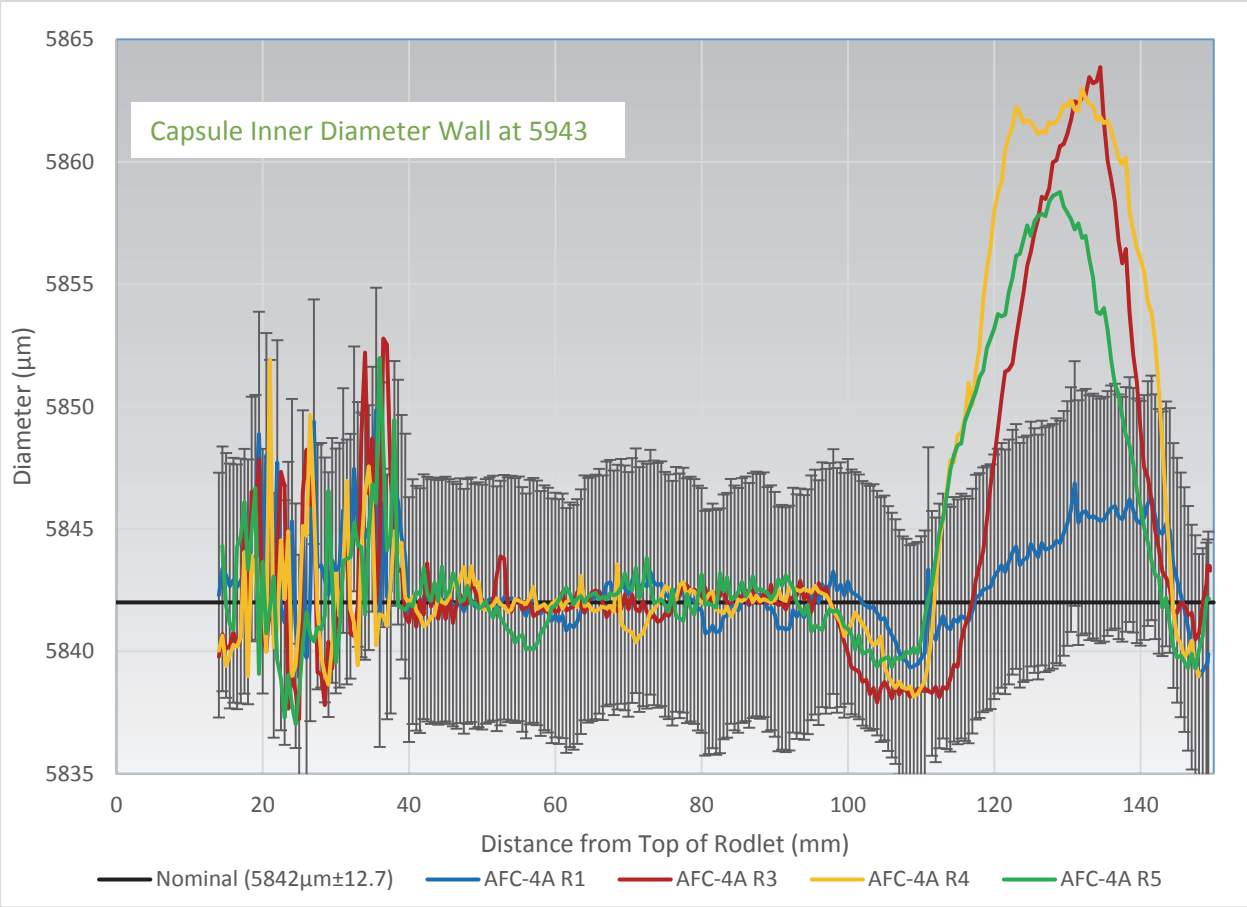

Figure 52. Average diameter of AFC-4A rodlets after irradiation.

4.1.3 Gamma Spectrometry

Gamma ray spectrometry of all of the AFC-4A rodlets was performed using the HFEF Precision Gamma Scanner (PGS). Axial scans were collected every 0.127 cm for 15 minutes live time. Nothing unusual was observed in the axial distribution of fission products for AFC-4A R1 or AFC-4A R5. These pins followed similar patterns to what is typically seen for annular fuel or sodium bonded fuel. The axial distributions of key radioisotopes from AFC-4A R3 and R4 are shown in Figure 53 and Figure 54 respectively. The neutron radiography for these rodlets is also shown to assist in interpretation. The peaks in Mn-54 line shows the location of endcaps and the cladding. In 4A R3, the Cs is dissolved above the fuel near the asymmetric top of the fuel column in the sodium above the fuel. In 4A R4 the Cs is also in sodium above the fuel, but it is also in the plenum. In both rodlets, some Cs has migrated out of the fuel below the bottom of the fuel slug and entered the free space around the endcap. Eu-154 also acts as a volatile in these fuels. In 4A R3, it is above the sodium and in the plenum and below the fuel in the endcap free

space. In 4A R4, it has not transported up into the plenum, which is unusual for Eu-154. The RuRh-106 signal in both fuel pins indicates that noble metal fission products are well integrated into the fuel, which is expected. There are some spikes in the CePr-144 signal in the 4A R3 plot that may indicate enhanced migration of lanthanides to the cladding in these areas. In contrast, the CePr-144 signal in 4A R4 is relatively constant.

The previously discussed GECT technique was also applied to 4A R3 and 4A R4. The Cs-137 distribution for both pins is shown in Figure 55, and the Ru-106 distribution for both pins is shown in Figure 56. The GECT was performed at the center of the fuel column. The Cs-137 appears to be relatively uniformly distributed throughout the fuel which is unusual for metallic fuel. The Ru-106 is arranged in a ring. This may be an indication of Pu-239 fission location or an indication of Ru radial migration. The fission yield for Ru-106 is much higher in Pu-239 fission than in U-235 fission. The Pu fission explanation seems more likely, given the distribution of Zr-95 in both pins shown in Figure 57. The distribution of Ce-144 shown in Figure 58a for 4A R3 appears to match the spike see in Ce-144 activity in Figure 53 that indicates some potential lanthanide attack of the cladding in this rodlet. The distribution of Ce-144 in 4A R4 in Figure 58b shows some possible radial migration of lanthanides in the fuel, but no aggressive cladding attack like what appears to be occurring in 4A R3.

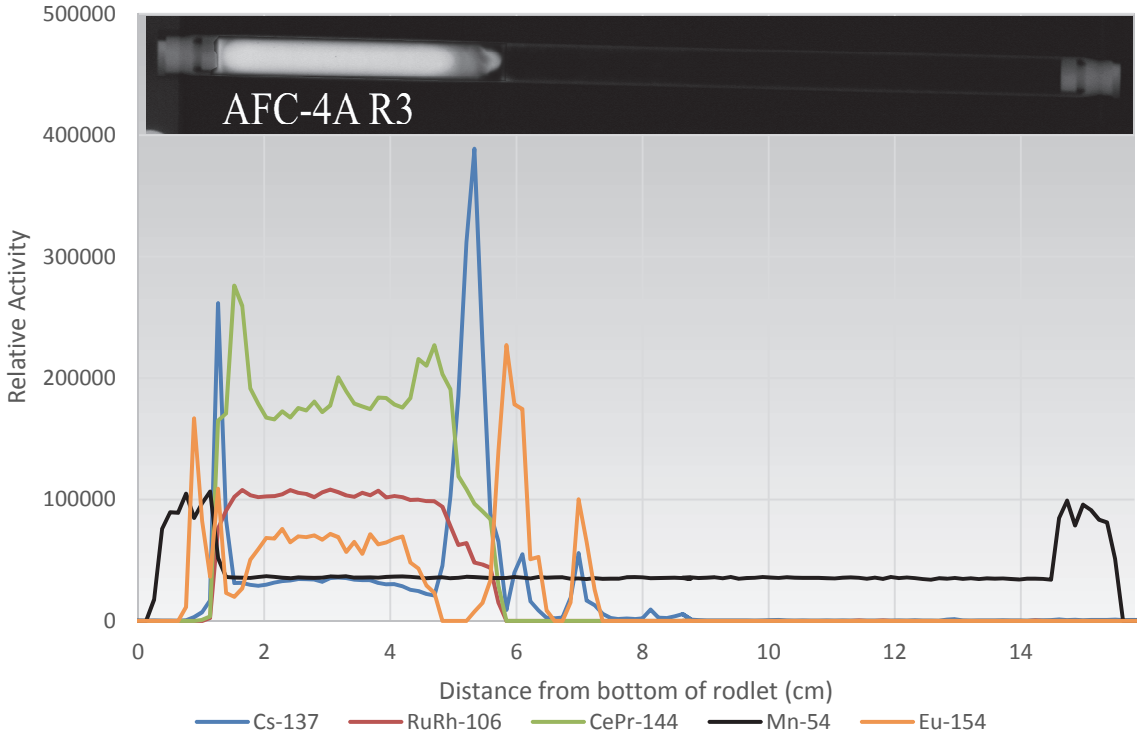

Figure 53. Axial distribution of select gamma emitting radionuclides in AFC-4A R3.

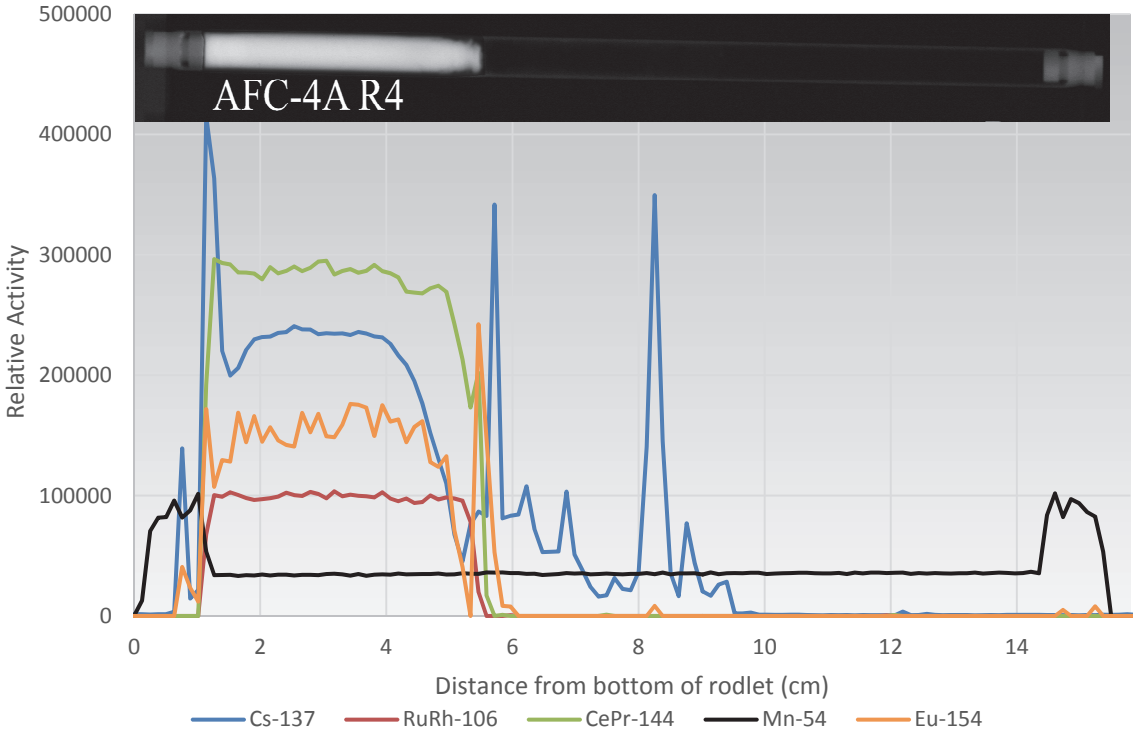

Figure 54. Axial distribution of select gamma emitting radionuclides in AFC-4A R4.

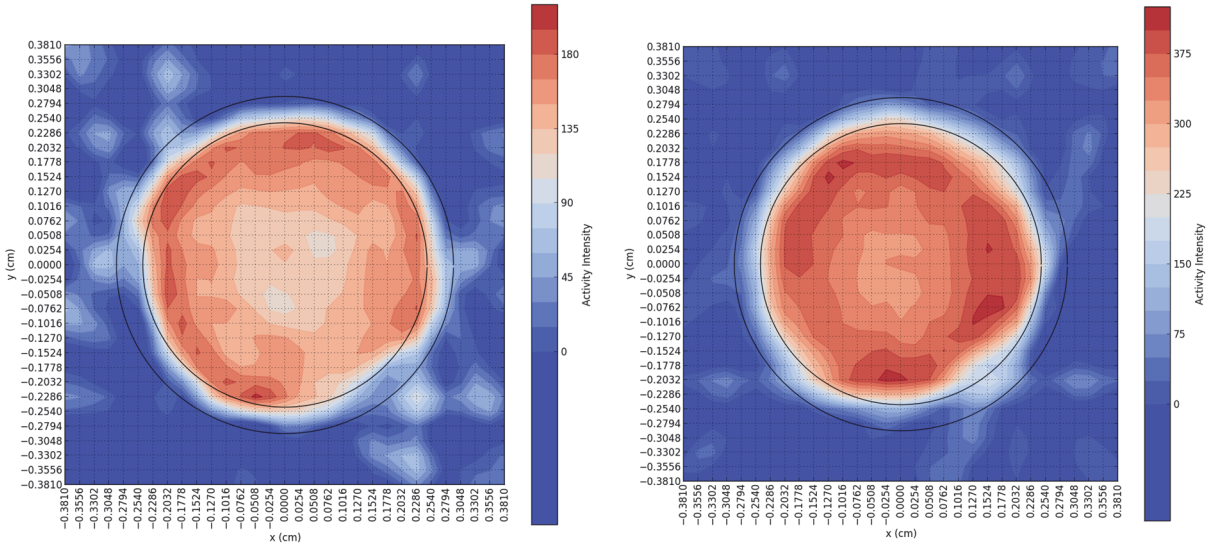

(a) (b)

Figure 55. Cs-137 Distribution in the middle of the fuel zone for AFC-4A R3 (a) and AFC-4A R4 (b).

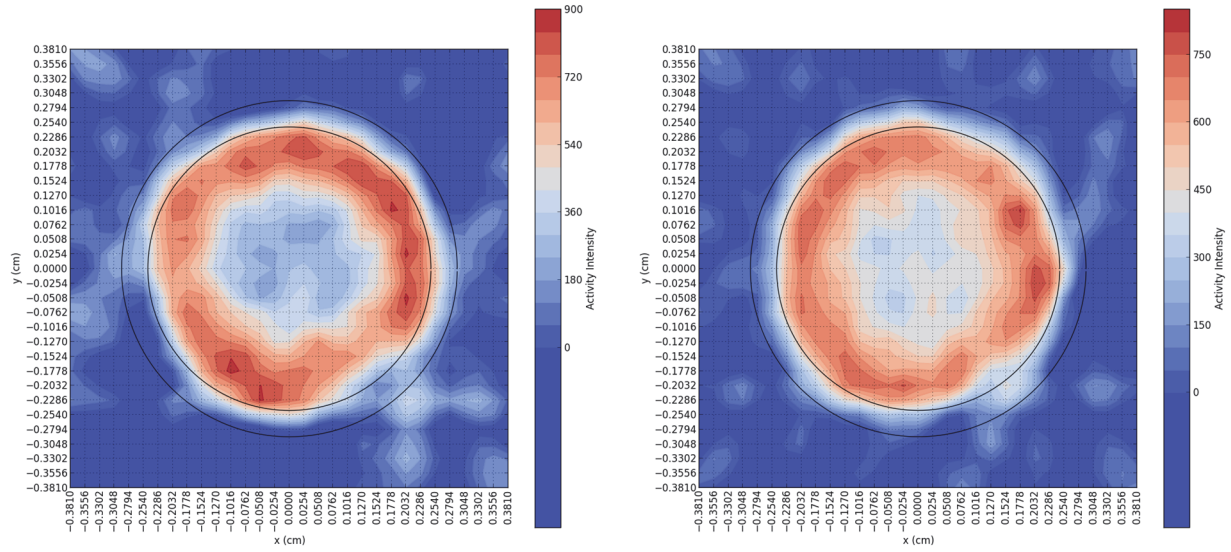

(a) (b)

Figure 56. Ru-106 Distribution in the middle of the fuel zone for AFC-4A R3 (a) and AFC-4A R4 (b).

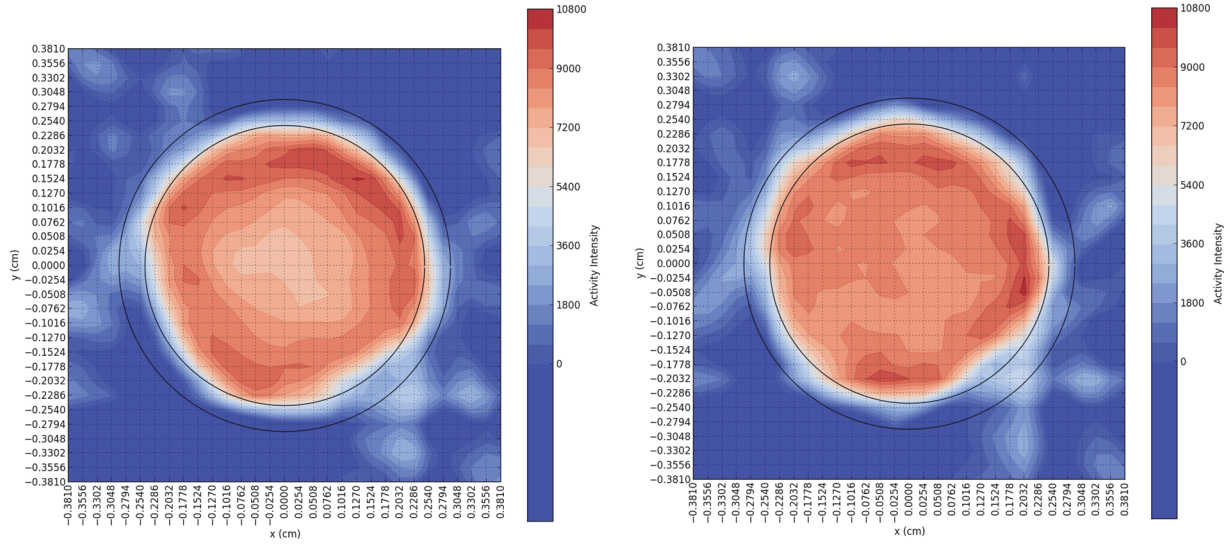

(a) (b)

Figure 57. Zr-95 Distribution in the middle of the fuel zone for AFC-4A R3 (a) and AFC-4A R4 (b).

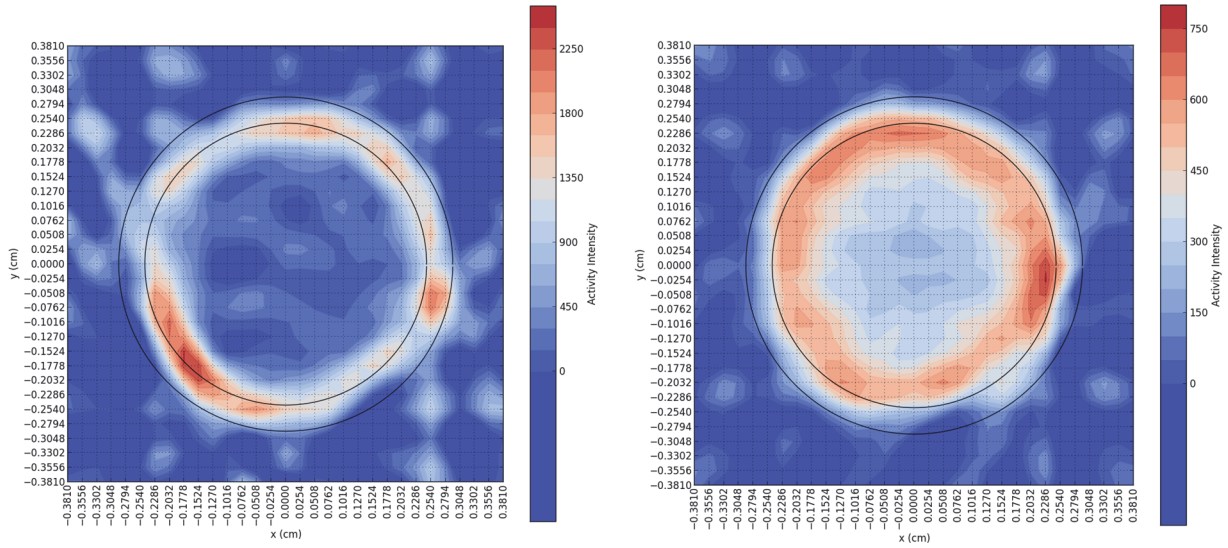

(a) (b)

Figure 58. Ce-144 Distribution in the middle of the fuel zone for AFC-4A R3 (a) and AFC-4A R4 (b).

4.1.4 Fission Gas Release

Fission gases were collected from the rodlets using the HFEF GASR system in the same manner as AFC-3C and AFC-3D. Fission gas analysis was performed by gas mass spectrometry. A summary of the fission gas release results for AFC-4A is shown in Table 6. The first column is the fission gas release based on the predicted number of fissions, and the second column is the fission gas release based on the measured number of fissions based on the mass spectrometry results discussed in Section 4.1.5.

Compared to historic norms, the resulting fission gas releases are reasonable for AFC-4A R1, and R4. A metallic fuel fission gas release of 70%±10% is typical for 75% smeared density U-Pu-Zr fuel beyond ~5×10^{20} fissions per cm^3 [12,24]. The fission gas release in AFC-4A R3 may be slightly elevated compared to the norm. The release based on predicted fission is in-line with the norm, but the release based on measured fission is beyond 100% or, basically, full fission gas release. The fission gas release for AFC-4A R4 is quite low, but the fission density is still below where full porosity interconnection is fully expected.

Table 6. Fission Gas Release Summary.

Rodlet	Fission Gas Release (Predicted Fission)	Fission Gas Release (Measured Fission)
AFC-4A R1	60%	78%
AFC-4A R3	73%	110%
AFC-4A R4	36%	40%
AFC-4A R5	61%	82%

4.1.5 Burnup

During rodlet sectioning to create the microscopy samples, additional samples were taken from near the fuel column mid-plane and were sent to the INL AL for a variety of chemical and isotopic analyses. The primary goal of these analyses was to ascertain the burnup of the sampled material.

Table 7. Burnup values and fission density values for AFC-4A

Rodlet	Simulation Burnup (%FIMA)	Simulation Fission Density (fissions/cm^3)	Measured Burnup (%FIMA)	Measured Fission Density (fissions/ cm^3)
AFC-4A R1	2.4%	9.47E+20	2.6%	7.94E+20
AFC-4A R3	2.5%	8.79E+20	2.2%	6.13E+20
AFC-4A R4	2.6%	8.88E+20	2.7%	7.18E+20
AFC-4A R5	2.5%	8.96E+20	2.5%	7.02E+20

Gamma spectrometry analysis was also performed. Burnup and fission density is calculated as discussed in Section 3.1.5.

The measured burnup values, the measured fission densities, the calculated burnup, and calculated fission density for each rodlet are shown in Table 7. The measured and simulation burnup values are quite similar. This follows recent experience, where measured burnup and simulations agree quite well in the AFC irradiations for burnup in the 1 to 5%FIMA range. There is a bias between the measured fission density and the simulation fission density. Fission density is determined from the mass spectrometry by calculating the number of fission that occurred in the sample and dividing by the volume of the original fuel in the measured sample. The number of fissions in the sample is taken and the average number of fissions calculated from the measured La-139, Ce-140, Ce-142, Nd-143, Nd-145 and Nd-146 content in the sample. The volume of the fuel in the sample is estimated by determining the mass of the fuel in the sample from the mass spectrometry results. The fuel mass is divided by the as-built fuel density to determine volume. Resolving the differences in fission density needs further study because comparing the fuel performance of widely different fuel is more informative when measured properties are trended against fission density, not burnup.

4.1.6 Metallography

For AFC-4A, one transverse cross section mount and one longitudinal section mount were prepared. The transverse cross section was taken from the first 5mm of fuel above the mid-plane of the fuel slug. The longitudinal section for all the rodlets was taken from the next 10 mm of fuel above the transverse section. The transverse sections were ground, back potted with epoxy, ground and polished to a 1 micron diamond paste finish. The longitudinal sections were ground from the outer radius of the fuel to the fuel center in several steps, with epoxy back potting at each step to preserve microstructure. Optical microscopy was performed using a Leica DMi8 inverted microscope. Figure 59 through Figure 69 on the following pages contain optical microscopy collected for AFC-4A. These images are discussed in context with the irradiation conditions and other PIE in the subsequent section.

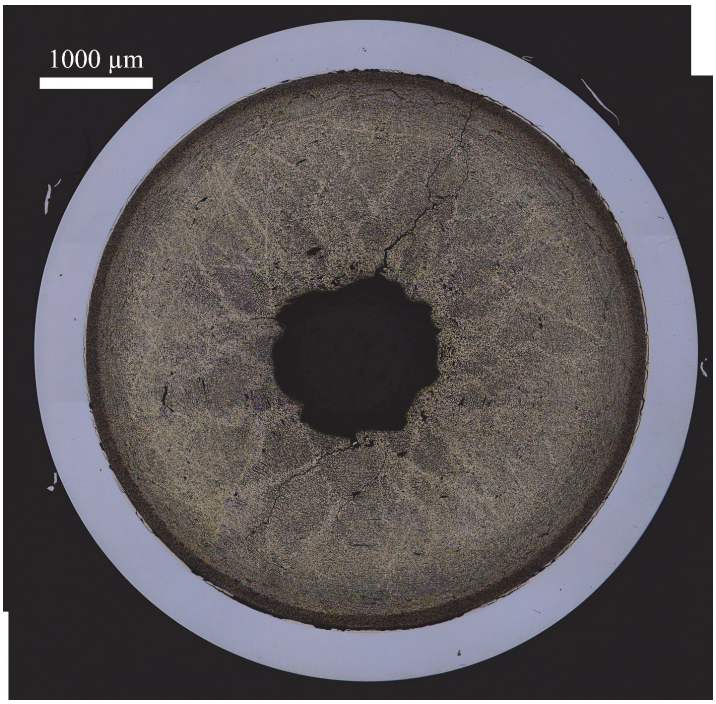

Figure 59. Transverse cross section from AFC-4A R1 (U-10Mo, 55% smear density, He bonded, annular).

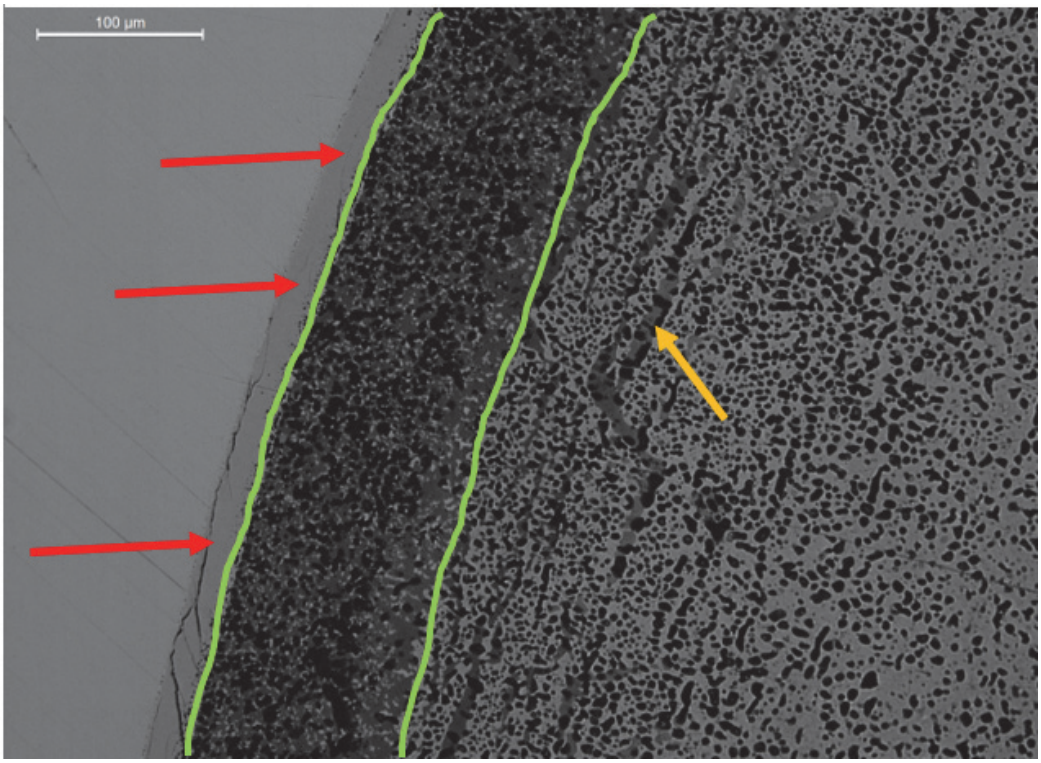

Figure 60. Detail of the interaction region between the fuel and cladding in AFC-4A R1. The red arrows indicated the FCCI cladding wastage layer. The green lines indicated a layer that is liekly iron infiltration into the fuel. The orange arrow indicates a deeper secondary phase that likely contains some iron.

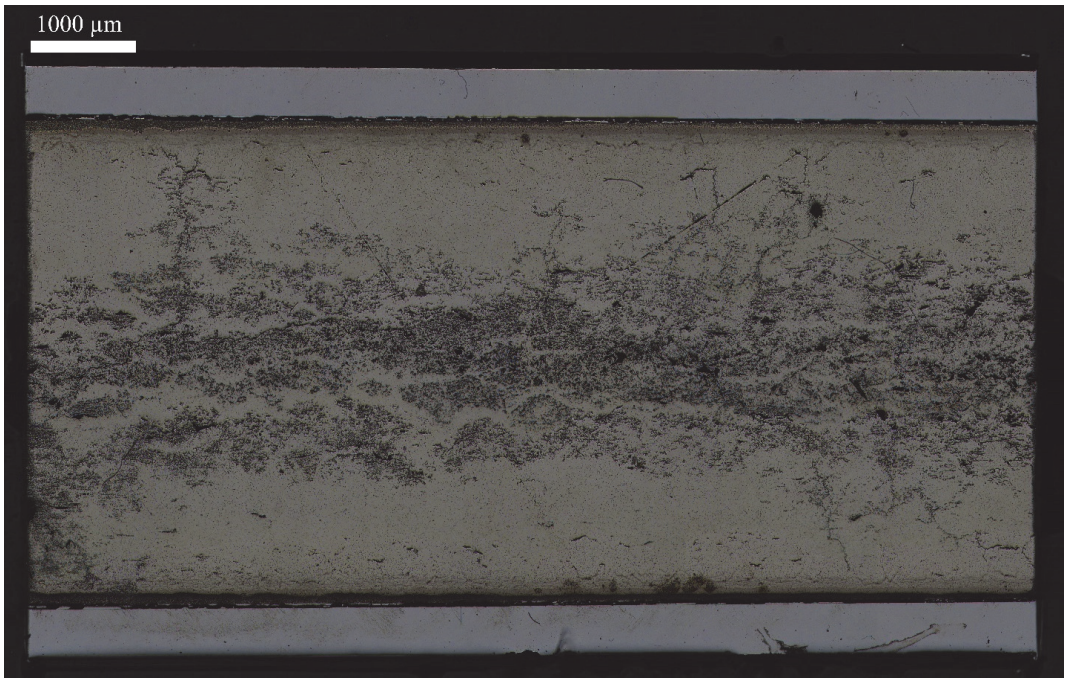

Figure 61. Longitudinal cross section from AFC-4A R1.

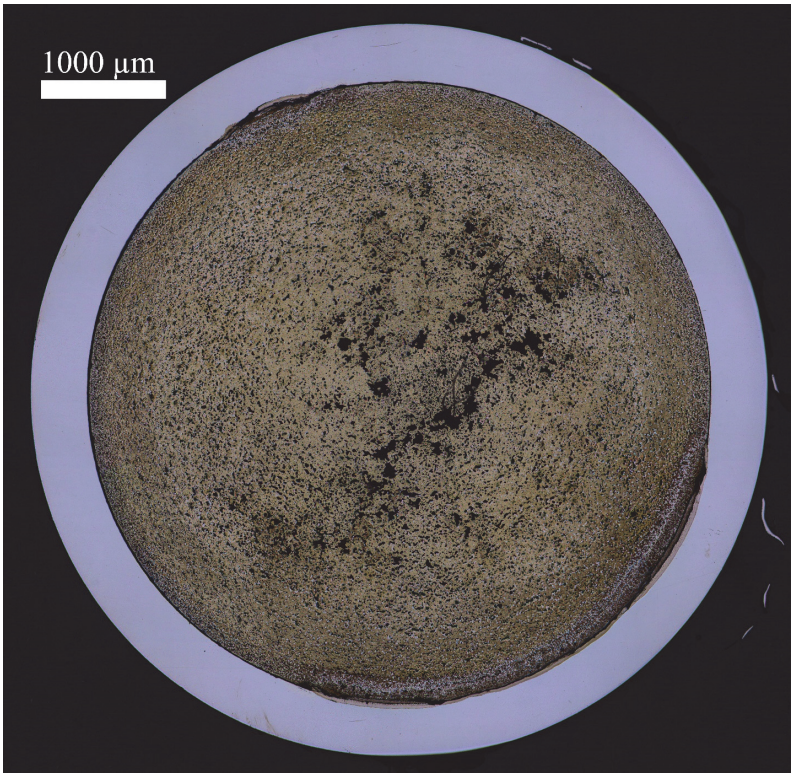

Figure 62. Transverse cross section from AFC-4A R3 (U-5Mo-4.3Ti-0.7Zr, 75% smear density, Na bonded, solid).

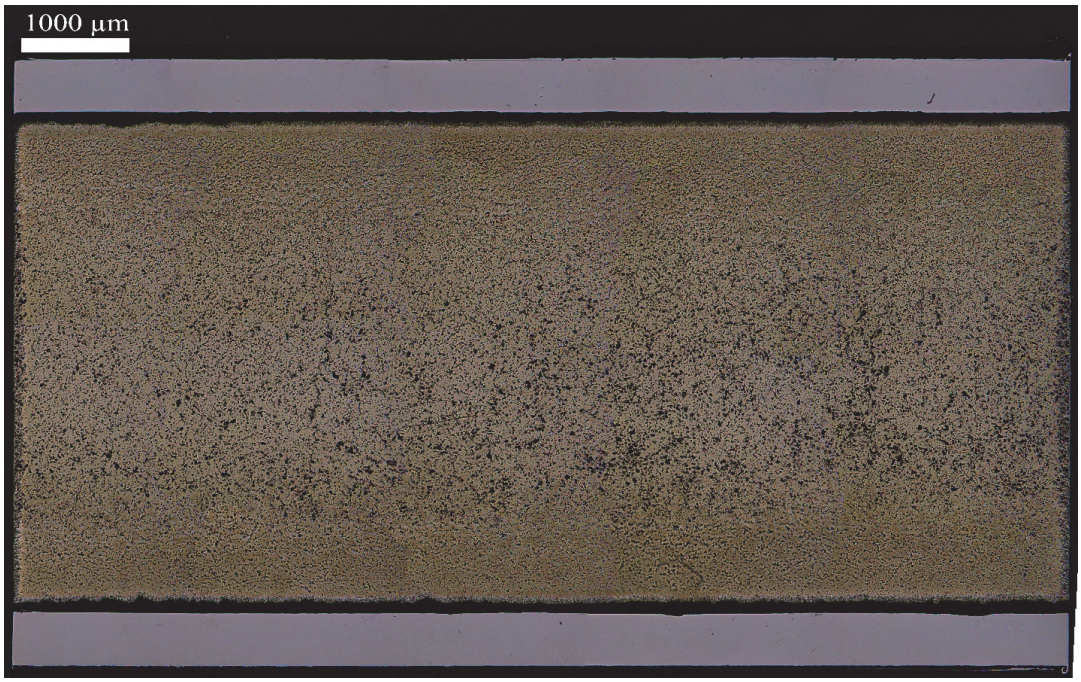

Figure 63. Longitudinal cross section from AFC-4A R3.

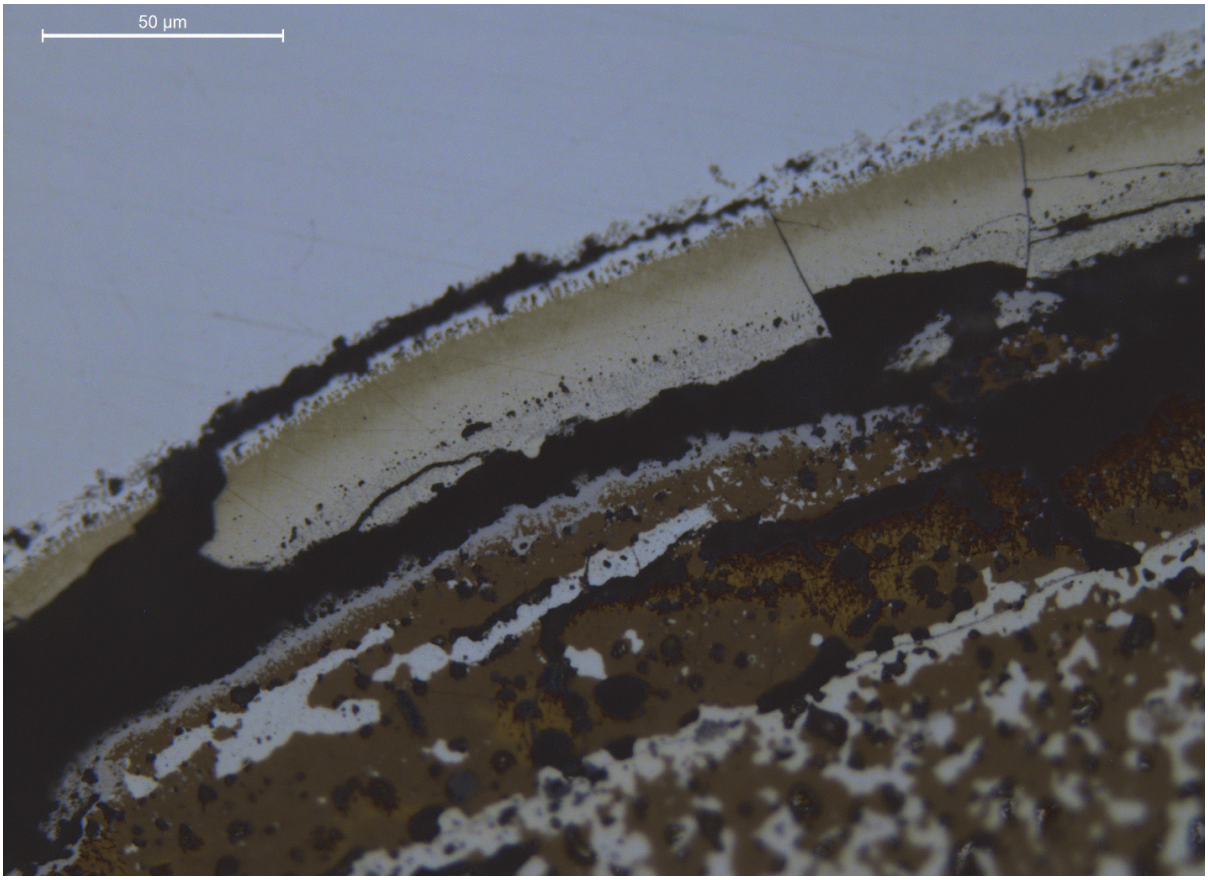

Figure 64. Detail of FCCI between the fuel and cladding in AFC-4A R3.

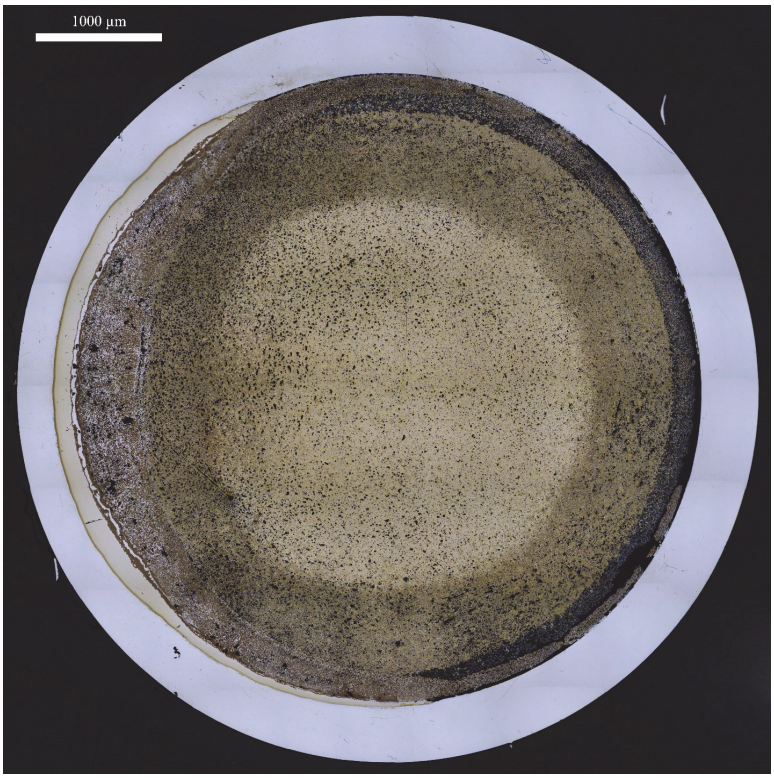

Figure 65. Transverse cross section from AFC-4A R4 (U-2Pd-5Mo-4.3Ti-0.7Zr, 75% smear density, Na bonded, solid).

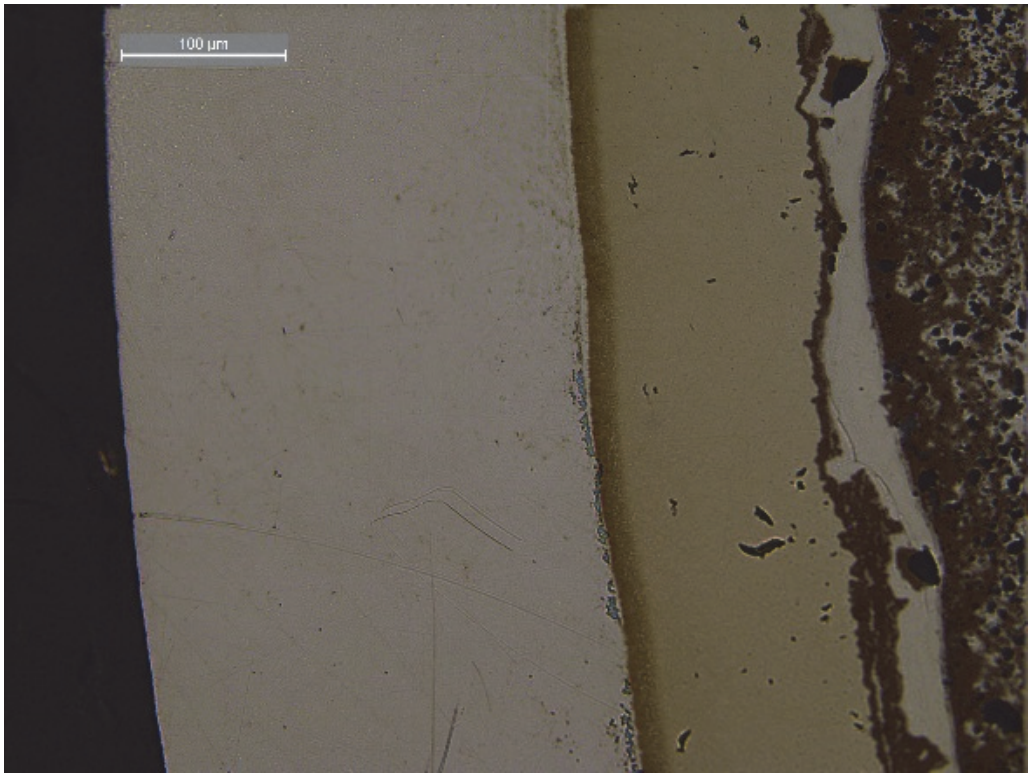

Figure 66. FCCI layers from AFC-4A R4.

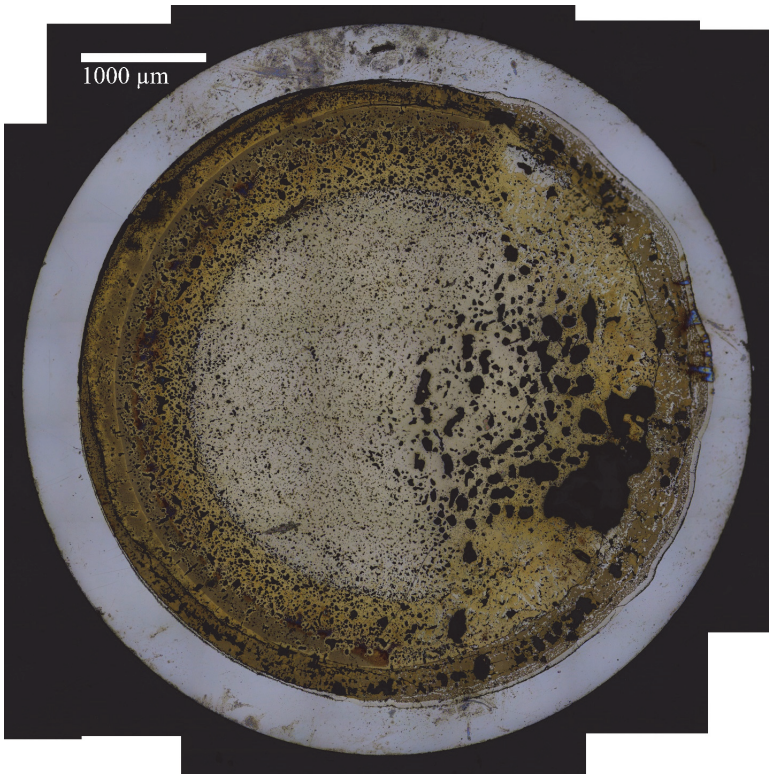

Figure 67. Transverse cross section from AFC-4A R5 (U-10Zr, 75% smear density, Na bonded, solid).

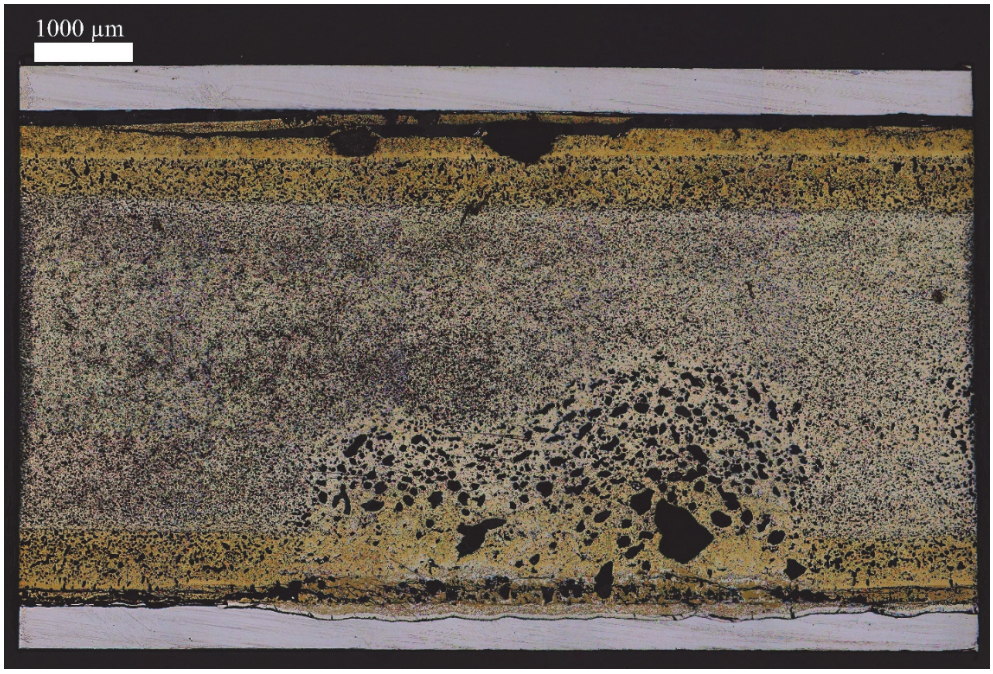

Figure 68. Longitudinal cross section from AFC-4A R5.

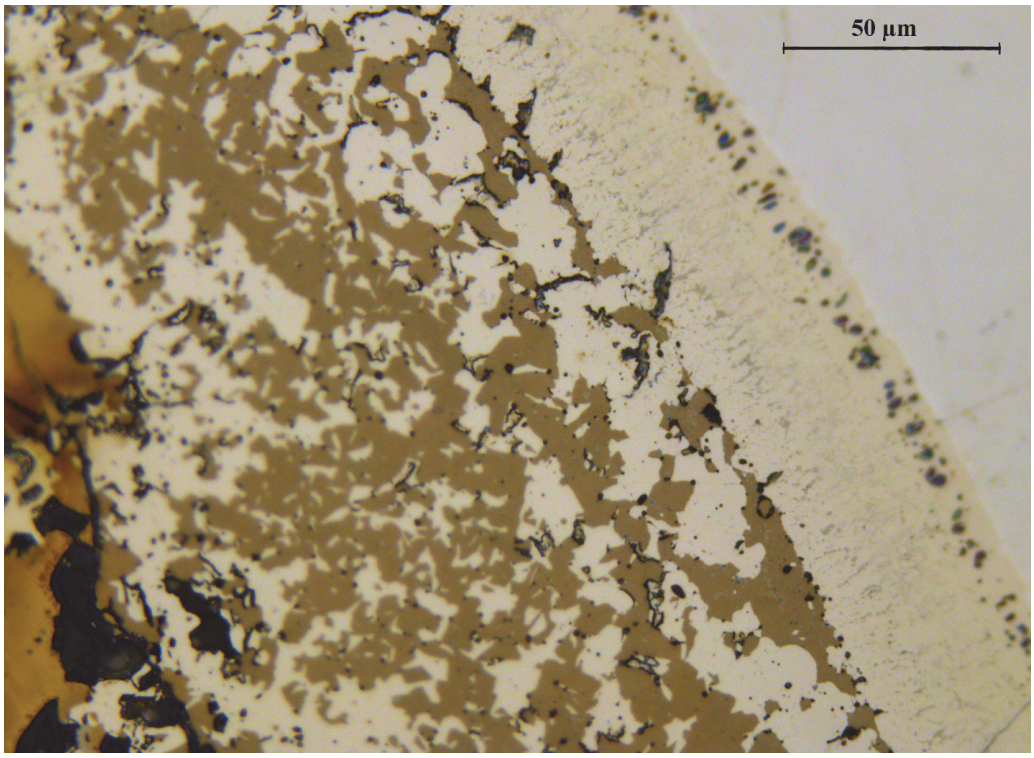

Figure 69. Detail of FCCI in AFC-4A R5.

4.2 Discussion

The discussion of AFC-4A is highly dependent on the irradiation history. As with AFC-3C and AFC-3D, the capsules used in AFC-4A had an inner diameter near 5.969 mm (0.235 inch) not the specified 5.9436 mm (0.234 inch). This difference, which met the specified drawing tolerances, resulted in PICT's that were above desirable conditions of a PICT near 550°C (see Figure 4). The performance of each of the rodlets will be discussed below.

The performance of AFC-4A R1 is somewhat different from other annular U-10Mo rodlets irradiated in AFC-3A/C/D [9] and Section 3.2.1. The temperature experienced by this rodlet is somewhat lower than those experienced by AFC-3C R2 and AFC-3D R4. The PICT history of AFC-A R2 is similar to AFC-4A R1. The axial growth of 4A R1, which was below detection limit, is lower than the other 3 annular U-10Mo pins. The fission gas release of this pin is similar to the other pins. The notable difference in AFC-4A R1 is the large amount of annulus closure seen in Figure 59 and Figure 61. In this case, the annulus may have closed instead of promoting axial swelling prior to fission gas release. Perhaps this is an effect of the early life irradiation history. As with the other annular U-10Mo pin, there is a significant amount of interaction between the fuel and the cladding. This is detailed in Figure 60 ,where there is a cladding wastage layer of approximately 25 µm and a layer, that is likely iron infiltration into the fuel, that extends about 120 µm into the fuel from the cladding.. As expected from the U-Mo phase diagram, the fuel has remained single phase, and the spherical porosity throughout the fuel indicates the crystal structure has remained cubic during irradiation.

The two MTZ alloy pins generally performed like U-10Mo or U-5Fs. The PICT history of these pins is unfortunate because it limits the evaluation of this alloy against historical data. The overall microstructure of the MTZ and MTZ alloy with Pd additive can be seen in Figure 62, Figure 63, and Figure 65. This alloy succeeded in preventing constituent redistribution in the fuel pin and appears to have remained single phase during irradiation. The axial swelling in these alloys is somewhat significant at near 12%.

The cladding strain displayed by these pins in Figure 52 is likely a thermal effect and not a feature of this alloy. Fission gas release in these alloys is in-line with general metallic fuel expectations. The gamma spectrometry of these alloys mostly follows metallic fuel norms also, except in the Ce-144 distribution seen in Figure 58. The Ce-144 tomograms show significant migration of Ce-144 to the fuel periphery. These tomograms can be compared to the even Ce-144 distribution in Figure 19c for U-10Zr or Figure 11b in Reference [9] for U-1Pd-10Zr. There are complicating temperature factors, but Ce-144 and presumably other lanthanides may quickly migrate to the fuel periphery in this fuel alloy, which would be highly undesirable. The FCCI is also highly undesirable in these alloys as detailed in Figure 64 and Figure 66. However, given the PICT history, this interaction is not surprising.

The performance of AFC-4A R5 is again disappointing but not unexpected based on the PICT history. It is more appropriate to compare the results of 4A R5 against accident testing experience, for example [38,39], than steady state irradiation experience. The asymmetric behavior of incipient melting seen in Figure 67 and Figure 68 also matches micrographs from accident testing experience. In many ways this experiment is similar to AFC-2E [40], but the irradiation conditions are better known. The FCCI in Figure 69 is very similar to that seen in high temperature areas of steady state irradiations [37,41].

5. CONCLUSIONS

This report summarizes the PIE performed on three irradiation tests AFC-3C, AFC-3D, and AFC-4A. These irradiation tests investigated a variety of different fuel alloys, geometries, and bonding materials. The majority of these irradiations were performed at peak inner cladding temperatures in excess of 550°C where some interaction with the cladding is expected. Some of the fuel forms performed better than others. The performance of U-10Mo under fast reactor conditions appears to be poor. This was also the conclusion of the AFC-3A and AFC-3B irradiation test **Error! Reference source not found.**, and these irradiation tests have confirmed that U-10Mo is a poor alloy for future testing due to the affinity this alloy has for interaction with iron based cladding. The cubic or gamma phase of the underlying crystal structure in U-10Mo does not seem to provide any consistent benefits to fuel performance as has previously been speculated. The results of AFC-3C and AFC-3D do show the need for precise machining of fuel slugs to match the inner diameter of cladding when helium bonding annular fuel to cladding. The performance of precisely machined, annular fuel in AFC-3C/D was much better than the performance of cast un-machined fuel in AFC-3A/B. The AFC-3D R1 (U-10Zr, 55% smear density, annular, He bonded) may be the best performing fuel irradiated in the AFC campaign since the AFC-1 irradiations. The efficacy of Pd additives is still uncertain. The additional Zr used in AFC-3C/D improved the performance of Pd additive fuel compared to AFC-3A/B. Based on these irradiations, additives can be used effectively in some situations. A more comprehensive review of additives that considers FCCI, additive kinetics, neutronic penalties, fuel cycle costs, and other considerations is needed to optimize the use of additives and to inform future irradiations. The MTZ alloy testing is somewhat inconclusive. There was significant interaction between the fuel and the cladding with this alloy, but the irradiations were also performed at very high temperatures. However, it is also not clear if there is any fuel performance benefit to this alloy or another single phase alloy of Mo-Ti-Zr over the known good performance of U-10Zr. Finally, these tests have highlighted the fabrication constraints of this irradiation design. The results of this have again reemphasized the pre-irradiation review of irradiation conditions prior to insertion into ATR.

6. REFERENCES

[1] Report to Congress on the Advanced Fuel Cycle Initiative: The Future Path for Advanced Spent Fuel Treatment and Transmutation Research, (2003).

[2] S.L. Hayes, J.M. Harp, H.J.M. Chichester, R.S. Fielding, R.D. Mariani, W.J. Carmack, Advances in Metallic Fuels for High Burnup and Actinide Transmutation, in: 14th Inf. Exch. Meet. Actin. Fission Prod. Partitioning Transmutat., San Diego, CA, USA, 2016. doi:https://www.osti.gov/servlets/purl/1358285.

[3] D.C. Crawford, D.L. Porter, S.L. Hayes, Fuels for sodium-cooled fast reactors: US perspective, J. Nucl. Mater. 371 (2007) 202–231. doi:10.1016/J.JNUCMAT.2007.05.010.

[4] G.L. Hofman, L.C. Walters, T.H. Bauer, Metallic fast reactor fuels, Prog. Nucl. Energy. 31 (1997) 83–110. doi:10.1016/0149-1970(96)00005-4.

[5] L.C. Walters, B.R. Seidel, J.H. Kittel, Performance of Metallic Fuels and Blankets in Liquid-Metal Fast Breeder Reactors, Nucl. Technol. 65 (1984) 179–231. doi:10.13182/NT84-A33408.

[6] J.. Kittel, B.R.. Frost, J.. Mustelier, K.. Bagley, G.. Crittenden, J. Van Dievoet, History of fast reactor fuel development, J. Nucl. Mater. 204 (1993) 1–13. doi:10.1016/0022-3115(93)90193-3.

[7] W.J. Carmack, D.L. Porter, Y.I. Chang, S.L. Hayes, M.K. Meyer, D.E. Burkes, C.B. Lee, T. Mizuno, F. Delage, J. Somers, Metallic fuels for advanced reactors, J. Nucl. Mater. 392 (2009) 139–150. doi:10.1016/J.JNUCMAT.2009.03.007.

[8] T. Ogata, Metal Fuel, in: Compr. Nucl. Mater., Elsevier, 2012: pp. 1–40. doi:10.1016/B978-0-08-056033-5.00049-5.

[9] J.M. Harp, H.J.M. Chichester, L. Capriotti, Postirradiation examination results of several metallic fuel alloys and forms from low burnup AFC irradiations, J. Nucl. Mater. 509 (2018) 377–391. doi:10.1016/J.JNUCMAT.2018.07.003.

[10] M.F. Simpson, P. Sachdev, Development of electrorefiner waste salt disposal process for the EBR-II spent fuel treatment project, Nucl. Eng. Technol. 40 (2008) 175–182.

[11] G.S. Chang, R.G. Ambrosek, Hardening neutron spectrum for advanced actinide transmutation experiments in the ATR, Radiat. Prot. Dosimetry. 115 (2005) 63–68. http://dx.doi.org/10.1093/rpd/nci167.

[12] J.M. Harp, S.L. Hayes, P.G. Medvedev, D.L. Porter, L. Capriotti, Testing Fast Reactor Fuels in a Thermal Reactor: A Comparison Report, Idaho Natl. Lab. Rep. (2017) INL/EXT-17-41677. doi:10.2172/1458766.

[13] R.S. Fielding, M.C. Teague, Specification for the AFC-3C/D Fuel Capsule Experiments in the ATR, Idaho Natl. Lab. Rep. (2013) SPC-1607 r.1.

[14] M.P. Teague, AFC-3C and AFC-3D Fuel As-Built Isotopic and Chemical Constituent Report, Idaho Natl. Lab. Rep. (2013) ECAR-2317.

[15] M.P. Teague, R.S. Fielding, Specification for the AFC-4A/B Fuel Capsule Experiments in the ATR, Idaho Natl. Lab. Rep. (2013) SPC-1620.

[16] M.P. Teague, AFC-4A and AFC-4B Fuel As-Built Isotopic and Chemical Constituent Report, Idaho Natl. Lab. Rep. (2013) ECAR-2373.

[17] D. Chapman, As-Built Thermal Analysis for the AFC-3A, AFC-3B, AFC-3C, AFC-3D, AFC-4A and AFC-4B Experiments in the ATR, Idaho Natl. Lab. Rep. ECAR-3742 (2016).

[18] D. Chapman, As-Built Thermal Analysis for the AFC-3D, AFC-4B, and AFC-4C Experiments in

the ATR, Idaho Natl. Lab. Rep. (2016) ECAR-3166.

[19] A.E. Craft, D.M. Wachs, M.A. Okuniewski, D.L. Chichester, W.J. Williams, G.C. Papaioannou, A.T. Smolinski, Neutron Radiography of Irradiated Nuclear Fuel at Idaho National Laboratory, Phys. Procedia. 69 (2015) 483–490. doi:10.1016/J.PHPRO.2015.07.068.

[20] D.L. Porter, H.J.M. Chichester, P.G. Medvedev, S.L. Hayes, M.C. Teague, Performance of low smeared density sodium-cooled fast reactor metal fuel, J. Nucl. Mater. 465 (2015) 464–470. doi:10.1016/J.JNUCMAT.2015.06.014.

[21] D.L. Porter, H. Tsai, Full-length U–xPu–10Zr (x = 0, 8, 19 wt.%) fast reactor fuel test in FFTF, J. Nucl. Mater. 427 (2012) 46–57. doi:10.1016/J.JNUCMAT.2012.03.047.

[22] J.M. Harp, P.A. Demkowicz, Investigation of the Feasibility of Utilizing Gamma Emission Computed Tomography in Evaluating Fission Product Migration in Irradiated TRISO Fuel Experiments, in: Int. Top. Meet. High Temp. React. Technol. (HTR 2014), WeiHai, China, 2014.

[23] J.D. Hunn, C.A. Baldwin, T.J. Gerczak, F.C. Montgomery, R.N. Morris, C.M. Silva, P.A. Demkowicz, J.M. Harp, S.A. Ploger, Detection and analysis of particles with failed SiC in AGR-1 fuel compacts, Nucl. Eng. Des. (2015). doi:10.1016/j.nucengdes.2015.12.011.

[24] R.G. Pahl, D.L. Porter, D.C. Crawford, L.C. Walters, Irradiation behavior of metallic fast reactor fuels, J. Nucl. Mater. 188 (1992) 3–9. doi:10.1016/0022-3115(92)90447-S.

[25] J.M. Harp, P.A. Demkowicz, P.L. Winston, J.W. Sterbentz, An analysis of nuclear fuel burnup in the AGR-1 TRISO fuel experiment using gamma spectrometry, mass spectrometry, and computational simulation techniques, Nucl. Eng. Des. 278 (2014) 395–405. doi:10.1016/j.nucengdes.2014.07.041.

[26] W.J. Maeck, R.P. Larsen, J.E. Rein, Burnup Determination for Fast Reactor Fuels: A Review and Status of the Nuclear Data and Analytical Chemistry Methodology Requirements, U.S. At. Energy Comm. TID-26209 (1973).

[27] M.B. Chadwick, M. Herman, P. Obložinský, M.E. Dunn, Y. Danon, A.C. Kahler, D.L. Smith, B. Pritychenko, G. Arbanas, R. Arcilla, R. Brewer, D.A. Brown, R. Capote, A.D. Carlson, Y.S. Cho, H. Derrien, K. Guber, G.M. Hale, S. Hoblit, S. Holloway, T.D. Johnson, T. Kawano, B.C. Kiedrowski, H. Kim, S. Kunieda, N.M. Larson, L. Leal, J.P. Lestone, R.C. Little, E.A. McCutchan, R.E. MacFarlane, M. MacInnes, C.M. Mattoon, R.D. McKnight, S.F. Mughabghab, G.P.A. Nobre, G. Palmiotti, A. Palumbo, M.T. Pigni, V.G. Pronyaev, R.O. Sayer, A.A. Sonzogni, N.C. Summers, P. Talou, I.J. Thompson, A. Trkov, R.L. Vogt, S.C. van der Marck, A. Wallner, M.C. White, D. Wiarda, P.G. Young, ENDF/B-VII.1 Nuclear Data for Science and Technology: Cross Sections, Covariances, Fission Product Yields and Decay Data, Nucl. Data Sheets. 112 (2011) 2887–2996. doi:10.1016/J.NDS.2011.11.002.

[28] Y.S. Kim, G.L. Hofman, A.M. Yacout, T.K. Kim, U–Mo alloy fuel for TRU-burning advanced fast reactors, J. Nucl. Mater. 441 (2013) 520–524. doi:10.1016/J.JNUCMAT.2013.01.324.

[29] Y.S. Kim, G.L. Hofman, A.M. Yacout, Migration of minor actinides and lanthanides in fast reactor metallic fuel, J. Nucl. Mater. 392 (2009) 164–170. doi:10.1016/J.JNUCMAT.2009.03.043.

[30] B. Kryger, H. Mikailoff, Relation entre le gonflement de combustibles metalliques et le relachement des gaz de fission, J. Nucl. Mater. 34 (1970) 234–236. doi:10.1016/0022-3115(70)90132-7.

[31] L.R. Blake, Achieving high burn-up in fast reactors, J. Nucl. Energy. Parts A/B. React. Sci. Technol. 14 (1961) 31–48. doi:10.1016/0368-3230(61)90071-4.

[32] L.R. Blake, Irradiation of uranium-metal and uranium-oxide fuel pins to high burn-up at high

temperature, J. Nucl. Energy. Parts A/B. React. Sci. Technol. 15 (1961) 140–159. doi:10.1016/0368-3230(61)90050-7.

[33] R.. Barnes, A theory of swelling and gas release for reactor materials, J. Nucl. Mater. 11 (1964) 135–148. doi:10.1016/0022-3115(64)90002-9.

[34] G.L. Hofman, S.L. Hayes, M.C. Petri, Temperature gradient driven constituent redistribution in U□Zr alloys, J. Nucl. Mater. 227 (1996) 277–286. doi:10.1016/0022-3115(95)00129-8.

[35] G.W. Egeland, R.D. Mariani, T. Hartmann, D.L. Porter, S.L. Hayes, J.R. Kennedy, Reduction of FCCI effects in lanthanide–iron diffusion couples by doping with palladium, J. Nucl. Mater. 440 (2013) 178–192. doi:10.1016/j.jnucmat.2013.04.060.

[36] R.D. Mariani, D.L. Porter, V. Blackwood, Z. Jones, D. Olson, B. Mishra, J.R. Kennedy, S.L. Hayes, R.D. Mariani, D.L. Porter, V. Blackwood, Z. Jones, D. Olson, B. Mishra, J.R. Kennedy, S.L. Hayes, New Fuel Alloys Seeking Optimal Solidus and Phase Behavior for High Burnup and TRU Burning, in: Int. Conf. Fast React. Relat. Fuel Cyles Safe Technol. Sustain. Scenar., 2013.

[37] J.M. Harp, D.L. Porter, B.D. Miller, T.L. Trowbridge, W.J. Carmack, Scanning electron microscopy examination of a Fast Flux Test Facility irradiated U-10Zr fuel cross section clad with HT-9, J. Nucl. Mater. 494 (2017) 227–239. doi:10.1016/j.jnucmat.2017.07.040.

[38] G.L. Batte, G.L. Hofman, Run - Beyond - Cladding - Breach (RBCB) test results for the Integral Fast Reactor (IFR) metallic fuels program, in: Conf. Int. Top. Meet. Fast React. Saf., Snow Bird, Utah,United States, 1990. https://www.osti.gov/servlets/purl/7176746.

[39] Y.Y. Liu, H. Tsai, M.C. Billone, J.W. Holland, J.M. Kramer, Behavior of EBR-II Mk-V-type fuel elements in simulated loss-of-flow tests, J. Nucl. Mater. 204 (1993) 194–202. doi:10.1016/0022-3115(93)90217-M.

[40] J.M. Harp, L. Capriotti, H.J.M. Chichester, P.G. Medvedev, D.L. Porter, S.L. Hayes, Postirradiation examination on metallic fuel in the AFC-2 irradiation test series, J. Nucl. Mater. (2018). doi:10.1016/J.JNUCMAT.2018.07.019.

[41] W.J. Carmack, H.M. Chichester, D.L. Porter, D.W. Wootan, Metallography and fuel cladding chemical interaction in fast flux test facility irradiated metallic U-10Zr MFF-3 and MFF-5 fuel pins, J. Nucl. Mater. 473 (2016) 167–177. doi:10.1016/J.JNUCMAT.2016.02.019.